
# Spatiotemporal characteristics of surface water in Sua Pan, Botswana, using Earth Observation data: 1992–2022

by

**Muchelene Peplouw**

**(1762914)**

**Research Report**

Submitted in fulfilment of the requirements for the degree

**Master of Science**

in

**GIS and Remote Sensing**

in the Faculty of Science, University of the Witwatersrand, Johannesburg, South Africa

Supervisor: Prof Stefan Grab

Co-supervisor: Prof Elhadi Adam

October 2024

**Declaration**

I, Muchelene Peplouw, declare that this work has been compiled by myself, that the work is my own, except where stated, and that it has not been previously accepted to any degree except as specified.

Signed…*M. Peplouw*…… (Candidate)

Date…… 14 October 2024……

**Abstract**

Surface water is a critical resource for sustaining both human and ecological health. However, climate change and human actions threaten its availability in semi-arid regions like Botswana. In addition, current research on monitoring and understanding surface water dynamics in Botswana lacks the application of remote sensing and machine learning. This highlights a crucial gap in knowledge that this study aims to address. This study investigates the spatiotemporal dynamics of land use/land cover (LULC) and surface water extent changes in Sua Pan, Botswana, from 1992 to 2022. Employing remote sensing, machine learning, and statistical techniques, the research offers valuable insights into the intricate relationships between land cover modifications, surface water variations, and climatic variables. Google Earth Engine (GEE) facilitated efficient analysis of Landsat imagery for LULC mapping. Random Forest (RF) effectively classified several land cover types within Sua Pan. To address the challenges of saline environments, a novel water index, the Saline Water Index (SWI), was developed specifically for Sua Pan. The McNemar statistical test compared the performance of SWI to established indices like the Modified Normalised Difference Water Index (MNDWI) and the Normalised Difference Salinity Index (NDSI). Surface water variations were analysed using homogeneity tests and the Mann-Kendall trend test. The relationships between hydro-climatic data (rainfall, evapotranspiration, land surface temperature) retrieved from GEE and surface water area for both wet and dry seasons were evaluated using Pearson correlation coefficients and visualised by line and area graphs. Additionally, the influence of the El Niño-Southern Oscillation (ENSO) on rainfall and surface water area was assessed using Analysis of Variance (ANOVA) to identify the specific ENSO phases that exert an influence. The findings demonstrate the effectiveness of GEE for LULC mapping with the RF algorithm, achieving moderate to high classification accuracy (65.2% - 90.69%) and Kappa coefficients (0.54 - 0.85). Surface water and bare area exhibited increasing trends (coefficients: 13.017 and 9.0609, respectively), whereas vegetation and salt hard pan showed decreasing trends (-16.786 and -5.3081, respectively). The newly developed SWI outperformed MNDWI and NDSI in detecting surface water, achieving the highest overall accuracy (94%) compared to MNDWI (64%) and NDSI (59%). The McNemar test confirmed no significant statistical difference between the SWI map and the validation dataset ($p = 0.2673$), while both MNDWI and NDSI maps showed significant differences ($p < 0.0001$). Utilising SWI, the study revealed that surface water was most prevalent in central and northeastern regions, with an average coverage of 33%. Seasonal homogeneity tests indicated a non-homogenous distribution of surface water

area in wet seasons, with abrupt changes in 1994 and 2003. Conversely, dry seasons exhibited a homogenous distribution. The Mann-Kendall trend test identified a statistically significant (*p-value* = 0.01) but weak positive trend (tau = 0.329) for surface water areas in wet seasons. In contrast, the dry seasons displayed a non-significant (*p-value* = 0.734) and a very weak positive trend (tau = 0.043). Surface water area, rainfall, evapotranspiration, and temperature consistently increase during the wet seasons compared to the dry seasons. Notably, increased evapotranspiration significantly impacted surface water presence. ENSO exhibited no significant influence on either rainfall or surface water extent (*p-value* > 0.05 for both). These findings highlight the potential of earth observation data for real-time surface water monitoring in salt pans. The developed techniques offer valuable insights for policy decisions regarding environmental management and conservation efforts in Sua Pan. In addition, the study emphasises the importance of cost-effective approaches for water change assessment, particularly appropriate for under-resourced regions.

**Dedication**

*In memory of my dearest Oupa, Cecil Matthew Johns,*

*To all cancer fighters,*

*To my family, I pray that you accomplish great things.*

*To my mother, who sacrificed and taught me so much.*

*To those who dream, challenge and go against societal norms.*

*I dedicate this paper to the young people of Manenberg. There is space for us in the world; we do not have to be confined to our community. It is time that we take up that space.*

**Acknowledgements**

"Have I not commanded you? Be strong and courageous. Do not be afraid; do not be discouraged, for the LORD your God will be with you wherever you go."

(**Joshua 1:9**)

A few years ago, pursuing a Master's degree at the University of the Witwatersrand seemed an impossible dream. The experience has been as rewarding as it has been challenging. By reflecting on my academic journey, I have come to appreciate the profound strength found in faith. My deepest gratitude goes to God, for this accomplishment would not have been possible without that faith.

Thank you to everyone who has supported, prayed for, and inspired me. Moving to a new city to pursue my Master's studies presented substantial challenges, but with your unwavering support, I could navigate them. A special thank you to my uncle Nigel Peplouw for his unconditional support since I arrived in Johannesburg. His life lessons, culinary expertise, and guidance have been a constant source of strength. I sincerely thank the Haggis family for their generosity and assistance in helping me settle comfortably in Johannesburg. I am also grateful to the Hartle family for becoming my second home. To my family and friends, thank you for your unwavering support, motivation, and encouragement, which fueled my determination to complete this project.

My most profound appreciation goes to my supervisors, Professor Stefan Grab and Professor Elhadi Adam, for the time they invested in this project and for their invaluable guidance. Your mentorship was instrumental in my success. Thank you to the GAES department for their warm welcome and unwavering support. Finally, I sincerely thank Dr Mary Evans for her help and guidance.

The financial assistance of the National Research Foundation (NRF) towards this research is hereby acknowledged. Opinions expressed and conclusions arrived at, are those of the author and are not necessarily to be attributed to the NRF.

# Contents

## List of Tables

## List of Figures

**List of Acronyms**

ANOVA - Analysis of Variance

CHIRPS - Climate Hazard Group InfraRed Precipitation with Station

CV - Coefficient of Variation

ENSO - El Niño southern oscillation

GEE - Google Earth Engine

LST - Land Surface Temperature

LULC - Land use/land cover

ONI - Ocean Nino Index

RF - Random Forest

SVM - Support Vector Machine

SWA - Surface Water Area

# Chapter 1: Introduction

## 1.1. Background

Surface water is a significant resource for human and ecological systems (Wang *et al*., 2022). Surface water ecosystems are necessary as they sustain all life forms and provide habitats to flora and fauna (Setlhogile *et al*., 2011). Additionally, humans rely on it for drinking water, agriculture, and economic value (Kløve *et al*., 2014). Anthropogenic activities, such as agriculture, industrial processes, urbanisation, and climate change, are causing significant surface water variability (Tulbure and Broich, 2019). Rising human populations and expanding economies are projected to burden global water supplies (Setlhogile *et al*., 2011). The variation in surface water bodies profoundly influences natural resources, such as species extinction, and human society (Albarqouni *et al*., 2022). As a result, accurate detection, extraction, quantification and monitoring of surface water dynamics become crucial. Surface water bodies in semi-arid regions are increasingly susceptible to a confluence of pressures. LULC modifications, climate change, and escalating water demands from agricultural, mining, industrial, and domestic sectors contribute to their decline (Geris *et al*., 2022; Segobaetso *et al*., 2022). Fluctuations in surface water can trigger flooding and drought events, significantly impacting human populations and ecosystems (Bhaga *et al*., 2020).

Salt pans are closed basins in arid and semi-arid regions. Here, high evaporation rates exceed precipitation, leading to a concentration of dissolved minerals and the formation of a saline crust (Shaw and Bryant, 2011). These environments are ecologically and economically significant and influence climate through dust emissions (Milewski *et al*., 2020). Despite their saline nature, salt pans are surprisingly widespread and constitute a critical yet unique component of the world's inland aquatic ecosystems (Williams, 2002). Semi-arid regions commonly host salt pans with vulnerable surface water bodies (Mohsen *et al*., 2018). This variability has an impact on the ecological systems. Flamingo breeding occurring in Sua Pan, Botswana, depends on surface water; therefore, during the dry seasons, this salt pan inhabits flamingos (McCulloch and Borello, 2000).

According to Micklin (2010), the Aral Sea is an example of a salt pan with excessive water withdrawal for irrigation and dried up almost entirely, leading to devastating environmental and societal consequences. Additional global examples include Lake Urmia in Iran. It was once the largest saltwater lake in the Middle East and has shrunk dramatically due to water extraction

for agriculture and dams (Javan *et al*., 2016). This has led to ecological devastation with a significant decline in bird population and loss of biodiversity. Furthermore, rainfall pattern changes and human influences have driven significant water level fluctuations in Etosha Pan, located in northern Namibia, over the past decades (Turner *et al*., 2022). This variability poses challenges for the diverse wildlife populations reliant on the pan.

Mapping spatiotemporal surface water of salt pans is crucial to understanding hydrological dynamics in pan systems over time. According to Pekel *et al*. (2016), terrestrial surface water, pans and other inland water bodies comprise 3% of land mass globally. It is a vital water resource to humans and ecosystems. However, anthropogenic activities and climate change have caused several water bodies to degrade (Mohsen *et al*., 2018). These changes have strongly impacted ecosystem functioning, especially on species dependent on the hydrological systems. Collen *et al*. (2014) reported a rapid global decline in water-related ecosystems, highlighting the necessity for consistent monitoring and mapping of surface water bodies.

Traditional methods of measuring surface water, such as collecting samples on-site, are expensive and timely. In contrast, remote sensing is a cost-effective method to continuously monitor water bodies over larger areas and track change (Huang *et al*., 2018). In LULC mapping, data derived from satellite images can be used because of their temporal, spectral and spatial resolution (Nasiri *et al*., 2022). A study by Klemas and Pieterse (2015) demonstrates how satellite radar data can map changes in soil moisture content, indirectly indicating potential changes in groundwater levels relevant for irrigation and ecosystem health in drylands. Landsat data is often used for surface water research due to its extensive coverage and long-term data record (Huang *et al*., 2018).

Researchers are utilising all accessible Landsat imagery to better collect and analyse data on changes in surface water (Albarqouni *et al*., 2022). Concurrently, with the emergence of cloud computing platforms, GEE, researchers can now analyse large-scale geospatial data without technical expertise (Albarqouni *et al*., 2022). This high-performance platform comprises multi-petabyte pre-processed data that are effective and free to use (Albarqouni *et al*., 2022). Additionally, it can investigate surface water extent variations over time (Albarqouni *et al*., 2022).

Researchers developed various GEE techniques to extract surface water information from satellite imagery. One method pioneered by Alesheikh *et al*. (2007) relies on a single band within the image. They can classify water bodies by analysing this band's specific spectral

reflectance properties. Another approach utilises machine learning algorithms. Mim and Zamil (2018) demonstrated how these GEE algorithms are expected to automatically identify water bodies in satellite imagery. However, the most common technique leverages water indices. These indices, developed by researchers (e.g. Rokni *et al*., 2014), are mathematical formulas that combine information from multiple spectral bands. By exploiting the unique spectral signature of water, these indices enhance water features while suppressing surrounding elements (Sisay, 2016; Guo *et al*., 2017).

According to Rokni *et al*. (2014), remote sensing data, including hydrology, has been utilised to monitor LULC changes. Singh (1989, p. 989) defines change detection as "the process of identifying differences in the state of an object or phenomenon by observing it at different times". Recently, water indices have been used to detect changes in water bodies. Sisay (2016) defines water indices as mathematical models that enhance the water signals from images. The standard water indices used to extract water features from Landsat images are NDWI, MNDWI, NDMI, WRI, NDVI, and AWEI (Sisay, 2016). In Botswana, numerous areas are expected to benefit from the mapping and monitoring of spatiotemporal water bodies. These areas include pan systems and rivers, as these water bodies are crucial to the ecosystems and people living in surrounding regions. This study investigated the surface water area changes of Sua Pan, Botswana, using Landsat images from 1992-2022.

### 1.2. Problem Statement

Botswana is a semi-arid and water-scarce country that experiences seasonal rainfall and extended periods of drought (Setlhogile *et al*., 2011). With the surge in water demand, people in Botswana have become reliant on surface and groundwater (Setlhogile *et al*., 2011). However, surface waters are scarce and seasonal, resulting in the reliance on groundwater for industrial, agricultural, domestic, and ecosystem usage (Geris *et al*., 2022). Botswana, a landlocked country, has perennial rivers along the northern and southern parts of the country, resulting in inland surface water being low as the interior rivers are non-perennial (Segobaetso *et al*., 2022). In addition, the recharge of water bodies occurs episodically because of the need for monitoring and aquifer management (Segobaetso *et al*., 2022). The absence of inland surface water, impacts people and affects the environment. A study conducted by McCulloch and Borello (2000) emphasised that the success rate of flamingo breeding depends on surface water availability in Sua Pan, Botswana. In addition, species often relocate once an area experiences drought and return once water bodies receive rainfall (Eckardt *et al*., 2008). In

semi-arid countries, explicitly developing countries like Botswana, there is a relative lack of research, data and information available to help one understand the hydrological dynamics of surface water and its impact on people and the environment. Enhancing our understanding of hydrological systems in southern Africa is necessary to ensure that appropriate conservation measures are put in place, precisely where climate and anthropogenic activities are expected to influence the hydraulic processes in these systems.

Although applying GIS and remote sensing to map and monitor surface water has many benefits, their application in Botswana still needs improvement. More spatial data on surface water resources in Botswana are required to help with effective management. Additionally, Sua Pan is a tremendous economic resource for the country and is essential to the ecological environment, especially in flamingo breeding. Yet, research on detecting surface water using GIS and remote sensing has been limited. Therefore, this study aims to fill this research gap using GIS and remote sensing to detect surface water body changes in Sua Pan, Botswana. The findings of this study will provide insight into the occurrence of surface water in Sua Pan, which can inform policy decisions regarding their management and conservation.

This study maps and monitored the spatiotemporal LULC and surface water area in Sua Pan, Botswana, using GEE for 1992-2022. Many studies have only analysed surface water extent using water index methods, such as the Normalized Difference Water Index (NDWI) and Modified Normalized Difference Water Index (MNDWI). For instance, Xu (2006) and Feyisa *et al*. (2014) utilised these indices to delineate surface water bodies from remote sensing imagery without integrating meteorological data. In contrast, other studies such as Zhou *et al*. (2017) and Huang *et al*. (2018), have combined water index methods with meteorological data such as precipitation and temperature, to evaluate the impact of climate variability on surface water changes. This study presents the spatiotemporal variation of the LULC classes of the study area using a machine learning algorithm. Additionally, the spatiotemporal variations of surface water extent using a newly developed water index are analysed to assess their relationship with ENSO and meteorological parameters.

### 1.3. Aim and Objectives

This study aims to investigate the spatiotemporal dynamics of surface water extent in Sua Pan, Botswana (1992 to 2022), using Landsat TM/ETM+/OLI imagery and the capabilities of the GEE cloud computing platform.

Objectives:

- To assess the effectiveness of GEE in detecting, mapping and monitoring LULC changes within Sua Pan.
- To utilise spectral reflectance measurements captured by Landsat imagery to develop an index using a mathematical model specifically designed to detect surface water in the unique environment of Sua Pan.
- To map and monitor surface water area changes in Sua Pan from 1992 to 2022.
- To leverage GEE's ability to extract hydro-climatic data, such as rainfall, evapotranspiration and LST data and establish a relationship between these variables and the mapped surface water area.
- To explore the influence of ENSO events (El Niño and La Niña) on rainfall patterns and surface water dynamics in Sua Pan.

### 1.4. Research report outline

Chapter 1: Introduction outlines the challenges of monitoring surface water in salt pans due to their unique characteristics. It highlights the research gap and defines the main aim and objectives.

Chapter 2: Literature Review explores existing research relevant to the topic. It defines salt pans and highlights its relationship with climate and anthropogenic activities. Additionally, this chapter focuses on the role of remote sensing in surface water mapping and monitoring and optical remote sensing for salt pans.

Chapter 3: Methodology presents the methodology used, including a description of the study area, the process of acquiring satellite image data, and the data analysis. This involves using machine learning algorithms, developing and applying a new water index, accuracy assessments, and statistical analysis.

Chapter 4: Results describe the findings obtained in this study. In this chapter, LULC mapping using machine learning, the results of applying the new water index to extract seasonal surface water and accuracy assessment are presented. Additionally, statistical analysis, including the meteorological parameters, is presented.

Chapter 5: Discussion compares the results with relevant literature, providing valuable insights and interpretations. It acknowledges limitations encountered during the study and proposes future research directions to further advance understanding surface water dynamics in salt pans.

Chapter 6: Conclusion summarises the key findings and their significance.

## Chapter 2: Literature Review

### 2.1. Defining salt pan

Pans are closed drainage basins accumulating rainwater inflow (De Klerk e*t al*., 2016). Semi-arid and arid regions frequently host salt pans, experiencing high evaporation rates and sporadic rainfall (Milewski *et al*., 2020). According to Dehni and Lounis (2012), salinisation occurs when salt solubility is accumulated in the soil. Additionally, rocks and minerals that have undergone weathering can result in soil being the primary salt source (Alsdorf *et al*., 2007). Moreover, Scheffers and Kelletat (2016) note that salt lakes can transform over time into salt pans through sedimentation. Salt pans are commonly found in dry landscapes, where a salt or clay crust is formed, with the moisture content continuously changing over time (Nield *et al*., 2016). Salt crusts can rapidly influence the topography of the pan surface (Nield *et al*., 2016). Furthermore, when evaporite minerals accumulate on the pan's surface, it is controlled by the depth of the water table, evaporation rates, and the geochemistry of groundwater (Nield *et al*., 2016). Sodium-rich salts on pan surfaces respond to surface moisture changes as the salts change due to temperature and humidity (Nield *et al*., 2016).

In contrast, Salar de Uyuni, the world's largest salina-type evaporite basin, covers a 10,582 km² area in Bolivia (Sanchez-Lopez, 2019). Its surface is typically dry year-round, with occasional flooding occurring only during the December-April rainy season, when 90% of the annual 141 mm precipitation falls. This intermittent flooding transforms the pan into a temporary hypersaline lake (Sanchez-Lopez, 2019). The only permanent water sources come from the Rio Grande de Lipez and Rio Colorado rivers flowing south of Uyuni. Salar de Uyuni is a giant closed basin with no outlet, containing layered salt and mud deposits reaching depths of at least 121 meters (Haferburg *et al*., 2017). It is evident in Figure 2 that saline wetlands are commonly located in South America and southern Africa.

Studies estimate that Earth holds roughly 50,000 salt pans, primarily concentrated in arid regions (Neal, 1975, as cited in Milewski *et al*., 2017). While most are relatively small, covering less than a few square kilometres, some, like Salar de Uyuni in Bolivia (10,582 km²) and Etosha Pan in Namibia, are truly massive (Milewski *et al*., 2017). Salt pans significantly contribute to mineral dust emissions, particularly in dry regions like the Kalahari Desert, encompassing Botswana, Namibia, and South Africa (Milewski *et al*., 2017). It is evident in Figure 1 that southern African salt pans are mainly located in Botswana, Namibia and South Africa. Spanning 22 km², the Omongwa Pan's catchment area in Namibia extends over 172

km² due to the area's unique geomorphology (Milewski *et al*., 2017). Notably, the pan lacks significant surface water inflow, as the Kalahari's highly permeable sands promote rapid infiltration (Milewski *et al*., 2017).


**Figure 1:** Salt pan distribution in Southern Africa (Seaman *et al*., 1991)

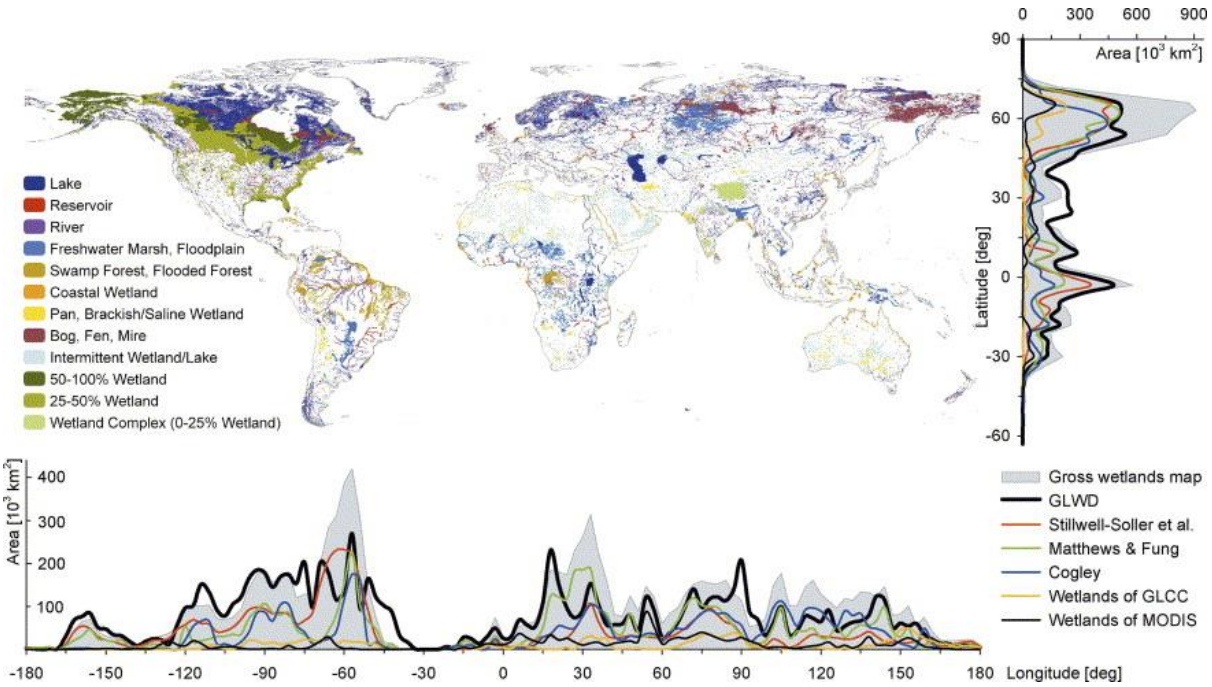


**Figure 2:** Global wetlands map GLWD-3 (Lehner and Doll, 2004)

The classification of pans has been evolving as botanists, sedimentologists, and others have made numerous classification attempts (De Klerk *et al*., 2016). Today, pans are classified into five categories; namely open pans (often associated with vegetation), salt pans (exceeding saline substrate), sedge pans (small – moderate sized pans that are generally perennial), reed pans (contains dense central reed bed) and grass pans (temporary and slightly saline) (De Klerk *et al*., 2016).

## 2.2. Salt pans and climate

Changes in climate and salt pans are becoming a growing concern globally, particularly in the southern African region. Research has shown that current and future climate impacts, including rising temperatures and changes in precipitation patterns, are predicted to significantly affect salt pans (Feher *et al.*, 2017). Some studies have indicated that increased temperatures and decreased rainfall can accelerate the drying of salt pans, leading to changes in salt crystallisation patterns and overall ecosystem dynamics (Liu *et al*., 2013; Bowen *et al*., 2017). Changes in salt pans are expected to ripple outwards, affecting the environment and the lives of people who rely on these ecosystems. From tourism and salt production to the very existence of diverse plant and animal life, the health of salt pans plays a crucial role. A prime example is the Great Salt Lake in the United States, where aridification (Hall *et al*., 2023) threatens critical migratory bird habitat and disrupts local salt production. Similarly, the world's largest salt flat,

Salar de Uyuni in Bolivia, is experiencing altered precipitation and temperature patterns (Milewski *et al*., 2017). These shifts disrupt the unique ecosystem and cast a shadow over tourism activities. In southern Africa, the Makgadikgadi Pans in Botswana face similar challenges. Declining rainfall and rising temperatures have led to the shrinkage of the salt pans, impacting wildlife habitats and traditional uses of the area by indigenous communities (Tarakini *et al*., 2022). Similarly, in Namibia, the Etosha Pan has experienced changes in salt production and altered wildlife migration patterns because of climate-induced shifts in the pan's hydrology (Milewski, 2020).

According to Williams (2002), salt pans have been underestimated and underexplored despite occurring on every continent. Pans are expected to be similar to freshwater lakes in size and have significant economic, scientific, recreational, cultural and ecological values. Many surface waters have distinct ecosystems supporting numerous plant and animal species. The ecosystems provide water supply, recreation, economic benefits and nutrient cycling (Bastin *et al*., 2019). However, surface waters are at risk because of unsustainability, water extraction, land use intensification and climate change.

### 2.3. Anthropogenic impacts on salt pans

While salt pans naturally contribute to dust emissions, their ecological roles are threatened by several anthropogenic pressures. For instance, upstream diversions for agriculture in the Aral Sea basin have significantly reduced freshwater inflow into the once-mighty lake, causing its transformation into a series of shrinking, hyper-saline pans with severe ecological consequences (Su *et al*., 2023). Similarly, salinisation from agricultural runoff in the Heihe River basin of China disrupts the delicate balance of freshwater and salt influx in the Ebinor Lake, impacting its biodiversity (Wang and Cheng, 2000). Additionally, industrial activities like potash mining near the Great Salt Lake (USA) introduce pollutants like heavy metals, impacting the lake's brine shrimp populations, a critical food source for migratory birds (Wurtsbaugh, 2014).

In southern Africa, salt pans face similar challenges. Unsustainable groundwater extraction for agriculture is expected to disrupt the delicate water balance in pans, altering salinity amounts and impacting the unique plant and animal communities adapted to these conditions. For example, studies in the Makgadikgadi Pans complex of Botswana have shown that increased groundwater pumping for irrigation has led to a decline in water levels within the pans, potentially impacting the breeding success of flamingos and other water birds (Hitchcock *et*

*al*., 2000). Furthermore, livestock grazing around pans can contribute to soil erosion and introduce pollutants from manure, further degrading the pan's ecosystem.

## 2.4. Remote Sensing for Surface Water Mapping and Monitoring

Remote sensing and GIS are powerful tools for monitoring changes in surface water (Nhamo *et al*., 2017). Remote sensing involves gathering data about the Earth's surface using sensors on satellites, aircraft, or drones (Mirzakarimova, 2023). These sensors detect and measure electromagnetic radiation emitted or reflected from the Earth, which can be used to understand LULC changes in the environment (Mirzakarimova, 2023). Conversely, GIS is a computer-based system used for analysing, managing, and visualising spatial data (Amoako-Attah *et al*., 2023). Amoako-Attah *et al*. (2023) note that remote sensing and GIS techniques have changed how surface water is monitored and managed. Remote sensing can provide spatial and temporal data and identify changes in water body extent. This information can be processed using GIS tools to analyse the data and derive valuable information (Amoako-Attah *et al*., 2023). These techniques have been used to develop models and algorithms for detecting and mapping surface water bodies.

Surface water monitoring is crucial for water resource management. Traditional techniques through the gauging station are not always feasible due to high costs and being time-consuming. To monitor surface water changes in pan systems, remote sensing techniques are a rapidly increasing alternative (Rahman and Di, 2017). Remote sensing offers a powerful tool for investigating various environments due to its ability to capture data across various spectral, spatial, and temporal resolutions (Ozesmi and Bauer, 2002). Landsats TM, ETM+, OLI, MSS, MODIS, Sentinel-1 and Sentinel-2 are commonly used satellites. Landsat OLI has been increasingly used to map various aspects of semi-arid and arid environments as it has an improved noise-to-signal ratio compared to Landsat TM and ETM+ (Malahlela *et al*., 2018). Methods applied in remote sensing to extract water features include the single-band threshold method (Alesheikh *et al*., 2007), Machine Learning Classification (Mim and Zamil, 2018) and the water index method (Rokni *et al*., 2014).

### 2.4.1. Single band threshold method

The single-band threshold method, introduced by Frazier and Page in 2000, is a simple way to identify water bodies in optical satellite imagery. This method is based on the unique spectral properties of water, which differ from those of other land cover types. Water reflects less in the infrared region than land (Huang *et al*., 2018). For instance, water absorbs NIR light heavily,

causing it to look darker in NIR imagery. This clearly contrasts water and land features (Rokni *et al*., 2014). However, the main limitation of this method is its lack of robustness. The threshold value used to discriminate water from other features is expected not to universally apply across different landscapes or image sources (Huang *et al*., 2018). This may lead to inaccuracies in water extraction, particularly in areas with variable environmental conditions.

### 2.4.2. Machine Learning Classification

The emergence of machine learning classification algorithms revolutionised the field by significantly enhancing the accuracy and usability of classification methods (Avcı *et al*., 2021). Several machine learning algorithms have been developed and used, but RF and SVM algorithms are increasingly popular (Bangira *et al*., 2019; Shih *et al*., 2019). Compared to traditional classification methods, unsupervised classification and visual interpretation, machine learning algorithms have a higher overall accuracy (Gislason *et al*., 2006). However, they do not produce consistent results when using different satellite data. While powerful, it presents challenges, namely acquiring training datasets often necessitates an expensive and time-consuming process. Additionally, if training data incorporate features with identical spectral signatures, the classification algorithm may group them into a single category, leading to misclassifications (Mishra *et al*., 2019). Machine learning algorithms use spectral signatures obtained from ground data to group pixels with similar digital numbers to formulate a single land cover class (Lillesand *et al*., 2015). The spectral properties of the classes formed from the previous process distinguish the various LULC classes from each other, making it easier to detect and map various land cover classes. Avcı *et al*. (2021) compared RF and SVM in LULC classification mapping on Marmara Lake and concluded that RF showed a slightly better classification accuracy than SVM. According to their findings, the overall classification accuracy for RF was 93% compared to 91% for SVM, with the dataset from 2015. In 2020, RF achieved an accuracy of 92.5% while SVM reached 91.7%.

### 2.4.3. Water Index Methods

Li *et al*. (2013) concluded that machine learning algorithms could not map surface water information on a large scale. Therefore, the water index (multi-band) method is preferred to extract surface water information. Using mathematical models, this approach combines multiple spectral bands to enhance the water features while restricting surrounding features (Sisay, 2016; Guo *et al*., 2017). The water index methods produce higher water extraction accuracies and are more efficient, particularly in larger areas (Fisher *et al*., 2016). According

to Rokni *et al*. (2014), the multiband approach is widely used and continues to advance with the development of new satellites and technologies. Like the single-band method, the multiband approach uses a threshold value to distinguish water from other features. However, the multiband approach uses multiple spectral bands, including the blue, green, red, near-infrared (NIR), and shortwave infrared (SWIR) bands. This reduces the chance for two features to share a similar spectral reflectance and to be classified as one feature. The threshold value varies depending on the study area and the methodology used (Fisher *et al*., 2016). These variations are influenced by the unique environmental conditions of the study area, such as differences in topography, vegetation type, soil moisture and water turbidity (Huang *et al*., 2018). For example, thresholds used to detect water might be adjusted based on local conditions, such as clear versus turbid water, or dense versus sparse vegetation (McFeeters, 1996; Feyisa et al., 2014). Methodologically, the type of satellite imagery, such as Landsat and Sentinel-2, and the classification algorithm, such as Random Forest and Support Vector Machine, also play significant roles, as each method processes spectral data differently (Xu, 2006). Additionally, seasonal changes, such as snow cover or drought conditions, can necessitate the adjustment of thresholds to reflect the dynamic nature of the landscape accurately (Zhou *et al*., 2019).

McFeeters (1996) developed the Normalised Difference Water Index (NDWI) using the NIR and Green bands, which enhances water features while reducing vegetation and land reflectance. However, NDWI often misclassifies built-up areas as water. To address this issue, Xu (2006) proposed the Modified Normalized Difference Water Index (MNDWI), incorporating NIR and SWIR bands to reduce the reflectance of built-up areas while enhancing water features. Building on this, researchers have since developed various indices to improve the accuracy of surface water mapping in different environments. For instance, the Automated Water Extraction (AWEI) by Feyisa *et al*. (2014), introduced two variations: AWEIsh for shadowed areas and AWEInsh for non-shadowed areas, effectively distinguishing water from other surfaces and addressing misclassification due to shadows. The Normalized Difference Moisture Index (NDMI), introduced by Wilson and Sader (2002), utilises NIR and SWIR, which has been adapted for water body identification. Similarly, the Water Ratio Index (WRI), proposed by Shen and Li (2010), combines Green, NIR and SWIR bands to distinguish water from other surfaces effectively. The water indices have been applied in studies to capture surface water change over time, including variations in width, volume, extent and water quality deterioration, outperforming traditional inter-spectral relation methods (Zhai *et al*., 2015; Wang

*et al*., 2020). The development of indices such as AWEI, which specifically targets shadowed and non-shadowed areas, further demonstrate their role in refining water feature detection by addressing issues like shadow misclassification due to similar spectral reflectance to water (Feyisa *et al*., 2014).

Jiang *et al*. (2020) developed the Sentinel-2 Water Index (SWI) to extract surface water using a Sentinel-2 satellite. The SWI uses the vegetation red edge band and the SWIR band, which have proven to be more sensitive to detecting water. The SWI was tested against the NDWI index on freshwater lakes, coastal water, saline lakes, and ice. The overall accuracy of the SWI was higher than that of NDWI in both Taihu Lake and the Yangtze River Estuary study areas. The SWI achieved and overall accuracy of 92.75% for Taihu Lake and 93% for the Yangtze River Estuary, compared to 91.5% AND 86.6% for NDWI, respectively. The results showed that the SWI performed better than NDWI in distinguishing the water body from urban areas, sediment, salt, and ice.

Moradi *et al*. (2017) introduced the Modified Optimization Water Index (MOWI) by leveraging the spectral resolution of Landsat 8 OLI for water detection and extraction. Similarly, Wang *et al*. (2018) proposed the Multi-Band Water Index (MBWI) designed explicitly for Landsat 8 imagery. MOWI and MBWI exploit spectral differences between water and other land cover types to map surface water accurately.

Yousefian *et al*. (2019) introduced the Salty Water Index (SWI) for extracting surface water from saline environments using Landsat 8 OLI. The SWI showed superior accuracy to other indices such as NDWI, AWEIsh, AWEInsh, MNDWI, WRI, MOWI and MBWI by suppressing clouds and shadows. The study's results showed that the SWI consistently achieved the highest overall accuracies across all test sites. For instance, in Lake Assal, the SWI achieved an accuracy of 99.54%, outperforming other indices like NDWI (90.34%), MNDWI (86.86%), AWEInsh (92.19%), AWEIsh (96.37%), WRI (86.59%), MOWI (88.06%) and MBWI (96.44%). Similarly, in the Great Salt Lake, the SWI had an accuracy of 98.41%, surpassing NDWI (97.8%), MNDWI (87.16%), AWEInsh (86.52%), AWEIsh (92.29%), WRI (89.91%), MOWI (93%) and MBWI (90.44%). Overall, the SWI was the most accurate water index at all test sites, demonstrating its effectiveness in surface water extraction from saline environments (Yousefian *et al*., 2019).

Landsat satellite imagery, combined with water index methods, has proven to be effective for mapping and monitoring surface water. Numerous studies have evaluated and compared the

accuracy of various water indices using Landsat data, highlighting the strengths and limitations of different approaches (Xu, 2006; Jiang *et al*. 2014; Fisher *et al*., 2016). Xu (2006), for instance, assessed the effectiveness of NDWI and MNDWI in mapping water bodies in China. His findings showed that MNDWI achieved superior accuracy, with an overall accuracy of 99.85% and a Kappa value of 0.99, indicating extremely high reliability. In contrast, the NDWI showed a lower accuracy of 77.25%, primarily due to the mixing of built-up land with water features, leading to an overestimation of water areas. This suggests the MNDWI is more effective for distinguishing water bodies from surrounding land cover types.

Furthermore, Jiange *et al*. (2014) conducted a comprehensive comparison of four water indices–NDWI, MNDWI, AWEIsh and AWEInsh– across various regions in China. Their findings showed that MNDWI and AWEIsh outperformed NDWI. The Automated Method for Extracting Rivers and Lakes (AMERL), when applied alongside optimal thresholding for these indices, showed improved accuracy across different study areas (Hebei, Jiangxi, and Ningxia). Specifically, in the Hebei study area, MNDWI achieved an accuracy of 84.50% (optimal threshold) and 95.78% (AMERL) with similar trends observed in Jiangxi and Ningxia. Notably, the AMERL method consistently enhanced accuracy, particularly for mixed water pixels and narrow rivers, offering a more reliable extraction of water bodies.

Fisher *et al*. (2016) performed a study in eastern Australia to assess the performance of various multiband methods for extracting surface water bodies. They compared these methods against spectral properties and spectrally similar non-water land covers across diverse water types. Their findings indicate that MNDWI was the most effective method, achieving an overall accuracy of approximately 96% higher than NDWI, which had an accuracy of 89%, and the AWEI, with accuracies of 94% (shadow version) and 92% (non-shadow version). For example, MNDWI, which uses green and SWIR bands, accurately extracted a broad range of water bodies, effectively differentiating water from built-up areas. In contrast, the Water Ratio Index (WRI), with an accuracy of 85%, and the Normalized Difference Vegetation Index (NDVI), with a lower accuracy of about 70%, were less effective in water extraction. This demonstrates that MNDWI consistently provided the most accurate results in distinguishing water bodies with different spectral characteristics.

### 2.5. Optical remote sensing for salt pans

Optical remote sensing offers a valuable tool for characterising salt pan environments, improving process understanding, and assessing climate change and human impacts (Shaw and

Bryant, 2011). This approach leverages the spectral reflectance properties of various surface components within salt pans. The visible and NIR regions capture the high reflectance of salt minerals like halite and are influenced by the absorption features of other materials like metal hydroxides and organic matter (Bryant, 1996). The SWIR region is sensitive to clays, carbonates, and sulfates, which have distinct absorption features (Sadrian *et al*., 2023). Notably, surface characteristics like texture, roughness, and water content influence the shape of the spectral reflectance curve by affecting absorption intensity (Milewski *et al*., 2017).

Studies have employed Landsat data to map depositional environments (Castañeda *et al*., 2005; Denhi and Lounis, 2012), differentiate mineral zones (Chapman *et al*., 1989; Flahaut *et al*., 2017), and identify evaporite-rich areas in African endorheic basins (Bryant, 1996). Furthermore, research has utilised Landsat data alongside ground-based information to estimate gypsum abundance in the Chott el Djerid pans (Bryant, 1999) and assess processes within the Makgadikgadi Pans using MODIS and Landsat data (White and Eckardt, 2006). While these studies showcase the utility of remote sensing for salt pan mineralogical characterisation, research on satellite-derived water extent within salt pans, particularly in Africa, remains underrepresented.

## Chapter 3: Study Area and Methodology

### 3.1. Study area

#### 3.1.1. Location

Sua Pan is located in the Kalahari from 20.24° S to 21.20° S and 25.81° E to 26.28° E and represents the eastern part of the Makgadikgadi Pans complex in Botswana (Eckardt *et al*., 2008; Schmidt *et al*., 2023). It has a surface area of approximately 3400 km$^2$ (Burrough, 2022) and is the second largest of the countless smaller pans in Botswana (Eckardt *et al*., 2008). Sua Pan lies south of Nata village and west of Francistown (Friederich *et al*., 1986). The northern part of Sua Pan is subject to brine extraction; it is an important wetland for flamingo breeding (McCulloch *et al*., 2007) and experiences seasonal flooding (Bryant *et al*., 2007).

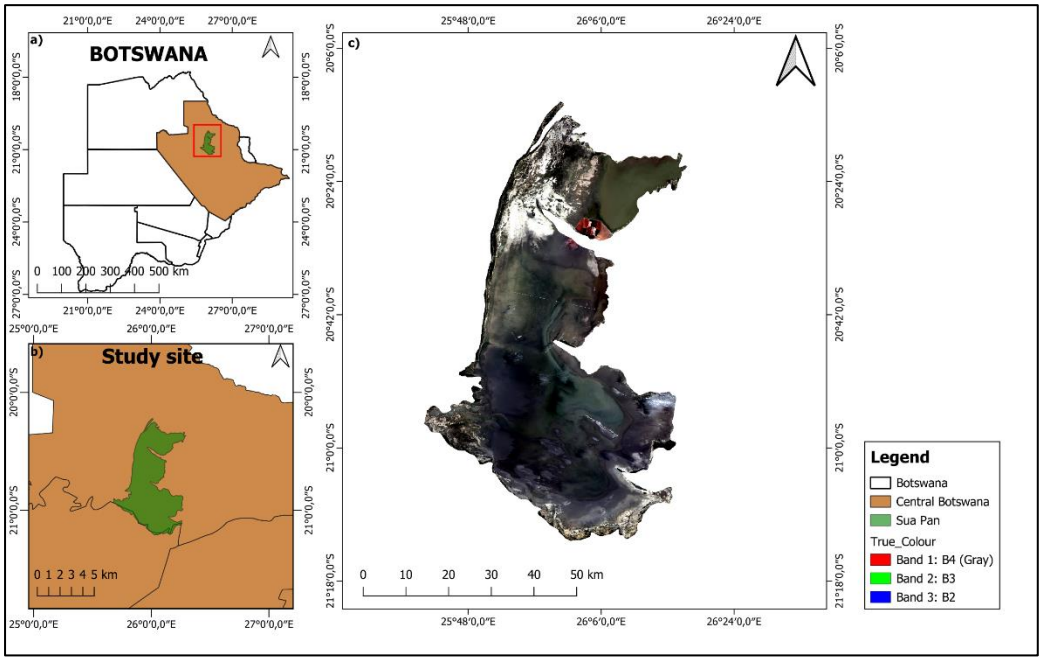


**Figure 3**: a) Botswana b) study site location within Botswana c) satellite image of Sua Pan

#### 3.1.2. Climate

On average, 450 mm of rain falls per annum at Sua Town on the eastern edge of the pan, with the rain season from December to March (Eckardt *et al*., 2008). According to Bryant *et al*. (2007), flooding of Sua Pan has been consistently linked to ENSO cycles during La Niña. ENSO is the dominant mode of interannual climate variability impacting southern Africa (Blamey *et al*., 2018). Traditionally, El Niño events are associated with drier conditions, while La Niña events are linked to increased precipitation over the region (Driver *et al*., 2019). Driver and Reason (2017) further suggest a potential modulating effect of ENSO on the Botswana High, a prominent mid-tropospheric pressure system. A stronger Botswana High, typically

observed during El Niño events, may suppress rainfall, while a weaker High during La Niña may enhance precipitation across southern Africa. Due to Sua Pan being in the central interior of southern Africa, positioned under the descending limb of the Hadley cell circulation (Batisani and Yarnal, 2010), the region has a semi-arid climate (McCulloch and Irvine, 2004). The pan experiences a cool, dry season from May to August, with temperatures ranging from 23 – 25°C during the day and 5 – 8°C at night (McLeod, 2019). The hot, dry season occurs from September to October when daytime temperatures exceed 35°C but decreases to 20°C from November to March in wet years as the region experiences greater cloud cover and rainfall (McLeod, 2019). The pan experiences a warm, dry season in April, with day temperatures ranging from 28 – 30°C (McLeod, 2019). Moreover, consistent wind occurs at the pan as the land is flat and without many trees to prevent wind from blowing (McLeod, 2019).

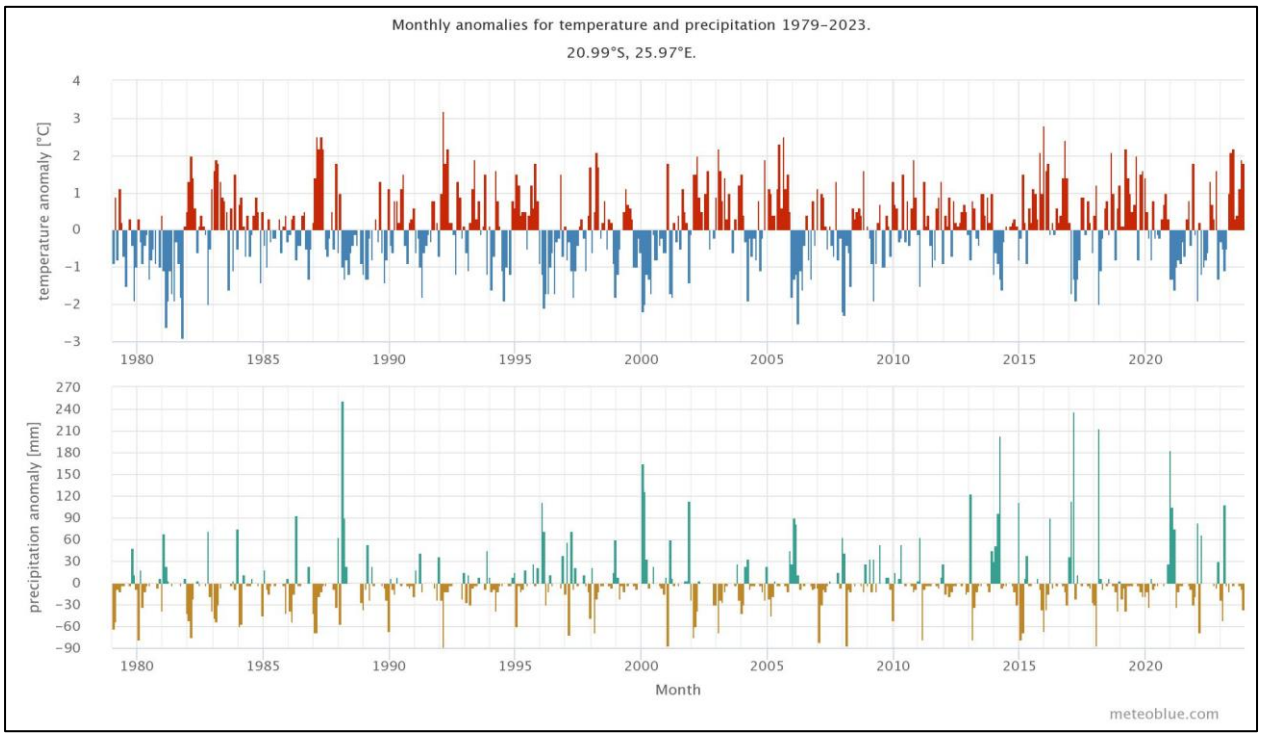


**Figure 4:** Monthly anomalies for temperature and precipitation 1979 - 2023, Sua Pan Botswana (Source: https://www.meteoblue.com/en/climate-change/sua-pan_botswana_933062).

The top graph, Figure 4, indicates the monthly temperature anomaly from 1979 to 2023. The anomaly depicts how much warmer or colder the region is based on the 30-year climate mean of 1980 – 2010. With this, the months coded in red displayed higher temperatures than the baseline, whereas blue months fell below the average. The lower graph, Figure 4, indicates the monthly precipitation anomaly from 1979 to 2023. The anomaly reveals whether a month received more or less precipitation compared to the 30-year climate average (1980-2010).

Green months indicate wetter-than-normal periods, while brown months represent drier-than-normal conditions.

### 3.1.3. Hydrology

Sua Pan receives its water primarily from the ephemeral Nata River and several smaller, seasonal streams draining eastward from gently sloping terrain, including the Semowane, Mosetse, and Mosopo Rivers (Burrough, 2022). Sua Pan collects seasonal river inflow and hosts the most regular inundations (Burrough, 2022; Ringrose *et al*., 2023). The northern part of Sua Pan experiences significant seasonal variations in inundation and desiccation (Eckardt *et al*., 2008). The Mosetse River feeds the shallow extents in the central Sua Pan (Burrough, 2022). However, in southern parts of Sua Pan, seasonal surface water is reported to be unrelated to fluvial surface flow but is likely to have a larger contribution from groundwater (Burrough, 2022). Eckardt *et al*. (2008) found that the pan surface undergoes drying from April to November. This occurs because evaporation rates surpass rainfall during this time.

### 3.1.4. Soil

Sua Pan boasts a smooth surface with a unique clay, silt, and sand blend. Deeper underground, some calcrete cementation can be found (Eckardt *et al*., 2008). This vast expanse holds the dubious honour of being Botswana's dustiest surface. The Nata River plays a crucial role in shaping this landscape: its discharge, along with the pan's characteristic cycles of flooding and drying, are the primary drivers of dust formation (Bryant *et al*., 2007). Interestingly, the evaporation processes occurring on the pan's surface further influence the composition and chemical makeup of the dust.

In the western region of Sua Pan lies Khubu Island, a collection of isolated granite blocks. Their presence is attributed to large-scale faulting events between Sua and Ntwetwe Pans (Burrough, 2022). In stark contrast to the surrounding plains, the northwestern portion of Sua Pan features a unique spectacle - numerous vegetated islands with a distinctive crescent shape. These islands lie perpendicular to the strong easterly winds that frequently blow across the pan (Burrough, 2022).

### 3.1.5. Ecology and vegetation

Sua Pan is a habitat for many species that rely on flooding events and have adapted to droughts for survival. According to McCulloch (2010), various fish species breed in Sua Pan when high rainfall and flooding occur. Cold-blooded animals such as reptiles and amphibians enter the

Pan via the Nata River upstream in Zimbabwe (McCulloch, 2010). According to McLeod (2019), several fish species in Botswana, including barbel, lie dormant in the sand and clay beds during the dry season to survive and start breeding in vast numbers when flooding occurs (McCulloch, 2010). Tilapia breeds well in Sua Pan during floods and can survive during long periods and increasing salinities (McCulloch, 2010). In and around the Makgadikgadi Pan, invertebrates such as spiders, insects and scorpions flourish (McLeod, 2019). Furthermore, termites are the most salient insects, producing enormous visible nests (McLeod, 2019). Terminates are essential to the ecological cycle at the pans as they decompose wood and leaves and recycle nutrients in the soil while simultaneously being prey for other species, such as spiders, birds and other small mammals (McLeod, 2019). The Makgadikgadi system, including major water bodies such as Sua Pan, the Nata and Boteti Rivers, and other surrounding pans, also hosts a diversity of birdlife (McCulloch, 2010). Sua and Ntwetwe Pans are home to over sixty bird species, and Sua Pan is one of the few lesser flamingo breeding sites (McLeod, 2019). The pan sites are also home to drought-adapted mammals such as springbok, gemsbok and steenbok, which are visible year-round (McLeod, 2019). Herds of antelope gather at the pans during the summer rainy season (McLeod, 2019). Moreover, elephants are in protected areas of northern Botswana but may migrate to Nata and Sowa Town during the wet season (McLeod, 2019). The Makgadikgadi Basin's vegetation type and species varies primarily with soil and groundwater depth, salinity and clay percentage (Department of Environmental Affairs and Centre for Applied Research, 2010).

### 3.1.6. Human Influence

The northern region of Sua Pan holds a valuable resource – a vast reservoir of subsurface brine (Eckardt *et al*., 2008). Jutting westward into the basin lies the Sua Spit, a geological feature that now serves as the heart of Botswana Ash (Pty) Ltd.'s soda ash ($Na_2CO_3$) and salt (NaCl) mining operation (Burrough, 2022). This industrial complex, BotAsh, is a significant presence on Sua Pan landscape. It manages an extensive network of infrastructure, including 98 wells, pipelines, an evaporation pond, and processing facilities, all spread across nearly 400 square kilometres ($km^2$) (Eckardt *et al*., 2008). Since its establishment in 1991, BotAsh has extracted groundwater at a high rate (2400 $m^3$/hour) from approximately 40 meters (Burrough, 2022). The estimated volume of brine deposits surpasses a staggering 1 billion cubic meters ($m^3$). Currently, the mine produces sodium chloride (NaCl), sodium carbonate ($Na_2CO_3$), sodium sulfate ($Na_2SO_4$), and sodium bicarbonate ($NaHCO_3$). Interestingly, despite the commercial significance of this operation, a surprising knowledge gap exists regarding the complete

chemical composition and hydrological dynamics of the entire brine system (Eckardt *et al*., 2008).

### 3.2. Satellite image acquisition and pre-processing

This study uses Landsat multitemporal imagery with a spatial resolution of 30 meters to monitor land cover classification and surface water area changes in Sua Pan over the past three decades. Annual Landsat Surface Reflectance (SR) data from 1992 to 2022 were collected from Landsat-5 TM, Landsat-7 ETM+, Landsat-8 OLI, and Landsat-9 OLI (Table 1). The last three months of the rainy season (January to March) and the dry season (August to October) were also analysed to determine changes in surface water area. The initiation of this study in 1992 coincides with the pivotal advancements in satellite technology and data processing. During the early 1990s, the Landsat program transitioned to more systematic and consistent data processing protocols (Wulder *et al*., 2012). The 30-year timeframe allows for insights into long-term environmental trends.

Before conducting any research, it is important to perform pre-processing such as radiometric, geometric, and atmospheric correction to enhance the visibility of each pixel (Gidey and Mhangara, 2023). For this study, Landsat SR Level 2 imageries were used, which have undergone atmospheric and radiometric correction and have been enhanced (Gidey and Mhangara, 2023). The images also include a mask for cloud, shadow, water, and snow, which was developed using the CFMASK (Foga *et al*., 2017) and obtained cloudless images (Yu *et al*., 2023). It should be noted that Landsat-7 ETM+ experienced a scan line error in May 2003, which resulted in missing data gaps (Jamaluddin *et al*., 2022). Therefore, for this study, the fill gap function was implemented to correct the SLC error using focal mean.

Annual median composite satellite images were used from 1992 to 2022 for LULC mapping. The last three months per wet season (January to March) and dry season (August to October) were applied to the stack of images using the code .median( ). Mahdianpari *et al*. (2019) propose using a median composite to address the presence of shadows and clouds in a stack of images. This technique calculates the median value for each pixel across all the images in the stack for bands that correspond to each other. By selecting the median value, pixels affected by shadows or clouds are less likely to influence the final image, resulting in a clearer representation of the underlying land cover.

The image stack was filtered using the .filterDate() function to represent time and by the boundary of Sua Pan using the code .filterBounds(aoi).

**Table 1:** Remote sensing data for LULC and surface water area mapping.

| Year | Dataset | Satellite Sensor | Launch Date | Total number of images |
|---|---|---|---|---|
| 1992 | LANDSAT/LT05/C02/T1_L2 | Landsat5TM | 1 March 1984 | 16 |
| 1993 | LANDSAT/LT05/C02/T1_L2 | Landsat5TM | 1 March 1984 | 19 |
| 1994 | LANDSAT/LT05/C02/T1_L2 | Landsat5TM | 1 March 1984 | 19 |
| 1995 | LANDSAT/LT05/C02/T1_L2 | Landsat5TM | 1 March 1984 | 22 |
| 1996 | LANDSAT/LT05/C02/T1_L2 | Landsat5TM | 1 March 1984 | 18 |
| 1997 | LANDSAT/LT05/C02/T1_L2 | Landsat5TM | 1 March 1984 | 22 |
| 1998 | LANDSAT/LT05/C02/T1_L2 | Landsat5TM | 1 March 1984 | 20 |
| 1999 | LANDSAT/LT05/C02/T1_L2 | Landsat5TM | 1 March 1984 | 20 |
| 2000 | LANDSAT/LT05/C02/T1_L2 | Landsat5TM | 1 March 1984 | 17 |
| 2001 | LANDSAT/LT05/C02/T1_L2 | Landsat5TM | 1 March 1984 | 12 |
| 2002 | LANDSAT/LE07/C02/T1_L2 | Landsat7ETM+ | 15 April 1999 | 22 |
| 2003 | LANDSAT/LE07/C02/T1_L2 | Landsat7ETM+ | 15 April 1999 | 22 |
| 2004 | LANDSAT/LE07/C02/T1_L2 | Landsat7ETM+ | 15 April 1999 | 9 |
| 2005 | LANDSAT/LE07/C02/T1_L2 | Landsat7ETM+ | 15 April 1999 | 18 |
| 2006 | LANDSAT/LE07/C02/T1_L2 | Landsat7ETM+ | 15 April 1999 | 21 |
| 2007 | LANDSAT/LE07/C02/T1_L2 | Landsat7ETM+ | 15 April 1999 | 23 |
| 2008 | LANDSAT/LE07/C02/T1_L2 | Landsat7ETM+ | 15 April 1999 | 22 |
| 2009 | LANDSAT/LE07/C02/T1_L2 | Landsat7ETM+ | 15 April 1999 | 18 |
| 2010 | LANDSAT/LE07/C02/T1_L2 | Landsat7ETM+ | 15 April 1999 | 20 |
| 2011 | LANDSAT/LE07/C02/T1_L2 | Landsat7ETM+ | 15 April 1999 | 8 |
| 2012 | LANDSAT/LE07/C02/T1_L2 | Landsat7ETM+ | 15 April 1999 | 20 |
| 2013 | LANDSAT/LC08/C02/T1_L2 | Landsat8OLI | 11 February 2013 | 59 |
| 2014 | LANDSAT/LC08/C02/T1_L2 | Landsat8OLI | 11 February 2013 | 79 |
| 2015 | LANDSAT/LC08/C02/T1_L2 | Landsat8OLI | 11 February 2013 | 87 |
| 2016 | LANDSAT/LC08/C02/T1_L2 | Landsat8OLI | 11 February 2013 | 83 |
| 2017 | LANDSAT/LC08/C02/T1_L2 | Landsat8OLI | 11 February 2013 | 77 |
| 2018 | LANDSAT/LC08/C02/T1_L2 | Landsat8OLI | 11 February 2013 | 87 |
| 2019 | LANDSAT/LC08/C02/T1_L2 | Landsat8OLI | 11 February 2013 | 86 |
| 2020 | LANDSAT/LC08/C02/T1_L2 | Landsat8OLI | 11 February 2013 | 83 |

| | | | | |
|---|---|---|---|---|
| 2021 | LANDSAT/LC08/C02/T1_L2 | Landsat8OLI | 11 February 2013 | 85 |
| 2022 | LANDSAT/LC09/C02/T1_L2 | Landsat9OLI | 27 September 2021 | 81 |

### 3.3. Reference data

#### 3.3.1. Reference data collected for Landsat classification.

The unavailability of ground data and multitemporal LULC maps of the given study area has resulted in using false-colour-composite and visual-image-interpretation techniques (Gidey and Mhangara, 2023) for collecting sample data. Additionally, The Regional Centre for Mapping of Resource for Development (RCMRD) 2010 LULC Map (https://arcg.is/CGaOb0) was used as a reference map to understand the boundaries of the various classes for the given study area and chosen thematic classes. However, due to the continuous changing of LULC classes, this study performed unsupervised classification to retrieve LULC classes from 1992 to 2022. The spectral information retrieved was analysed and named according to the classes identified from the LULC map for Botswana 2010. The four main classes identified were water, bare area, vegetation and salt hardpans (Table 2). Annual reference data were collected using stratified random sampling (70% training and 30% validation) to sample LULC classes based on their represented sizes within the study area (Appendix A) (Adam *et al*., 2014).

**Table 2:** Description of LULC classes

| **Landcover Classes** | **Code** | **Characteristics** |
|---|---|---|
| **Water** | W | Waterbody |
| **Bare areas** | BA | Non-consolidated bare area, consolidated bare area |
| **Vegetation** | V | Shrubland, grassland, herbaceous vegetation |
| **Salt hardpans** | S | Salt hardpans |

The training samples (70%) were digitised on GEE using the false-colour-composite, similarly used by Gidey and Mhangara (2023), and the validation samples (30%) were digitised using Google Earth Pro due to its high spatial resolution and then imported into GEE (Chabalala *et al*., 2022). The full annual training and validation datasets are attached in Appendix A. The training datasets were used for the Random Forest classifier, while the validation datasets were used for accuracy assessment.

### 3.3.2. Reference data collected for water indices.

Furthermore, binary classification maps were created to map surface water areas using 100 sample points for non-water and 100 for water areas. This was derived using the high spatial resolution of Google Earth Pro Images for 2022 only. Classification accuracies were then derived from MNDWI, NDSI, and SWI thematic maps for 2022. The overall accuracies were then compared. The index with the highest accuracy is used to extract the seasonal surface water area from 1992 to 2022.

## 3.4. Climate data

### 3.4.1. Rainfall

Rainfall data is critical in understanding climate variability and water resource availability. However, historical rainfall data for Sua Pan is often limited due to access constraints. To address this challenge, this study leverages the CHIRPS dataset as it is specifically designed for trend analysis, seasonal rainfall monitoring, and drought assessments, making it a valuable tool for studying Sua Pan despite the limitations of traditional data sources (Ocampo-Marulanda *et al*., 2022). The CHIRPS dataset was selected due to its long-term temporal resolution and suitability for extracting rainfall data from 1992 to 2022. CHIRPS has the best spatial resolution (Ocampo-Marulanda *et al*., 2022). It was previously used by Policelli *et al*. (2019) to correlate surface water area with rainfall. This study uses the Pentad CHIRPS rainfall dataset with a spatial resolution of 0.05° suitable for seasonal monitoring (Rivera *et al*., 2019). The average seasonal data for the wet (January to March) and dry (August to October) seasons from 1992 to 2022 were extracted in GEE.

### 3.4.2. Evapotranspiration

Seasonal evapotranspiration (ET) data were obtained from “MOD16A2.061: Terra Net Evapotranspiration 8-Day Global 500m” from 2001-2022 using Google Earth Engine. These data were selected as they are a component of the hydrological cycle (Garajeh *et al*., 2023).

### 3.4.3. Land Surface Temperature

Using GEE, LST data were compiled from a MODIS product, “MOD11A1.061 Terra Land Surface Temperature and Emissivity Daily Global 1km” from 2000 to 2022. Average seasonal data were extracted. The data were selected as they have the best quality option available (de Almeida *et al*., 2023).

### 3.4.4. ENSO

ONI is a key metric scientists use to monitor the ENSO cycle (Kousky and Higgins, 2007). This index is based on the average sea surface temperature (SST) anomalies in a specific region of the tropical Pacific Ocean called the Niño 3.4 region. The ONI value represents the difference between the average SST in this region over three months and the long-term average SST for the same period.

The ONI values provide a straightforward way to identify the different phases of ENSO:

- **El Niño:** Positive ONI values greater than +0.5°C indicate El Niño conditions. During El Niño events, the tropical Pacific Ocean warms above average.
- **La Niña:** Negative ONI values lower than -0.5°C indicate La Niña conditions. Cooler-than-average sea surface temperatures in the tropical Pacific characterise La Niña events.
- **Neutral:** ONI values between -0.5°C and +0.5°C suggest neutral ENSO conditions, where neither El Niño nor La Niña is dominant (Ubilava, 2017b).

Results of the phase classification applied to the ONI data from NOAA are shown in Figure 5.

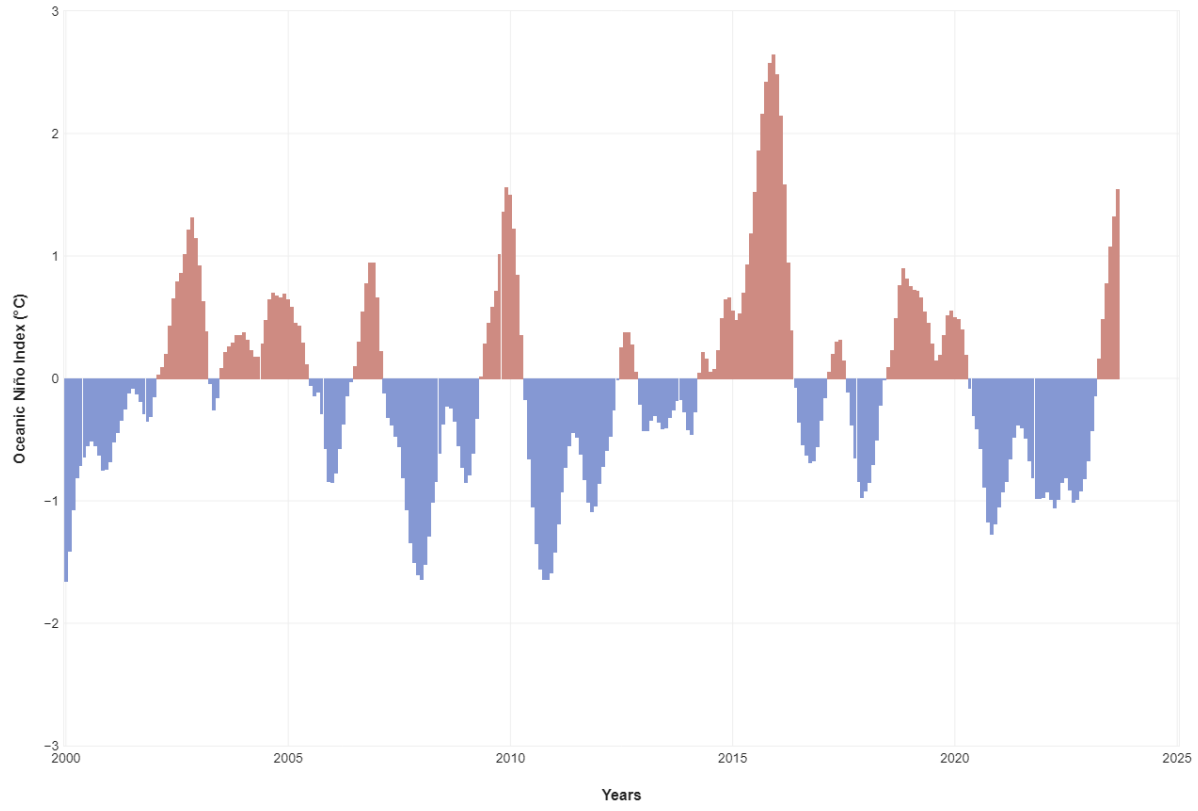


**Figure 5:** Phase classification applied to the ONI data from NOAA (source: https://www.climate.gov/news-features/understanding-climate/climate-variability-oceanic-nino-index)

## 3.5. Image data interpretation and analysis

### 3.5.1. Classification analysis and mapping

#### *a) Random Forest*

Once the training samples were developed in GEE, supervised classifications were performed. The yearly LULC image classifications from 1992 to 2022 were executed using the RF algorithm. It is an ensemble classifier combining multiple decision tree models to improve classification accuracy (Ao *et al*., 2019). Each tree is generated using a random subset of features (predictors) from the input data, enhancing the robustness of the model (Breiman, 2001). This approach offers several advantages for land cover classification, as Slagter *et al*. (2020) highlight. Firstly, RF can effectively handle large variations within land cover classes, ensuring accurate classification even for complex landscapes. Secondly, the algorithm can handle noise within the data, offering improved performance compared to methods sensitive to noisy data (Rodriguez-Galiano *et al*., 2012). Akinyemi *et al*. (2019) reported to have used RF in GEE to produce land cover maps of Botswana in 2015, with an overall accuracy of 74%,

and 2018, with an overall accuracy of 77%, using Landsat 8 data. For RF, 500 *ntree* was selected as a default value (Adam *et al*., 2014; Dube *et al*., 2019).

***b) Change detection***

The LULC classes occupying Sua Pan were using RF from 1992 to 2022. The class area for each LULC map was extracted from GEE to assess the landcover transitions between the various years. A spatiotemporal trend analysis was applied to see how the LULC classes have changed from 1992 to 2022. Additionally, the maps produced give a visual representation of these changes.

### 3.5.2. Surface water detection, analysis and mapping

***a) Development of the Saline Water Index***

For this study, I adopted a combination of the MNDWI and NDSI to detect surface water in a salt pan with a formula influenced by the Vegetation Soil Salinity Index (VSSI) (Dehni and Lounis, 2012) and the Salinity Index (Abbas and Khan, 2007). MNDWI uses the green and the SWIR bands to discriminate water from non-water features (Xu, 2006), whereas NDSI uses the red and NIR bands to retrieve salt classes (Khan *et al*., 2005). The VSSI discriminates between soil and vegetation stress (Dehni and Lounis, 2012). According to Seaman (1991), Sua Pan is shallow and does not have uniform ground level. Additionally, the northeastern part of Sua Pan is fed by the Nata River and other ephemeral streams (Riedel *et al*., 2012). This suggests different surface water areas in the pan have different salinity levels. Therefore, this proposed index will be able to detect all levels of wetness, including freshwater to hypersaline water, with a threshold of ≤ 0.4 (Figure 6).

SWIL9 | Get Link | Save | Run | Reset | Apps

```
132
133  //>> Saline Water Index
134  var SWI = l9composite.expression(
135      "(2 * NIR - 5 * (GREEN - SWIR1) * sqrt (GREEN * RED))",
136      {
137        NIR: l9composite.select("SR_B5"),     // NIR
138        SWIR1 : l9composite.select("SR_B6"),   // SWIR1
139        GREEN: l9composite.select("SR_B3"),   // GREEN
140       RED: l9composite.select("SR_B4"),     //  RED
141      });
142
143  Map.addLayer(SWI, {min: 0, max: 1, palette: ['blue', 'pink','white']}, "SWI");
144
145  var swiThreshold = SWI.lte(0.4);
146  var swiMask = swiThreshold.updateMask(swiThreshold);
147
```

**Figure 6:** Saline Water Index in GEE using Landsat 9

### *b) Calculation of indices for detecting surface water using Google Earth Engine*

Landsat 9 OLI was filtered by date (2022-01-01 to 2022-12-31) to obtain available images in 2022. Further, the images were all stacked using the `.median()` code and clipped according to Sua Pan boundary using the code `.clip(aoi)`. It was further filtered by less than 10% cloud coverage, representing a low cloud coverage. The median composites were used to compute MNDWI, NDSI and SWI (Table 3). The MNDWI can discriminate between open water and other land surfaces (Jamaluddin *et al*., 2022). The NDSI effectively hydro-salinized area mapping (Khan *et al*., 2005). The author created the SWI to detect surface water irrespective of salinity levels. Although the study focuses on Sua Pan for 1992 – 2022, 2022 was only selected to test the validity of MNDWI, NDSI and SWI.

**Table 3:** Landsat 9 OLI spectral indices retrieval

| **Index** | **Formula** | **Reference** |
|---|---|---|
| **MNDWI** | (GREEN–SWIR1)/ (GREEN+SWIR-1) | Xu (2006) |
| **NDSI** | (RED-NIR)/(RED+NIR) | Khan *et al*. (2005) |
| **SWI** | (2 * NIR - 5 * (GREEN - SWIR1) * sqrt (GREEN * RED)) | Author |

The threshold selection for MNDWI and NDSI was `.gte(0.1)` to divide the water class from the nonwatery class. However, the SWI was created to automatically detect water class mixed with salt, resulting in the threshold being .lte`(0.4)`. Hereafter, the output images were converted into binary classification. MNDWI and NDSI values greater than and equal to 0.1 were classified as water, and values less than 0.1 to -1 were classified as non-water. For SWI, values less than and equal to 0.4 were classified as water and values greater than 0.4 were classified as non-water. Following the binary classification, the results were vectorised to mask the water class. This was performed only for the study site (Sua Pan). The index with the highest accuracy assessment was used to quantify the surface water area seasonally from 1992 to 2022.

### 3.5.3. Processing in Google Earth Engine: Surface water extraction

To assess the seasonal (January to March, i.e. last three months of the rain season, and August to October, i.e. last three months of the dry season), hydrological dynamics from 1992 to 2022, the Saline Water Index (SWI) was applied to identify, discriminate and measure the surface

water from non-water pixels within the study area using Landsat 5, 7, 8 and 9 images. The SWI is suitable for detecting fresh to hyper-saline water with a threshold of 0.4.

### 3.5.4. Seasonal surface water area spatiotemporal trend analysis

The surface water area binary maps derived from the SWI at Sua Pan were evaluated from 1992 to 2022. A spatiotemporal trend analysis was applied to see the change in the surface water area. The advantage hereof is that information about the direction and magnitude of change can be derived from it. Maps displaying the surface water area at the end of the wet and dry seasons from 1992 to 2022 were produced to visually present how surface water has changed.

### 3.5.5. Accuracy assessment

The RF classifier was evaluated annually using the derived classification maps' accuracy assessment from 1992 to 2022. According to Newete *et al*. (2023), an accuracy assessment tests the validity and reliability of the classifiers. To validate the RF classification outputs, 30% of the sample data points for each class were obtained from high-resolution Google Earth Pro images. These sample points were then imported into Quantum Geographic Information System (QGIS) and converted into shapefiles. After exporting the shapefiles from QGIS, they were imported into the GEE platform for accuracy assessment.

Furthermore, 100 sample points for non-water areas and 100 sample points for water areas were derived using the high spatial resolution of Google Earth Pro for 2022. Classification accuracies were then derived from MNDWI, NDSI, and SWI thematic maps. The index with the highest overall accuracy is used to extract the seasonal surface water area from 1992 to 2022.

The accuracy of the classified maps was evaluated using standard accuracy metrics, including Overall Accuracy (OA), User's Accuracy (UA), Producer's Accuracy (PA), and the Kappa Coefficient. Overall Accuracy (OA) represents the proportion of correctly classified sample points out of the total sample points and is calculated by dividing the number of correctly classified points by the total number of points. User's Accuracy (UA) indicates the likelihood that a pixel classified into a given category represents that category on the ground, calculated by dividing the number of correctly classified points for a class by the total number of points assigned to that class. Producer's Accuracy (PA) shows the probability that a reference sample point has been correctly classified, calculated by dividing the number of correctly classified

points for a class by the total number of actual points for that class in the reference data. The Kappa Coefficient, a statistical measure accounting for the possibility of chance agreement, was calculated using the formula:

*Equation 1: Kappa Coefficient*

$$k = \frac{N\sum_{i=1}^{k} x_{ii} - \sum_{i=1}^{k}(x_{i+} \times x + i)}{N^2 - \sum_{i=1}^{k}(x_i \times x + i)}$$

Where:

N = Total number of observations.

$x_{ii}$ = The diagonal elements of the confusion matrix, representing agreement.

$x_{i+}$ and $x + i$ = The sums of the counts for each row and column, representing the marginal totals.

$k =$ The number of classes (Cohen, 1960).

A significance test was computed between the validation sample points and the MNDWI, NDSI and SWI maps. The Mcnemar test was applied to each water index against the validation sample points. The McNemar test is based on a chi-square ($\chi^2$) statistic as given by:

*Equation 2: Chi-square statistic*

$$\chi^2 = \frac{(|b - c| - 1)^2}{b + c}$$

Where:

$b$ and $c$ = frequencies from the contingency, related to the observed values.

$b - c$ = represents the absolute difference between $b\ and\ c$.

$(|b - c| - 1)$ = Subtracting 1 in the numerator is used as a continuity correction to improve the approximation of the Chi-square statistic (Yates, 1934).

## 3.6. Statistical analysis

### 3.6.1. Homogeneity testing

Homogeneity tests, Pettit, Buishand, and Standard Normal Homogeneity Test (SHNT), were applied to the seasonal surface water area to detect if the data were homogenous. According to Javari (2016), this statistical method is used to time series data to detect if abrupt change has

occurred. Pettitt (1979) developed the non-parametric test, indicating no assumptions about the data distribution. Alexandersson (1986) developed the SNHT, a likelihood ratio test for change detection in the data. It is suggested that multiple methods of homogeneity testing should be used to assess homogeneity in time series data (Ahmed *et al*., 2018). The Homogeneity testing was performed using the XLSTAT statistical package.

### 3.6.2. Mann-Kendall testing

The Mann-Kendall trend test determined if the data have changed over time (Mann, 1945; Kendall, 1975), and the Sen's slope was used to determine the magnitude of change (Fuentes *et al*., 2020). This is commonly used in time series hydrometeorological studies (Gocic and Trajkovic, 2013). This statistical analysis was applied to the proposed Saline Water Index (SWI) seasonal surface water extent to assess trends using R-Studio.

### 3.6.3. Linear Regression

The relationships between surface water area and hydro-meteorological data of the wet and dry seasons of Sua Pan were derived using simple linear regression. Linear regression is useful for determining the relationship between variables and provides information about the proportion of variability that can be accounted for by the predictor variable (Cohen *et al*., 2013). This statistical analysis was performed in Microsoft Excel.

### 3.6.4. ANOVA test

The Analysis of Variance (ANOVA) was used to determine if there were statistically significant differences in mean rainfall and surface water area across the different ENSO phases. The Tukey's Honestly Significant Difference (HSD) post-hoc test was applied to explore which specific pairs of the ENSO phases differed. The statistical significance was set at a *p-value* of less than 0.05 using R-Studio.

### 3.6.5. Correlation

Pearson correlation measures two variables' direction and magnitude of association (Obilor and Amadi, 2018). The correlation coefficient is represented by r and can range from -1 to +1, signifying perfect negative and positive correlation coefficients. A correlation value 0 indicates no relationship between the variables (Obilor and Amadi, 2018).

For this study, the test was done under the hypothesis:

$H_0$: The variables are not correlated.

$H_A$: The variables are correlated.

At a 5% significance level. If the P-value is < 0.05, the variables are correlated; if the p-value is > 0.05, the variables are not correlated.

The correlation between climate variables and the surface water area of Sua Pan was studied to understand the behaviour of each variable in the presence of other variables. The correlation matrix for the correlation coefficient for both the wet and dry seasons was derived using the XLSTAT statistical software.

**Table 4:** Pearson's correlation coefficients interpretation (Akoglu, 2018)

| ***R*** | **Correlation Level** |
|---|---|
| +0.70≤ n | A very strong positive |
| +0.40≤+0.69 | Strong positive |
| +0.30≤+0.39 | Moderate positive |
| +0.20≤+0.29 | Weak positive |
| +0.01≤+0.19 | No or negligible |
| 0 | No |
| -0.01≥-0.19 | No or negligible |
| -0.20≥-0.29 | Weak negative |
| -0.30≥-0.39 | Moderate negative |
| -0.40≥-0.69 | Strong negative |
| -0.70≥n | A very strong negative |

# Chapter 4: Results

## 4.1. LULC accuracy assessment analysis

The performance of the Random Forest classifier was assessed using various metrics: overall accuracy, producer's and user's accuracy, F1 score, and Kappa statistic. To validate annual classified images from 1992 to 2022, 30% of the sample data (refer to Appendix A) was used. Figure 7 displays the overall accuracy, while Figure 8 shows the annual Kappa coefficient from 1992 to 2022. Landsat 5 TM was used from 1992 to 2001, with the overall accuracy ranging from 65.2% to 77.67% and the Kappa coefficient ranging from 0.54 to 0.7, indicating a moderate to substantial strength of agreement. The years 1992, 1993, 1994, 1995, 1996, 1997, 1998, 1999, 2000 and 2001 had an overall accuracy of 65.22%, 71.01%, 73.22%, 65.71%, 69.67%, 70.34%, 74.38%, 70.71%, 69.93% and 77.67%, respectively; all higher than 65%, indicating a satisfactory overall accuracy.

From 2002 to 2012, Landsat 7 ETM+ was used in the LULC classification. It had an overall accuracy that ranged from 68.4% to 82.43%, and the Kappa coefficient ranged from 0.57 to 0.75, indicating a moderate to substantial strength of agreement. The years 2002, 2003, 2004, 2005, 2006, 2007, 2008, 2009, 2010, 2011 and 2012 had an overall accuracy of 78.02%, 74.41%, 77.26%, 68.4%, 76.87%, 82.43%, 79.53%, 79.42%, 81.19%, 78.74% and 75.65%, respectively; all higher than 65%, indicating a satisfactory overall accuracy.

Landsat 8 OLI was used in the LULC classification from 2013 to 2021. It had an overall accuracy that ranged from 79.2% to 85.09% and the Kappa from 0.71 to 0.8, indicating a substantial strength of agreement. The years 2013, 2014, 2015, 2016, 2017, 2018, 2019, 2020 and 2021 had an overall accuracy of 82.26%, 80.86%, 84.57%, 82.11%, 81.14%, 84.07%, 80.53%, 79.2% and 85.09%, respectively; all higher than 65%, indicating a satisfactory overall accuracy. For 2022, Landsat 9 OLI was used in the LULC classification. It had an overall accuracy of 90.69% and a Kappa coefficient of 0.85, indicating an almost perfect strength of agreement.

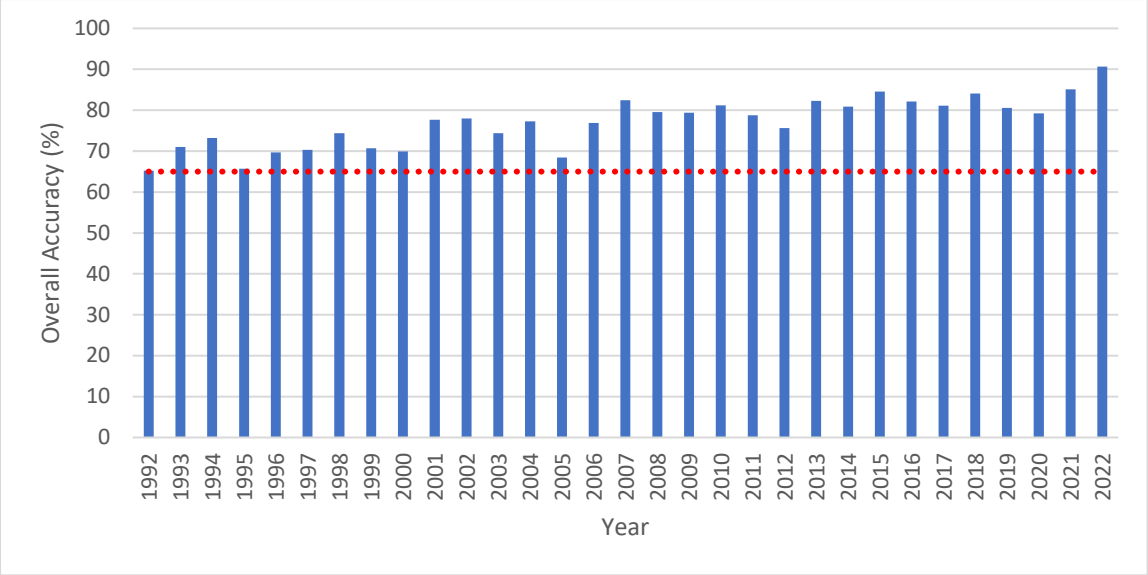


**Figure 7:** Annual overall accuracy of LULC classes from RF. The red dotted line represents satisfactory overall accuracy results above 65%.

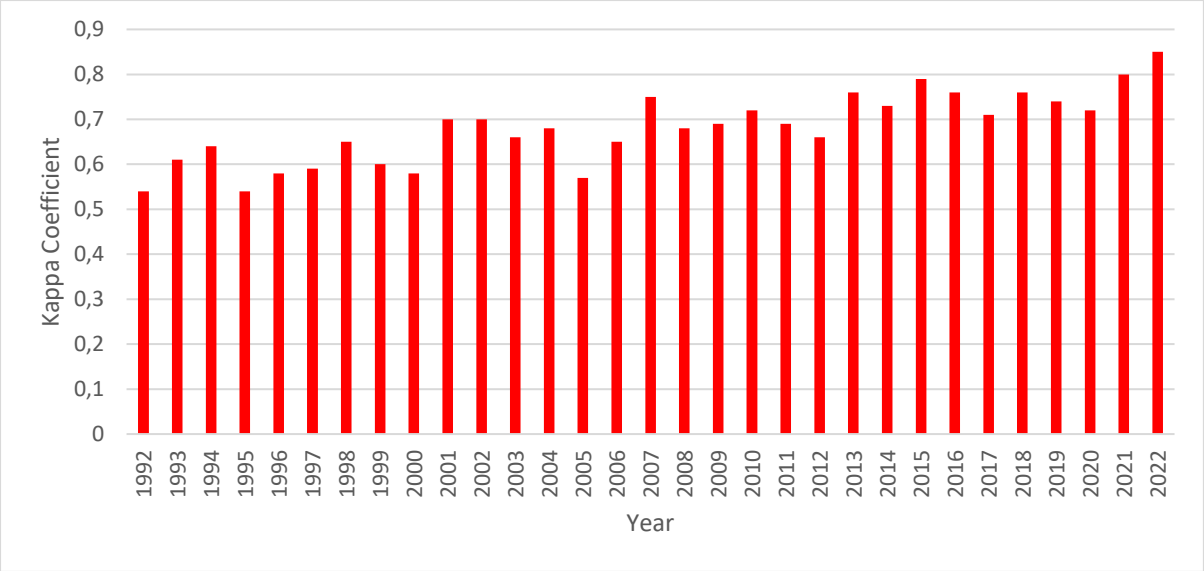


**Figure 8:** Annual Kappa coefficient for LULC classes from RF.

Figure 9 shows the user's accuracy from 1992 to 2022 for the water, bare area, vegetation and salt hardpan classes. The water, bare area, vegetation and salt hardpan classes have an increasing user accuracy trend, indicating that the Random Forest model is improving over time. Figure 10 shows the producer's accuracy from 1992 to 2022 for water, bare area, vegetation and salt hardpan classes. The water, bare area, vegetation and salt hardpan classes have an increasing producer's accuracy trend, indicating the model is improving over time. Figure 11 shows the f1 score from 1992 to 2022 for water, bare area, vegetation and salt hardpan classes. These classes have an increasing f1 score trend, indicating that the model is becoming

effective in correctly classifying positive instances and minimising false positives and false negatives.

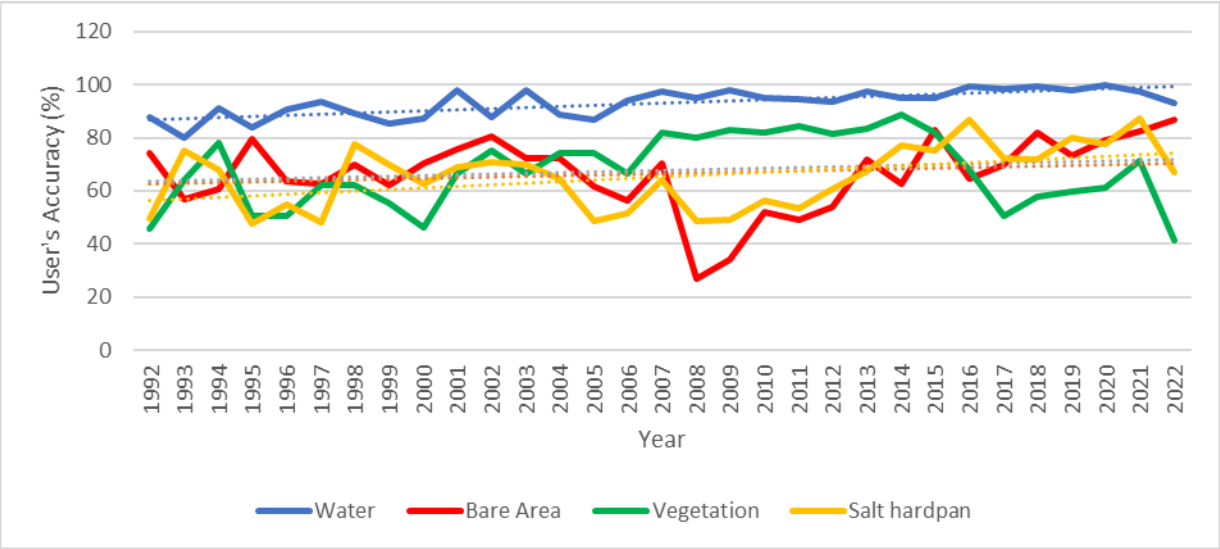


**Figure 9:** Users accuracy for LULC classes from 1992 to 2022.

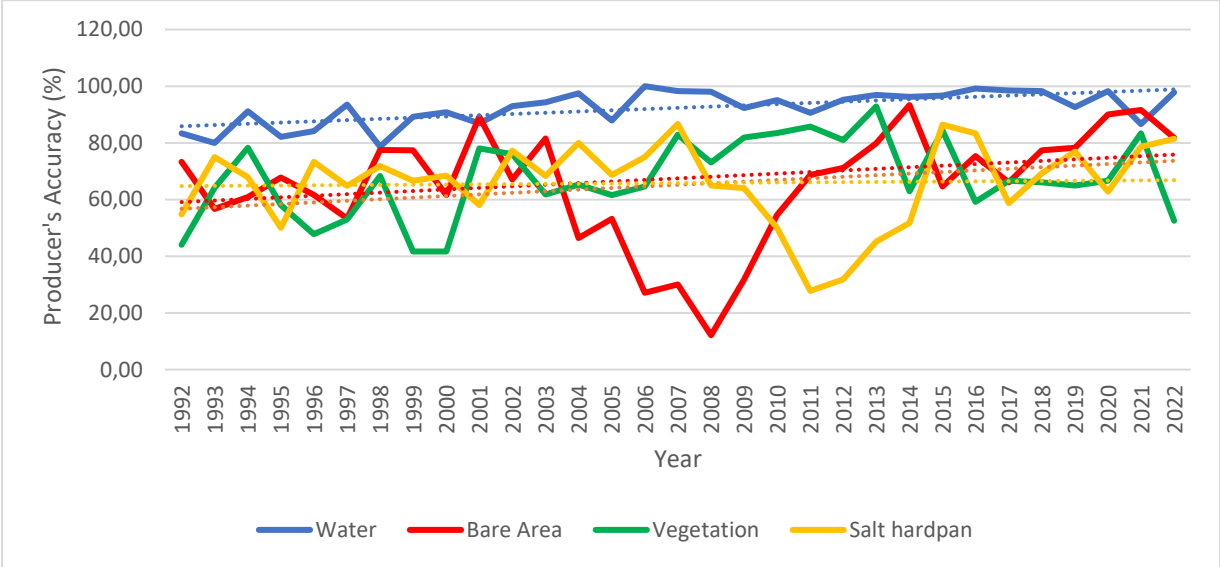


**Figure 10:** Producers accuracy for LULC classes from 1992 to 2022.

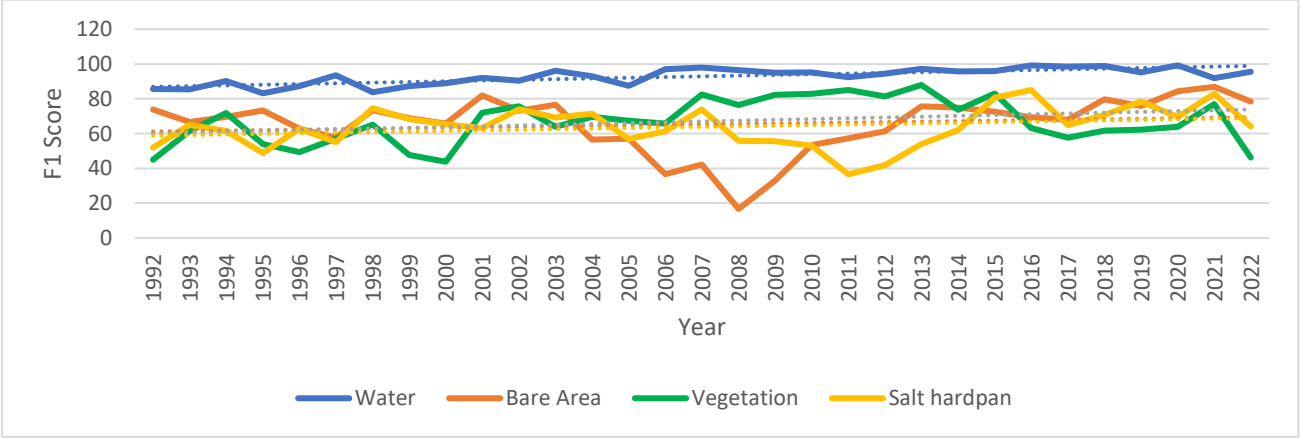


**Figure 11:** F1 score for LULC classes from 1992 to 2022

### 4.2. Annual LULC analysis

Figure 12 shows the derived spectral reflectance for water, bare area, vegetation and salt hardpan, which were considered in this study. The spectral profiles were derived using Landsat 9 OLI. Line plots (Figure 12) show the spectral reflectance values per class of the studied salt pan, indicating that all classes are distinguishable when using the Visible, NIR, SWIR1 and SWIR2 spectral regions. The results indicate that the water class has a low reflectance in the blue region, as water typically absorbs light. Furthermore, the water class has the lowest reflectance of 14% in the NIR region and close to 0 in the SWIR1 and SWIR2 regions due to its strong absorption. The salt class has a typically low reflectance, like the water class in the visible region. However, the water and the salt classes become distinguishable in the SWIR1 and SWIR2 regions, and the salt class has a distinct reflectance. The vegetation class has a relatively low reflectance in the SWIR1 and SWIR2 regions, which could indicate that the vegetation is experiencing stress or drought. The bare area class has the highest reflectance in the SWIR1 region. Overall, the results indicate that water can be distinguished from other land cover types using the SWIR-1 (1566nm) and SWIR-2(2107nm) regions as it has no reflectance.

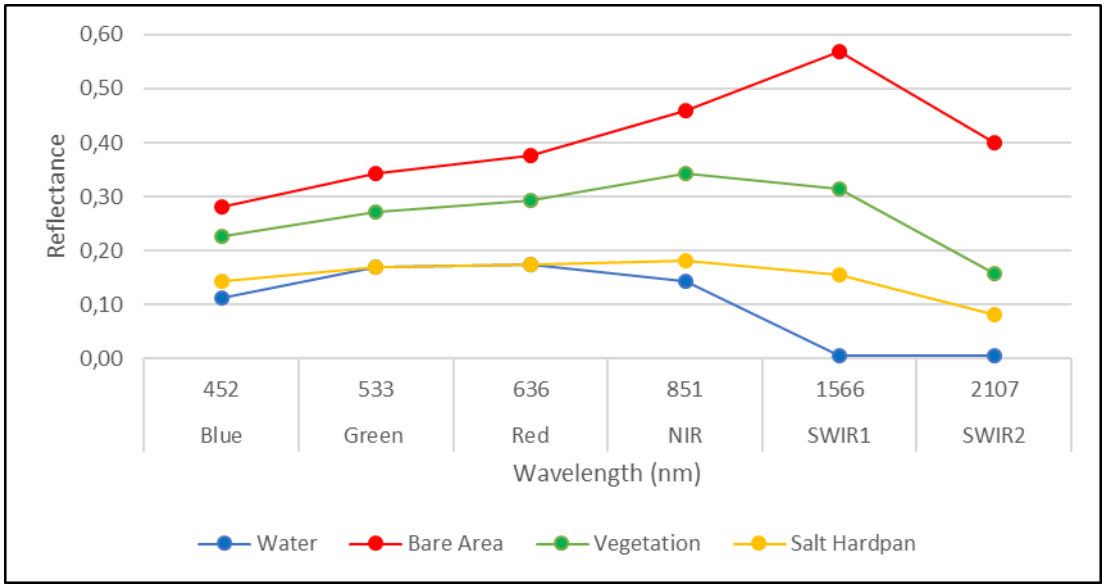


**Figure 12:** Spectral reflectance values extracted from unsupervised classification.

During the study period (1992 – 2022), thirty-one thematic maps were derived using RF classifier and Landsat satellite images to assess the spatiotemporal change analysis of land use/landcover classes in Sua Pan. Figure 13 shows the annual median composite LULC classes using RF.

The results reveal surface water, vegetation, bare area, and salt hardpan coverage fluctuations. On average, surface water is frequently found in the central and northeastern regions of Sua Pan (Figure 13). Figure 13 illustrates vegetation commonly surrounding surface water and bare area and salt hardpan on the periphery of Sua Pan. Surface water area covers approximately 33% of the total surface area, ranging from 19% in 2020 to a maximum of 56% in 2011 and 2014 (Figure 14). Notably, in 2004, 2008, 2010, 2011, 2014, 2017 and 2018, the surface water covers more than 50% of the total surface area.

Years of maximum surface water area coverage include 2000, 2011 and 2014, with 1524 $km^2$, 1846 $km^2$ and 1846 $km^2$ (Figure 14). The years with the minimum surface water area coverage are 1992 and 2020, with areas measuring 625 $km^2$ and 620 $km^2$, respectively. Figure 14 shows that, on average, vegetation occupies approximately 637 $km^2$, showing significant variability over the years. In 1995, vegetation had a maximum of 1405 $km^2$ and a minimum of 119 $km^2$ in 2005. The bare area had an average coverage of approximately 726 $km^2$, experiencing variation; the bare area was at its minimum in 2004 with a coverage of 269 $km^2$ and peaked in 2020 with a coverage of 1214 $km^2$. Similarly, salt hardpan had an average coverage of approximately 750 $km^2$; its maximum surface area was in 1998 with an area of 1322 $km^2$ and lowest in 2017 with an area of 454 $km^2$.

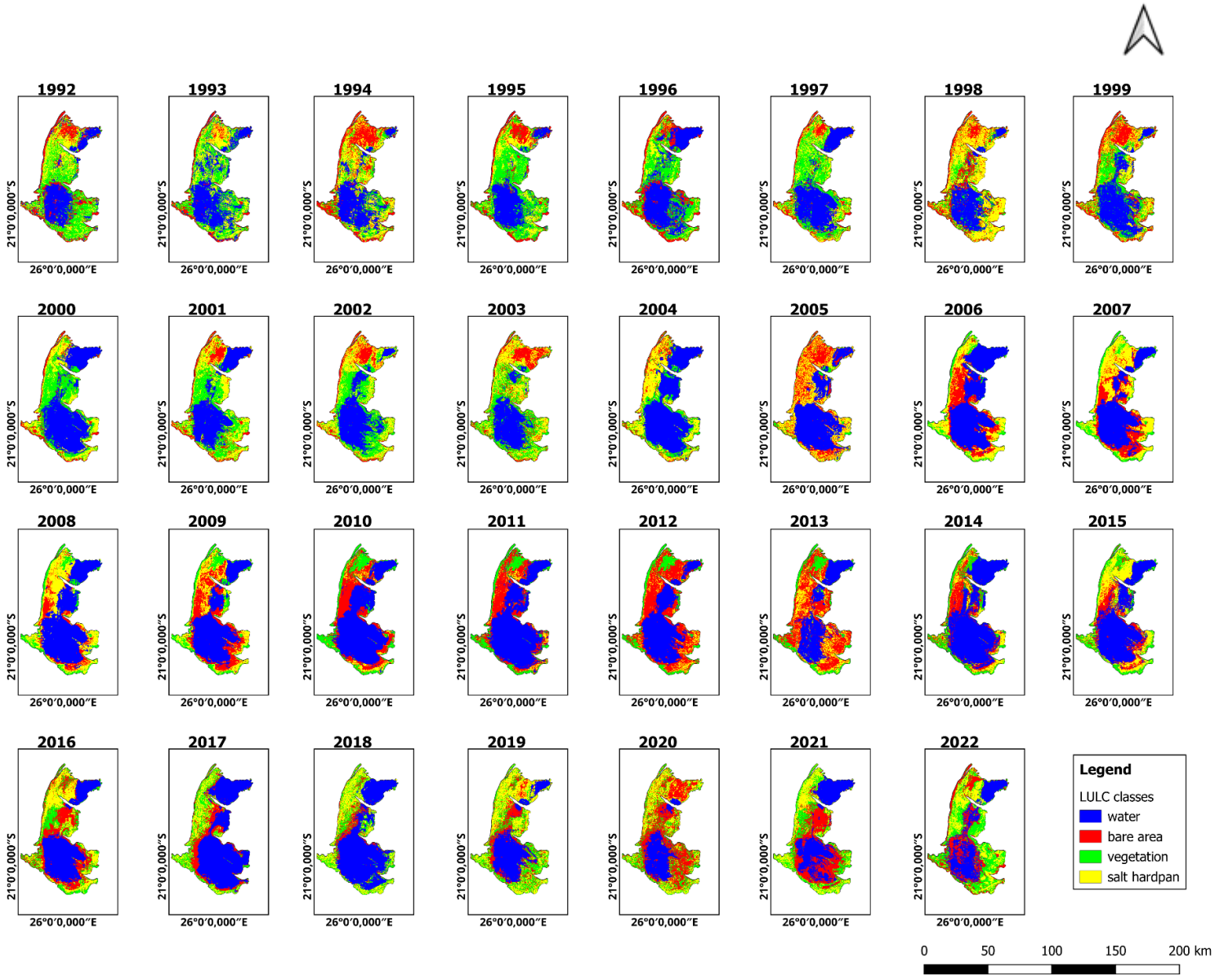


**Figure 13**: Annual (January to December) median composite LULC classes based on RF and Landsat satellite images from 1992 to 2022.

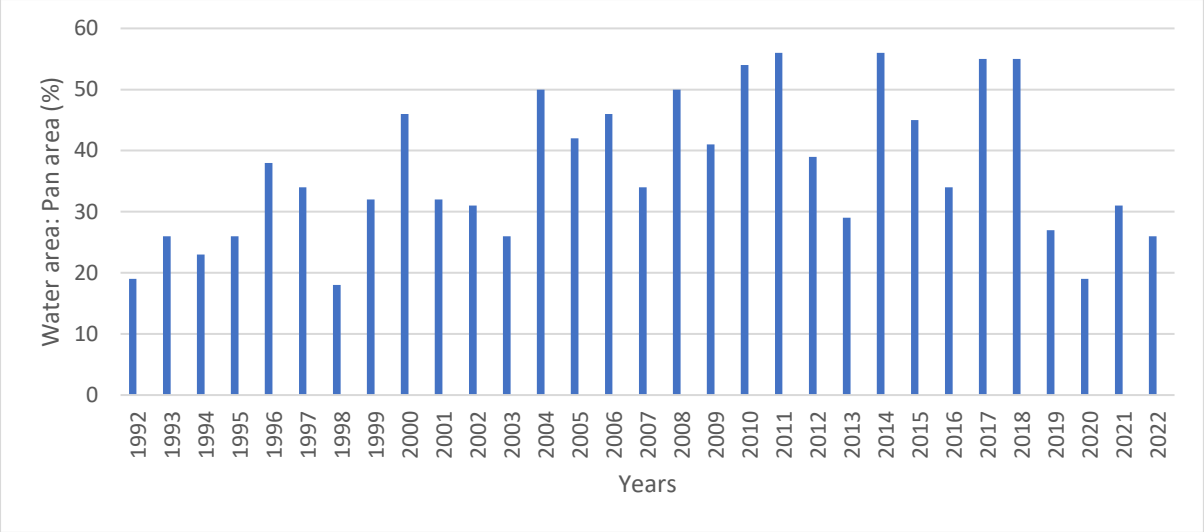


**Figure 14:** Annual (January to December) median composite water body area in proportion to the surface area of Sua Pan. This graph shows the proportion of Sua Pan's surface that is occupied by water bodies throughout the year (from January to December), expressed as a percentage of the pan's total area.

Figure 15 shows the spatiotemporal trend analysis of the area of LULC classes using RF classifier. Surface water has a coefficient of 13.017, indicating an increasing trend suggesting that surface water increases over time. Similarly, bare area has a coefficient of 9.0609, indicating an increasing trend suggesting that bare area increases over time. However, vegetation has a coefficient of -16.786, indicating a decreasing trend and suggesting vegetation decreases over time. Salt hardpan has a coefficient of -5.3081, indicating a decreasing trend suggesting that salt hardpan decreases over time.

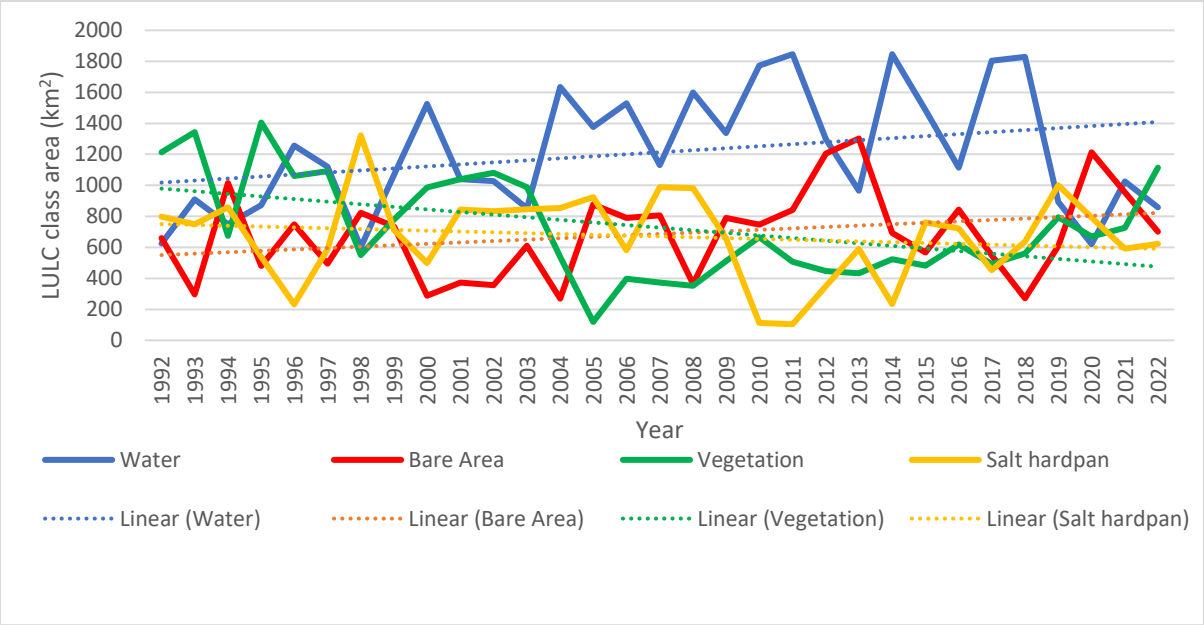


**Figure 15**: Spatiotemporal trend analysis of LULC class area using RF classifier (1992 - 2022).

### 4.3. Surface water area detection and interpretation

#### 4.3.1. Spectral response of surface water using different water indices

The capabilities of MNDWI, NDSI and SWI in detecting water bodies have been examined and compared in this study. Figure 16 shows the spectral reflectance for NDSI, MNDWI and SWI in 2022. In the visible region, the surface water has a similar spectral response to all the indices used. The MNDWI and NDSI have 15% and 11% reflectance values in the NIR region, respectively. In comparison, SWI has a reflectance value of 18% in the same region, which is typically high for a saline environment. MNDWI and NDSI have less than 2% reflectance values in the SWIR1 and SWIR2 regions. SWI has higher reflectance values of 13% and 7% in the SWIR1 and SWIR2 regions, respectively. This indicates the presence of water in the salt pan, including saline water.

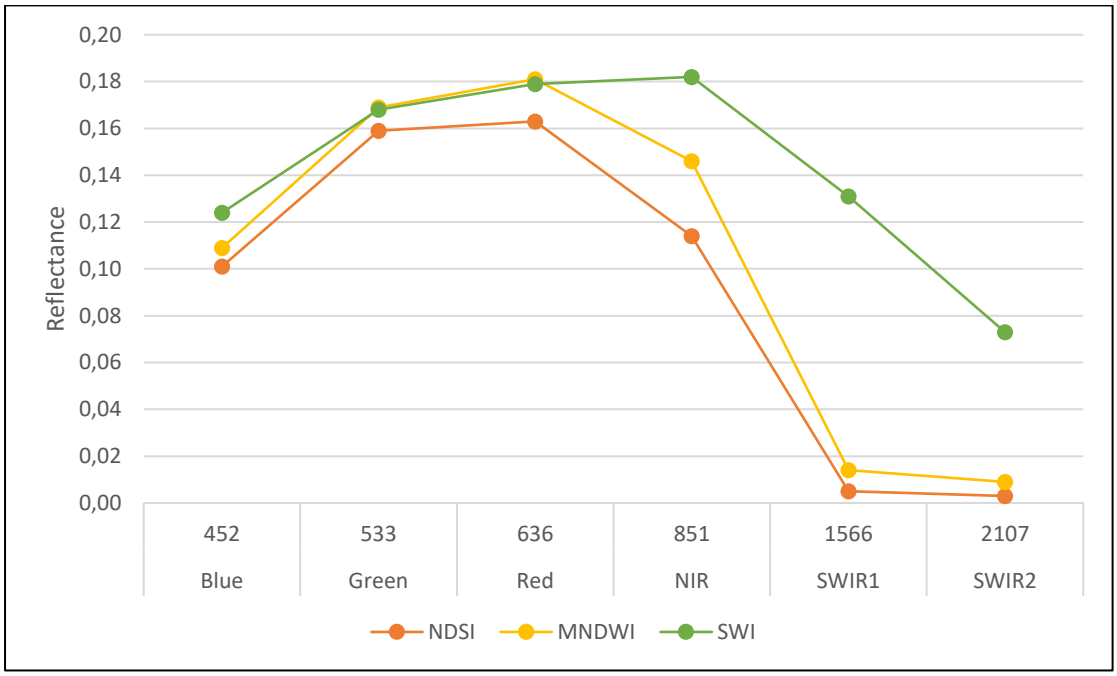


**Figure 16:** Surface water spectral reflectance extracted from NDSI, MNDWI and SWI using Landsat 9 OLI.

The index images and binary classification are shown in Figure 17 using Landsat 9 OLI for 2022 images. MNDWI, NDSI and SWI could detect water in the northeastern part of Sua Pan. MNDWI could detect surface water sparsely in the centre of the pan. NDSI under-detected surface water in the centre of Sua Pan. The SWI detected most surface water in the centre of the pan. All three indices detected surface water in the northeastern part of Sua Pan.

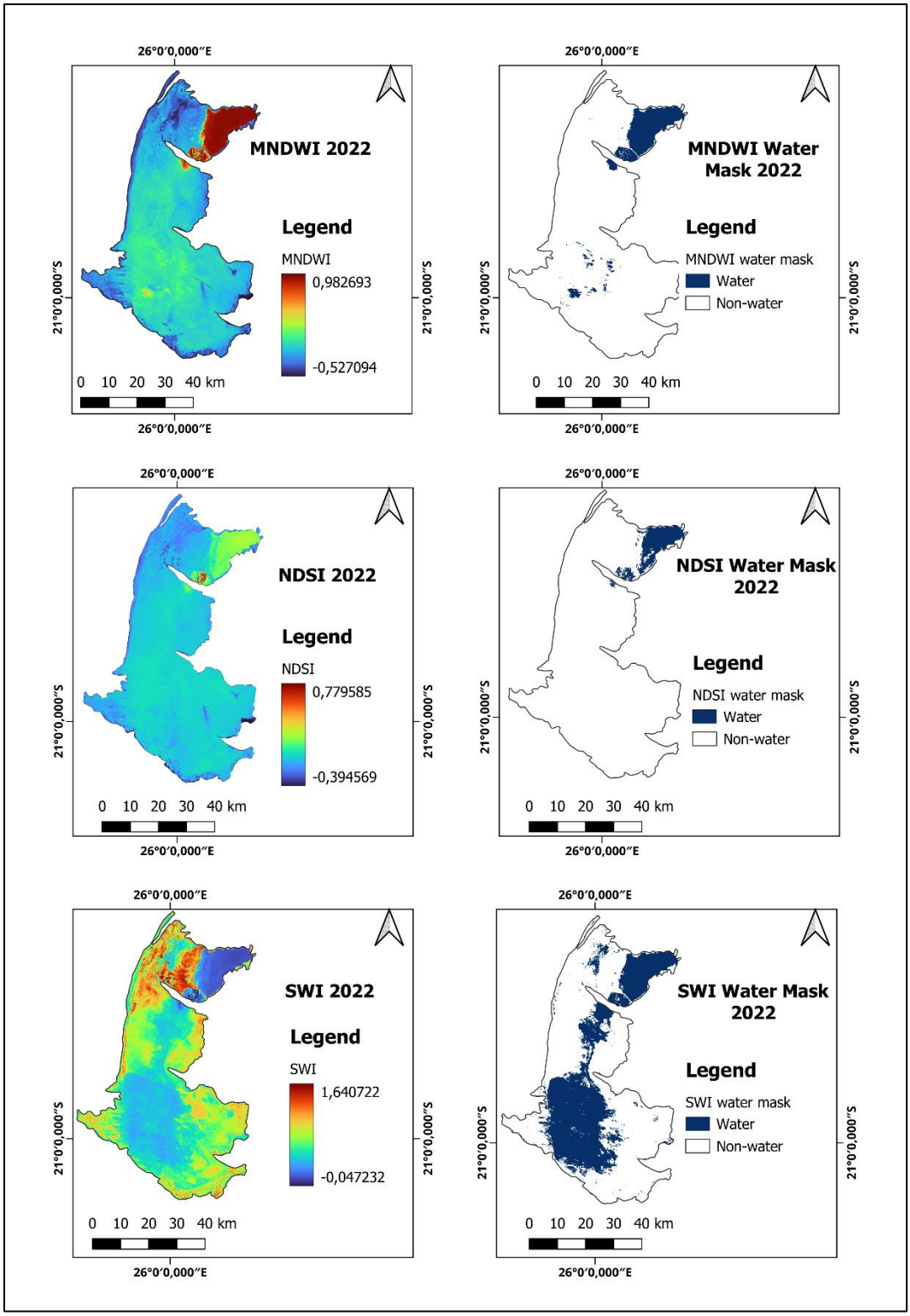


**Figure 17:** 2022 (January to December) median composite images of MNDWI, NDSI and SWI indices and its water mask.

### 4.3.2. Accuracy assessment

Table 5 shows the accuracy assessment performed for the MNDWI, NDSI and SWI using Landsat 9 for 2022. The results show that the overall accuracies range from 59% to 94%. The lowest overall accuracy observed was for NDSI, with 59% and its Kappa coefficient of 0.18. MNDWI had an overall accuracy of 64% and a Kappa coefficient of 0.28. SWI had a higher overall accuracy of 94% and a kappa coefficient of 0.87.

The PA and UA for the three thematic maps range between 21% and 96% for 2022 based on the Landsat 9 composites (Table 5). Moreover, the results show that NDSI has the lowest PA for the water class at 21%, and MNDWI has the lowest UA for the water class at 85%. For the water class, the users' and producers' accuracy for the author's new proposed index (SWI) is 91% and 96%, respectively.

**Table 5:** Confusion matrix for validating the MNDWI, NDSI and SWI maps.

| **MNDWI** | | | | |
|---|---|---|---|---|
| | **Non-water** | **Water** | **Total** | **Users Accuracy** |
| **Non-water** | 94 | 66 | 160 | 59 |
| **Water** | 6 | 34 | 40 | 85 |
| **Total** | 100 | 100 | 200 | |
| **Producers Accuracy** | 94 | 34 | | |
| **Overall Accuracy** | 64 | | | |
| **Kappa** | 0.28 | | | |
| **NDSI** | | | | |
| | **Non-water** | **Water** | **Total** | **Users Accuracy** |
| **Non-water** | 97 | 79 | 176 | 55 |
| **Water** | 3 | 21 | 24 | 88 |
| **Total** | 100 | 100 | 200 | |
| **Producers Accuracy** | 97 | 21 | | |
| **Overall Accuracy** | 59 | | | |
| **Kappa** | 0.18 | | | |
| **SWI** | | | | |
| | **Non-water** | **Water** | **Total** | **Users Accuracy** |
| **Non-water** | 91 | 4 | 95 | 96 |
| **Water** | 9 | 96 | 105 | 91 |
| **Total** | 100 | 100 | 200 | |

| | | | | |
|---|---|---|---|---|
| **Producers Accuracy** | 91 | 96 | | |
| **Overall Accuracy** | 94 | | | |
| **Kappa** | 0.87 | | | |

To assess the statistically significant differences between the validation data set and MNDWI, NDSI and SWI, this study calculated McNemar's chi-square test. MNDWI ( $\boldsymbol{X^2}$ = 48.347, p < 0.0001, degrees of freedom (d.f.) = 1) and NDSI ($\boldsymbol{X^2}$ = 68.598, p < 0.0001, degrees of freedom (d.f.) = 1) had a significant statistical difference with the validation dataset (Table 6). In comparison, the SWI ($\boldsymbol{X^2}$ = 1.2308, p = 0.2673, degrees of freedom (d.f.) = 1) had no significant statistical difference with the validation dataset. This indicates that the SWI is not far from the truth.

**Table 6:** Chi-square results of binary (water and non-water) classification using Landsat 9 data.

| **Index** | **Land-cover class** | **Threshold** | **OA (%)** | $\boldsymbol{\kappa}$ | $\boldsymbol{\rho}$ | $\boldsymbol{X^2}$ |
|---|---|---|---|---|---|---|
| **MNDWI** | **Water Non-water** | ≥ 0.1 | 64 | 0.28 | <0.0001 | 48.347, df = 1 |
| **NDSI** | **Water Non-water** | ≥ 0.1 | 59 | 0.18 | <0.0001 | 68.598, df = 1 |
| **SWI** | **Water Non-water** | ≤ 0.4 | 94 | 0.87 | 0.2673 | 1.2308, df = 1 |

### 4.4. Spatiotemporal analysis of surface water area using Saline Water Index (SWI) during the wet and dry seasons

This study uses remote sensing data and techniques for the seasonal spatiotemporal monitoring of surface water in Sua Pan. The Saline Water Index had the highest overall accuracy of 94%. Therefore, this study used the SWI to map surface water during the wet and dry seasons using Landsat 5,7,8 and 9 median composites. In Figure 18, the surface water area is portrayed in blue. The visual results indicate that surface water has varied from 1992 to 2022. It is visually evident that 1992 was the driest year for Sua Pan.

The average surface water area from 1992 to 2022 for the wet season was 1404,76 $km^2$, and for the dry season, 447,21 $km^2$. The maximum surface water area for the wet season was estimated at 2644,59 $km^2$ in 2017. For the dry season, the maximum surface water estimated was 1549,788 $km^2$ for 2017. The lowest surface water area estimated was 190,698 $km^2$ (1996) for the wet season and 26,381 $km^2$ for the dry season in 2005. In 1992, the surface water area was 544 $km^2$ during wet season and 59 $km^2$ during dry season.

In 1992, 1995 and 2003, no surface water was detected in the northeastern part of the pan in both the wet and dry seasons. Following this, the total surface water area for both the wet and dry seasons was below 600 $km^2$, approximately 2000 $km^2$ less than the maximum surface water area. Figure 19 shows the surface water area trend analysis for the wet and dry seasons from 1992 to 2022. The results show that surface water area during the wet season has a higher trend with a slope of 32,667x. The dry season has a slightly increasing trend with a slope of 1,9901x.

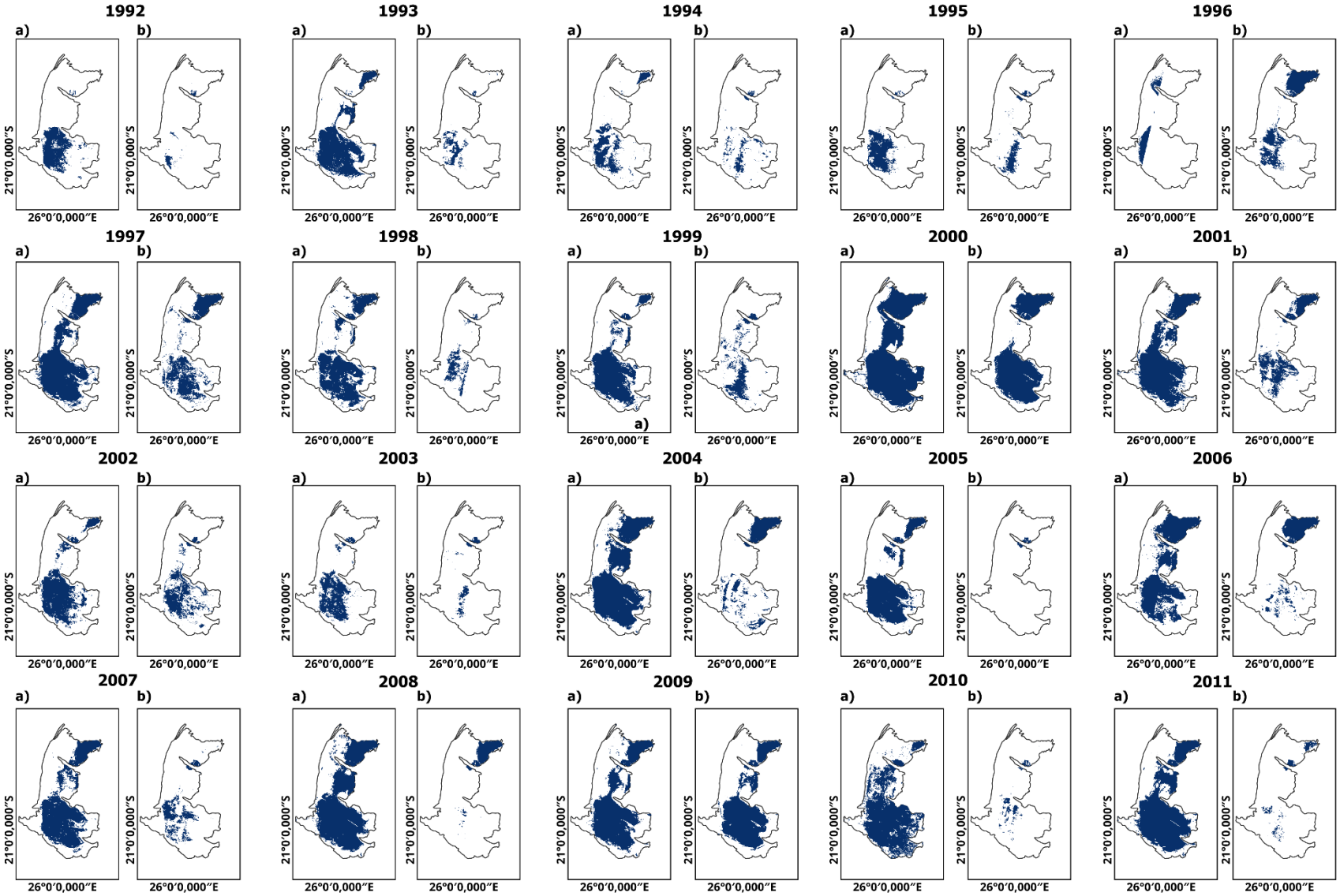
1992
1993
1994
1995
1996
1997
1998
1999
2000
2001
2002
2003
2004
2005
2006
2007
2008
2009
2010
2011
a)
b)
21°0′0,000″S
26°0′0,000″E

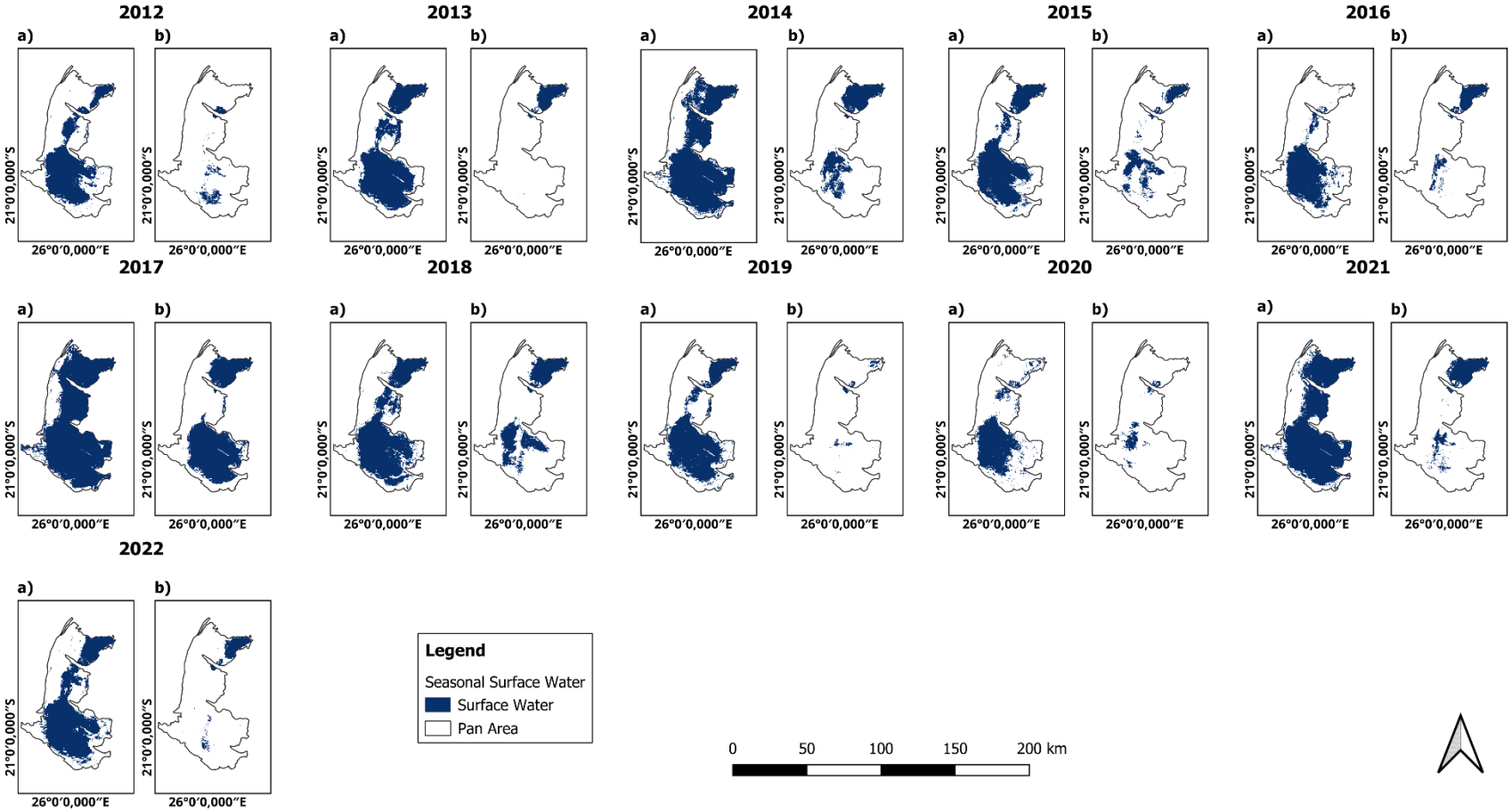


**Figure 18:** Spatiotemporal maps of surface water area using SWI during the a) wet season (January to March) and b) dry season (August to October) from 1992 to 2022.

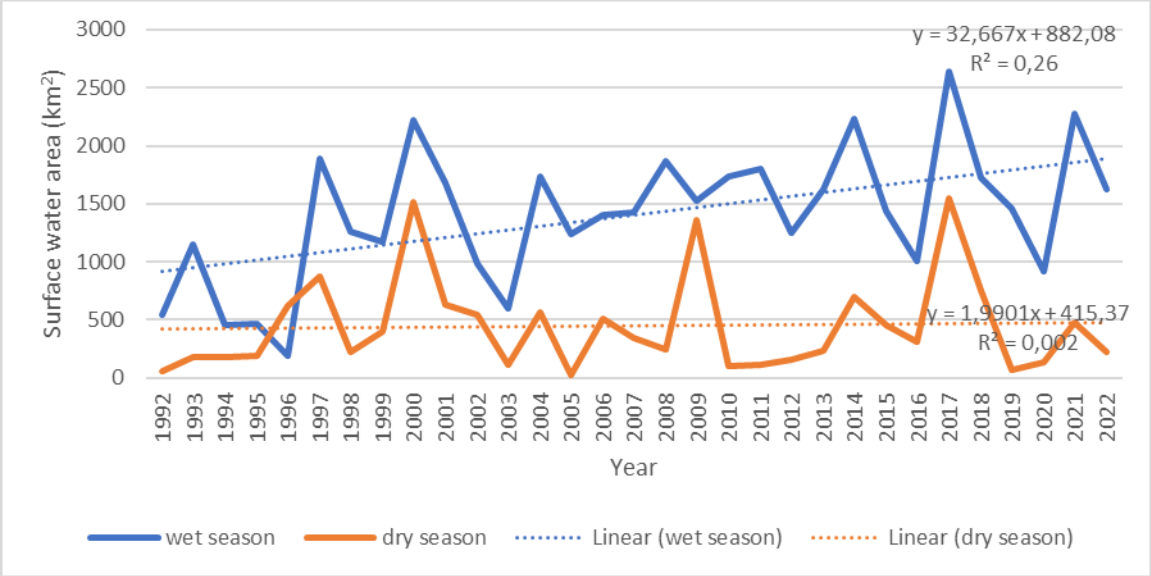


**Figure 19:** Spatiotemporal analysis of surface water area using SWI during the wet and dry seasons.

### 4.4.1. Homogeneity testing

The wet season's Standard Normal Homogeneity Test (SHNT) and Buishand's homogeneity tests for Sua Pan suggest that the surface water area is not homogeneous, and abrupt changes occurred in 1994 and 2003, respectively (Table 7). The computed *p-values* using the SNHT and Buishand tests were 0,000 and 0,029, respectively (Table 7). In comparison, the Pettitt test computed that the data are homogenous with a *p-value* of 0,109. The dry season's Pettitt, SHNT and Buishand homogeneity tests for Sua Pan suggest that the surface water area is homogeneous with computed *p-values* of 0.673, 0.695 and 0.859, respectively.

**Table 7:** Homogeneity tests for surface water area from 1992 to 2022

| **Wet Season** | | | | |
|---|---|---|---|---|
| | *P-value* | Alpha (α) | Confidence level | Test Decision |
| Pettitt | 0,109 | 0,05 | 99% | *p-value* > α, fail to reject null hypothesis $H_0$. |
| SNHT test | **0,000** | 0,05 | 99% | *p-value* < α, reject the null hypothesis $H_0$. |

| | | | | |
|---|---|---|---|---|
| | | | | Change point 1996 |
| Buishand | **0,029** | 0,05 | 99% | *p-value* < α, reject the null hypothesis $H_0$. Change point 2003 |
| **Dry Season** | | | | |
| | *P-value* | Alpha (α) | Confidence level | Test Decision |
| Pettitt | 0,673 | 0,05 | 99% | *p-value* > α, fail to reject null hypothesis $H_0$. |
| SNHT test | 0,695 | 0,05 | 99% | *p-value* > α, fail to reject null hypothesis $H_0$. |
| Buishand | 0,859 | 0,05 | 99% | *p-value* > α, fail to reject null hypothesis $H_0$. |

### 4.4.2. Trend analysis and descriptive statistics

The trend analysis, CV, minimum, maximum and mean of seasonal surface water from 1992 to 2022 are presented in Table 8. The computed *p-value* was 0,01 and tau 0,329 for the wet season. According to the Mann-Kendall test, there is a statistically significant, weak positive monotonic trend in the wet season of the surface water area using SWI. For the dry season, the computed *p-value* was 0,734 and tau 0,043. A very weak positive monotonic trend is not statistically significant for the dry season.

The wet season had a CV of 29,17%, indicating moderate variability in the surface water area obtained. The dry season had a CV of 91,24%, indicating relatively high variability in surface water area. Minimum values were reported as 190,7 $km^2$ and 26,38 $km^2$ for the wet and dry seasons, respectively. The maximum area values were 2644,59 $km^2$ for the wet season and

1549,79 $km^2$ for the dry season. The average values were 1404,76 $km^2$ and 713.06 $km^2$ for the wet and dry seasons.

**Table 8:** Trend analysis and descriptive statistics

| Series\Test | Kendall's tau | *p-value* | CV | Min $km^2$ | Max $km^2$ | Mean $km^2$ |
|---|---|---|---|---|---|---|
| **Wet** | 0,329 | 0,01 | 29,17 | 190,7 | 2644,59 | 1404,76 |
| **Dry** | 0,045 | 0,734 | 91,24 | 26,38 | 1549,79 | 713,06 |

### 4.5. Using cloud computing remote sensing climate data and ENSO to assess the influence on surface water area

#### 4.5.1. Relationship between ENSO, rainfall and surface water area during the wet and dry seasons

Figure 20 shows the ONI index for the wet season from 1992 to 2022. The positive values shown represent the El Niño phases, and the negative values represent the La Niña phases. Figures 19 and 21 are line graphs depicting the temporal variation of surface water area ($km^2$) and rainfall (mm) during the wet seasons from 1992 to 2022.

The results indicate a varying relationship between ENSO, rainfall and surface water area during the wet season. Strong El Niño events of 1.63 and 1.93 anomalies occurred in 1992 and 1998, respectively and are associated with 64mm and 186mm rainfall and a surface water area of 544 $km^2$ and 1265 $km^2$. In 2016, a very strong El Niño event occurred with an anomaly of 2.14, rainfall of 333mm and a surface water area of 1010 $km^2$.

In 1998, 1999, and 2007, a moderate La Niña event occurred with anomalies of -1.31, -1.16 and -1.07, respectively. The rainfall for these years was 186mm, 195mm and 128mm and surface water areas of 1265 $km^2$, 1176 $km^2$ and 1421 $km^2$. In 2008, the strongest La Niña event occurred during the study period with an anomaly of -1.52. The rainfall for the wet season in 2008 was 300mm, and a surface water area of 1863 $km^2$.

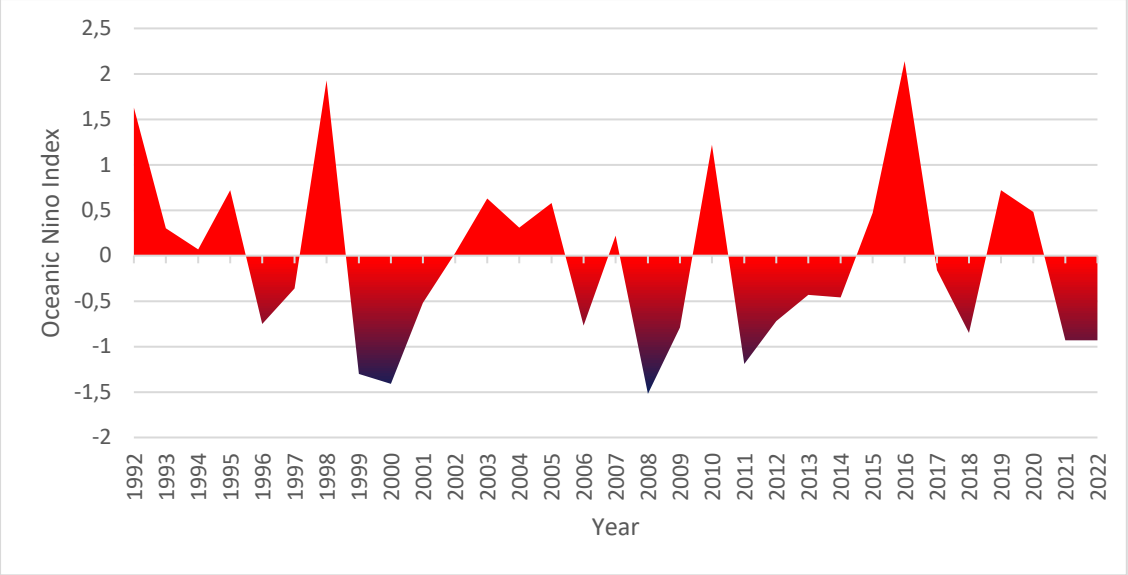


**Figure 20:** Wet season (January to March) ONI anomalies. Red illustrates El Niño and blue illustrates La Niña.

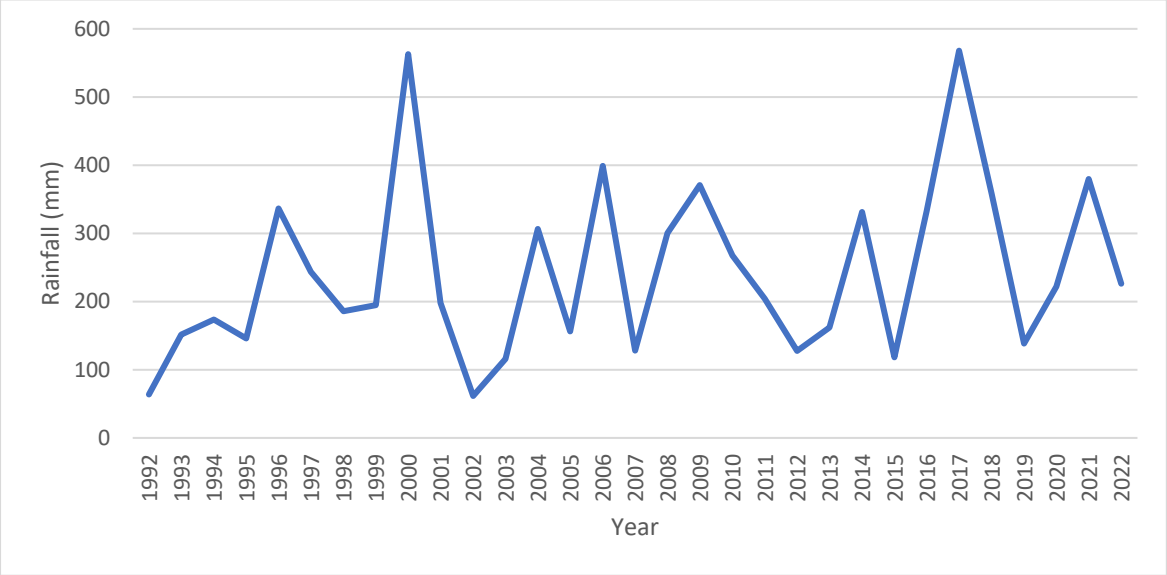


**Figure 21:** Rainfall (mm) during the wet season (January to March).

Figure 22 shows the Ocean Nino Index (ONI) index for the dry season from 1992 to 2022. The positive values represent the El Niño phases, and the negative values represent the La Niña phases. Figures 23 and 19 are line graphs depicting the temporal variation of rainfall (mm) and surface water area ($km^2$) during the dry seasons from 1992 to 2022.

The ENSO values fluctuate around neutral conditions from 1992 to 1996. Very strong El Niño events of 2.14 and 2.16 anomalies occurred in 1997 and 2015, respectively and are associated with 30.2mm and 11.7mm and a surface water area of 878 $km^2$ and 459 $km^2$.

In 1998, a moderate La Niña event occurred with an anomaly of -1.31, reflecting the transition to La Niña conditions. 1999, 2000 and 2001, there was a period of moderate to weak La Niña conditions with anomalies of -1.16, -0.55 and -0.19, respectively. In 2010, a strong La Niña event occurred with an anomaly of -1.56, rainfall of 21.1mm and a surface water area of 105 $km^2$.

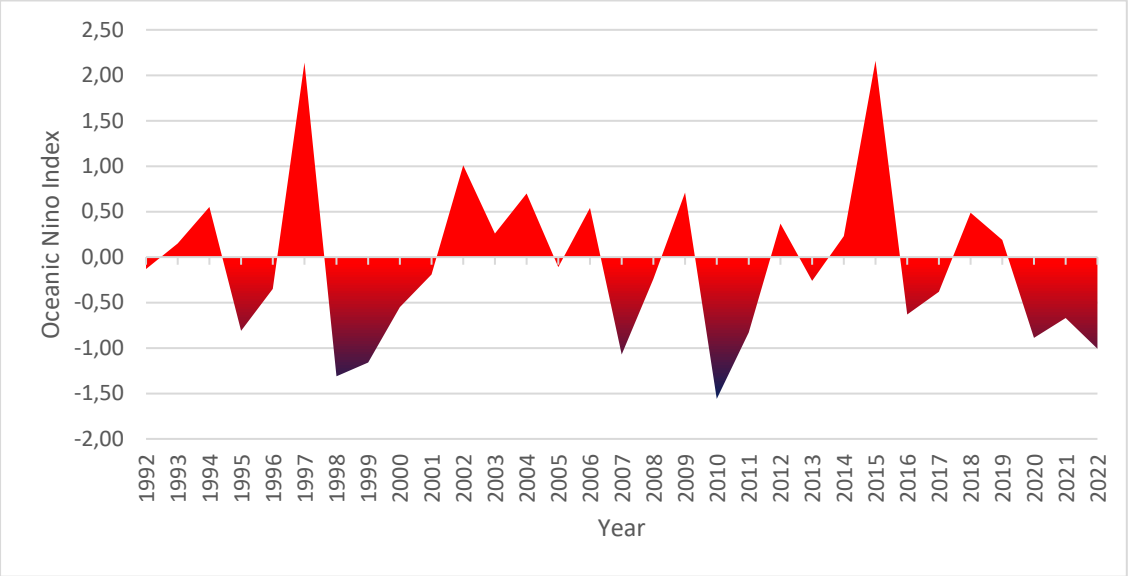


**Figure 22:** Dry season (August to October) ONI anomalies. Red illustrates El Niño and blue illustrates La Niña.

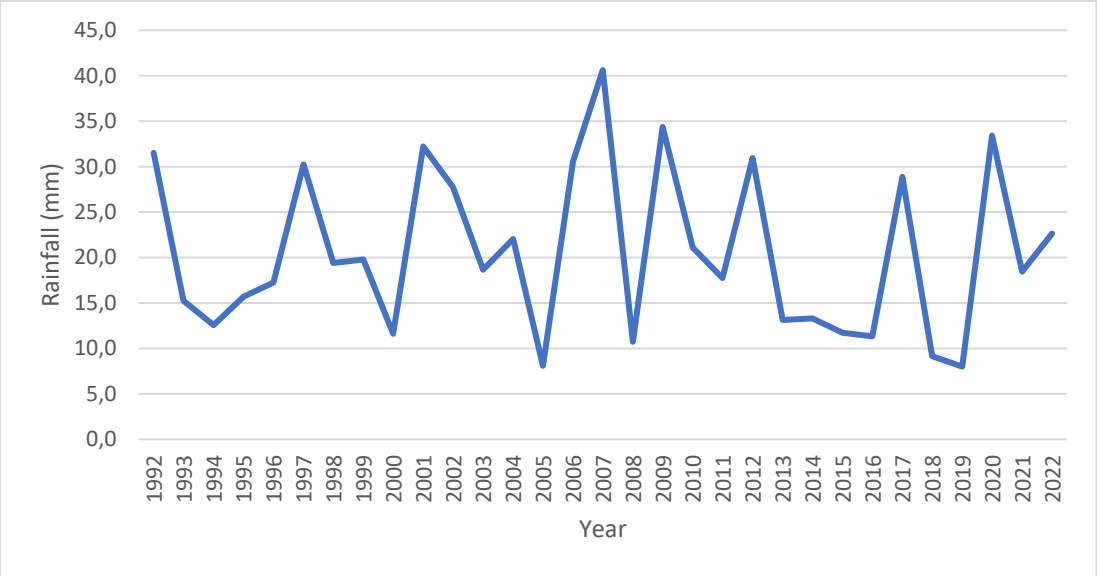


**Figure 23:** Rainfall (mm) during the dry season (August to October).

### 4.5.2. Statistical relationship between ONI and surface water area and Rainfall over Sua Pan through the Period (1992-2022)

Figure 24 illustrates the ENSO events between 1992 and 2022. Notably, the period is dominated by La Niña events, with four strong La Niña events in 1998-1999, 1999-2000, 2007-2008 and 2010-2011. Compared to three moderate El Niño events in 1994-1995, 2002-2003 and 2009-2010 and two very strong El Niño events in 1997-1998 and 2015-2016. Overall, the graph shows the fluctuating nature of the ENSO cycle.

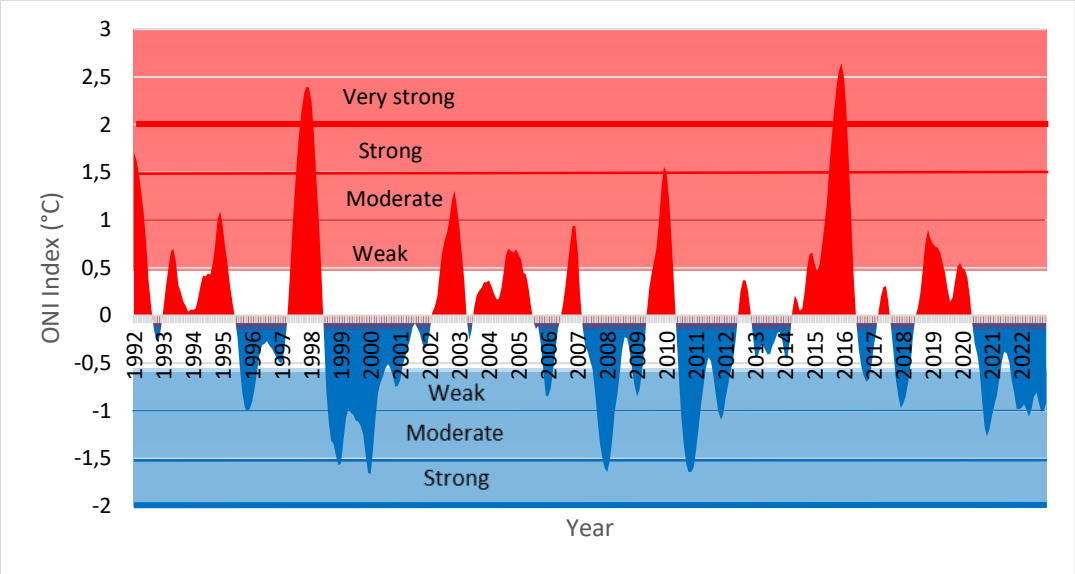


**Figure 24:** The ONI with El Niño and La Niña strength years through the study period (1992–2022).

To investigate the impact of ENSO events on rainfall and surface water area, ANOVA and Tukey analysis were conducted to examine which ENSO phases directly influence rainfall and surface water area. Based on the ANOVA_Rainfall results (Table 9), the computed *p-value* $0.667 > 0.05$ suggests that no statistically significant evidence suggests that the different ENSO phases significantly impact rainfall. Tukey's post-hoc results (Table 10) provide insight into the relationship between ENSO phases and rainfall. The ANOVA_Rainfall test was unable to find an overall difference. Tukey's post-hoc_Rainfall results (Table 10) provide further insights, showing no statistically significant differences in mean rainfall and any specific pairs of ENSO phases such as Moderate La Niña versus Moderate El Niño, Strong El Niño versus Moderate El Niño, Strong La Niña versus Moderate El Niño, Very strong El Niño versus Moderate El Niño, Strong El Niño versus Moderate La Niña, Strong La Niña versus Moderate La Niña, Very strong El Niño versus Moderate La Niña, Strong La Niña versus Strong El Niño, Very strong El Niño versus Strong El Niño, and Very strong El Niño versus Strong La Niña.

This is supported by the adjusted p-values in Table 10, all greater than the 0.05 significance level.

**Table 9:** ANOVA_Rainfall results of ENSO phenomena on rainfall

| Source | Df | Sum Sq | Mean Sq | F value | Pr(>F) |
|---|---|---|---|---|---|
| **ENSO** | 4 | 97381 | 24345 | 0.609 | 0.667 |
| **Residuals** | 9 | 359874 | 39986 | | |

**Table 10:** Post-hoc_Rainfall Multiple Comparisons of Mean Differences in Rainfall Between ENSO Categories

| ***Comparison (ENSO categories)*** | **Difference in means (diff)** | **Lower confidence interval (lwr)** | **Upper confidence interval (upr)** | **Adjusted *p-value* (p adj)** |
|---|---|---|---|---|
| ***ModerateLa Niña - ModerateEl Niño*** | 167.5 | -346.05 | 681.05 | 0.8043 |
| ***StrongEl Niño - ModerateEl Niño*** | -64 | -840.42 | 712.42 | 0.9984 |
| ***StrongLa Niña - ModerateEl Niño*** | 176.25 | -337.3 | 689.8 | 0.7757 |
| ***Very strongEl Niño - ModerateEl Niño*** | 105 | -508.81 | 718.81 | 0.9756 |
| ***StrongEl Niño - ModerateLa Niña*** | -231.5 | -983.26 | 520.26 | 0.8332 |
| ***StrongLa Niña - ModerateLa Niña*** | 8.75 | -466.71 | 484.21 | 0.9999 |
| ***Very strongEl Niño - ModerateLa Niña*** | -62.5 | -644.81 | 519.81 | 0.9957 |
| ***StrongLa Niña - StrongEl Niño*** | 240.25 | -511.51 | 992.01 | 0.8149 |
| ***Very strongEl Niño - StrongEl Niño*** | 169 | -654.52 | 992.52 | 0.9537 |
| ***Very strong El Niño - Strong La Niña*** | -71.25 | -653.56 | 511.06 | 0.9929 |

The ANOVA_SurfaceWaterArea results (Table 11) show a computed *p-value* of 0.753 > 0.05 suggesting no statistically significant evidence that the different ENSO phases impact surface water area.

**Table 11:** ANOVA_SurfaceWaterArea results of ENSO phenomena on surface water area

| ***Source*** | ***Df*** | ***Sum Sq*** | ***Mean Sq*** | ***F value*** | ***Pr(>F)*** |
|---|---|---|---|---|---|
| ***ENSO*** | 4 | 366249 | 91562 | 0.475 | 0.753 |
| ***Residuals*** | 9 | 1733414 | 192602 | | |

Tukey's post-hoc_SurfaceWaterArea results (Table 12) provide further insight into the relationship between ENSO phases and surface water area. The ANOVA_SurfaceWaterArea test was unable to find an overall difference. Similarly, Tukey's post-hoc_SurfaceWaterArea test results (Table 12) reveal individual comparisons between specific ENSO phases, such as Moderate La Niña versus Moderate El Niño, Strong El Niño versus Moderate El Niño, Strong La Niña versus Moderate El Niño, Very strong El Niño versus Moderate El Niño, Strong El Niño versus Moderate La Niña, Strong La Niña versus Moderate La Niña, Very strong El Niño versus Moderate La Niña, Strong La Niña versus Strong El Niño, Very strong El Niño versus Strong El Niño, and Very strong El Niño versus Strong La Niña, show no statistically significant differences in mean surface water area. This is supported by the adjusted p-values in Table 12, all greater than the 0.05 significance level.

**Table 12:** Post-hoc_SurfaceWaterArea Multiple Comparisons of Mean Differences in surface water area Between ENSO Categories

| *ENSO Comparison* | *Difference (diff)* | *Lower Confidence Interval (lwr)* | *Upper Confidence Interval (upr)* | *Adjusted p-value (p adj)* |
|---|---|---|---|---|
| ***ModerateLa Niña - ModerateEl Niño*** | 191.75 | -935.35 | 1318.85 | 0.976 |
| ***StrongEl Niño - ModerateEl Niño*** | -164 | -1868.01 | 1540.01 | 0.997 |
| ***StrongLa Niña - ModerateEl Niño*** | 281.5 | -845.6 | 1408.6 | 0.911 |
| ***Very strongEl Niño - ModerateEl Niño*** | 413.5 | -933.64 | 1760.64 | 0.835 |
| ***StrongEl Niño - ModerateLa Niña*** | -355.75 | -2005.65 | 1294.15 | 0.945 |
| ***StrongLa Niña - ModerateLa Niña*** | 89.75 | -953.74 | 1133.24 | 0.998 |
| ***Very strongEl Niño - ModerateLa Niña*** | 221.75 | -1056.26 | 1499.76 | 0.974 |
| ***StrongLa Niña - StrongEl Niño*** | 445.5 | -1204.4 | 2095.4 | 0.887 |
| ***Very strongEl Niño - StrongEl Niño*** | 577.5 | -1229.87 | 2384.87 | 0.815 |
| ***Very strongEl Niño - StrongLa Niña*** | 132 | -1146.01 | 1410.01 | 0.996 |

### 4.5.3. Pearson’s correlation of climate variables, ENSO and surface water area

Table 13 represents Pearson's correlation matrix for climate variables, ENSO and surface water area in the wet and dry seasons. Land surface temperatures and surface water area have a strong negative correlation during the wet season (-0,791) and dry season (-0,699). During the wet season, surface water area and rainfall have a strong positive correlation (0,661), compared to the dry season with a moderate positive correlation (0,328). Surface water area and evapotranspiration have a strong positive relationship in the wet season (0,803) and dry (0,714) season. Surface water area and ENSO have a moderate negative correlation (-0,464) in the wet season and a weak to moderate positive correlation (0,290) in the dry season.

**Table 13:** Pearson Correlation analysis of climate variables and surface water area for wet and dry seasons.

| **Wet Season** | | | | | | | | | | |
|---|---|---|---|---|---|---|---|---|---|---|
| | **LST** | | **Rainfall** | | **Evapotranspiration** | | **ENSO** | | **SWA** | |
| | *p-value* | Pearson's r | *p-value* | Pearson's r | *p-value* | Pearson's r | *p-value* | Pearson's r | *p-value* | Pearson's r |
| **LST** | 0 | 1 | | | | | | | | |
| **Rainfall** | **<0.0001** | **-0,867** | 0 | 1 | | | | | | |
| **Evapotranspiration** | **<0.0001** | **-0,954** | **<0.0001** | **0,856** | 0 | 1 | | | | |
| **ENSO** | **0,013** | **0,521** | 0.02963 | -0,391 | **0,010** | **-0,537** | 0 | 1 | | |
| **SWA** | **<0.0001** | **-0,791** | **0,001** | **0,593** | **<0.0001** | **0,803** | **0,030** | **-0,464** | 0 | 1 |
| **Dry Season** | | | | | | | | | | |
| | **LST** | | **Rainfall** | | **Evapotranspiration** | | **ENSO** | | **SWA** | |
| | *p-value* | Pearson's r | *p-value* | Pearson's r | *p-value* | Pearson's r | *p-value* | Pearson's r | *p-value* | Pearson's r |
| **LST** | 0 | 1 | | | | | | | | |
| **Rainfall** | 0,275 | -0,244 | 0 | 1 | | | | | | |
| **Evapotranspiration** | **0,001** | **-0,676** | **0,044** | **0,434** | 0 | 1 | | | | |
| **ENSO** | 0,940 | 0,017 | 0,487 | -0,157 | 0,606 | -0,116 | 0 | 1 | | |
| **SWA** | **0,000** | **-0,699** | 0,136 | 0,328 | **0,000** | **0,714** | 0,191 | 0,290 | 0 | 1 |

## Chapter 5: Discussion

### 5.1. GEE and Machine Learning (Random Forest) for LULC from 1992 to 2022

This study demonstrates the effectiveness of GEE for LULC change detection in Sua Pan. The introduction of GEE, a cloud-computing platform, provides various advantages like advanced machine-learning algorithms, parallel processing, memory efficiency, and fast image processing power (Gxokwe *et al*., 2022). The RF classification's overall accuracy varied from 65.2% to 85.09%, and the Kappa coefficient ranged from 0.54 to 0.85. These values indicate moderate to substantial agreement between the classified maps and reference data (Rwanga and Ndambuki, 2017). Notably, accuracy improved over time, with Landsat 8 OLI imagery achieving the highest overall accuracy (79.2% - 85.09%) and Kappa coefficient (0.71 - 0.80). A study by Malahlela *et al*. (2018) suggests that Landsat OLI has an improved noise-to-signal ratio compared to other Landsat satellite data. This suggests a potential improvement in land cover types' spectral separability with additional bands in later Landsat satellites (Wulder *et al*., 2022).

Further insights are provided by the user's and producer's accuracy, which generally increased over time for all land cover classes (water, bare area, vegetation, and salt hardpan). Patel *et al*. (2024) mention that increased accuracy indicates the model's ability to correctly classify these classes as it improved throughout the study period. The analysis revealed a rising F1 score, signifying a significant improvement in the model's overall performance. The F1 score considers both precision (correctly identified positive instances) and recall (identification of all positive instances) – a critical advantage for tasks where both aspects are equally important. This increase suggests that the model became more effective in accurately classifying positive instances while minimising false positives (incorrectly classified positive instances) and false negatives (missed positive instances).

The observed increase in rainfall of approximately 150 mm between 2007 and 2008 during the wet season had a significant impact on LULC classification accuracy, particularly affecting the bare area class. This change in rainfall led to a notable spike in vegetation growth from 2008 to 2009, altering the landscape. In arid and semi-arid regions, such substantial increase in rainfall can cause a vegetation response, as noted by Zhang *et al*. (2004). The resulting seasonal vegetation cover in areas typically classified as bare areas altered their spectral signatures. This shift in landcover characteristics increased misclassification with bare area being incorrectly

identified as vegetation. The impact of these changes is reflected in user's accuracy, producer's accuracy and F1 scores evident in figures 9, 10 and 11.

The derived spectral reflectance curves clearly distinguish between water and other land cover types in SWIR1 (1566 nm) and SWIR2 (2107 nm). Water exhibits minimal reflectance in these regions, allowing for effective separation from other classes. This finding aligns with established water detection methods utilising shortwave infrared bands (Ma *et al*., 2019).

The analysis revealed fluctuations in the area coverage of surface water, vegetation, bare area, and salt hardpan across the study period. Water was most frequently found in the central and northeastern regions, with an average coverage of approximately 33% and a range of 19% (2020) to 56% (2011, 2014). Years with extensive water coverage of >50% coincided with 2004, 2008, 2010, 2011, 2014, 2017, and 2018. Vegetation cover displayed significant variability, with a maximum area of 1405 km² in 1995 and a minimum of 119 km² in 2005. Bare area also exhibited fluctuations, reaching a peak in 2020 with an area of 1214 km² and a minimum in 2004 with an area of 269 km². Similarly, salt hardpan coverage varied, with a maximum area of 1322 km² in 1998 and a minimum of 454 km² in 2017. The spatiotemporal trend analysis indicated a positive trend for surface water and bare area, suggesting an increase in their extent over time. Conversely, vegetation and salt hardpan exhibited negative trends, suggesting decreased coverage. Bryant *et al*. (2007) reveal a notable decrease in vegetation in Sua Pan.

### 5.2. Surface Water Detection, Interpretation and Mapping

The study compared the spectral reflectance of (NDSI, MNDWI, and SWI). All three indices exhibited similar responses in the blue, green, and red regions for surface water. However, they diverged in the NIR and SWIR regions. MNDWI and NDSI are commonly used indices with lower reflectance values in NIR and close to zero reflectance in SWIR-1 and SWIR-2, indicating their ability to distinguish water from other land cover types. The newly proposed index SWI showed higher reflectance values in the NIR and SWIR regions than in MNDWI and NDSI. This suggests its ability to capture open and shallow water within the pan. This notion is strongly supported by Bryant (1996), who found that the visible and NIR region of the electromagnetic spectrum is influenced by the highly reflective properties of salt minerals present in salt pans.

The visual interpretation of the indices further highlights their performance. According to Riedel *et al*. (2012), the northeastern part of Sua Pan is fed by the Nata River; therefore, surface

water was detected in the northeastern region by MNDWI, NDSI and SWI. While MNDWI and NDSI detected water in specific areas, particularly the northeastern part, they missed surface water in the centre. In contrast, the SWI successfully identified surface water in both the northeastern and central regions of Sua Pan.

Fisher *et al*. (2016) note that Landsat data was used to analyse the spectral reflectance properties of several water body types. Their findings revealed that different water types exhibit unique spectral signatures. Clear and deep water bodies demonstrated a general trend of decreasing reflectance across the spectrum. In contrast, water containing significant plant matter (appearing dark or green) showed higher reflectance in the green band. Similarly, brown or dark brown water with high sediment concentrations exhibited peaks in the red band (Fisher *et al*., 2016). This highlights a crucial point: the effectiveness of multiband methods for water extraction can vary depending on the specific water type being studied.

Furthermore, the study found that each multiband method produced distinct errors for different water and non-water land cover types. However, all methods achieved accurate classification for pure water pixels. This suggests that factors like the background colour (riverbed sediment or vegetation) and the chosen classification technique can influence the overall accuracy of water extraction.

Similarly, Bryant (1996) and Sadrian *et al*. (2023) demonstrate that NIR and SWIR1-2 bands have a higher spectral reflectance due to dust and muddy water conditions than MNDWI and NDSI. This might explain why SWI has a higher overall accuracy than MNDWI and NDSI. The accuracy assessment using a confusion matrix and McNemar's chi-square test revealed significant limitations in MNDWI and NDSI performance. They achieved overall accuracies below 65% and showed statistically significant differences compared to the validation data.

The newly proposed SWI demonstrated a substantial improvement. It achieved an overall accuracy of 94% and Kappa coefficient (0.87), indicating strong agreement with the reference data. McNemar's chi-square test also showed no significant statistical difference between the SWI classification and the validation dataset. This suggests the SWI's effectiveness in accurately mapping surface water in Sua Pan, potentially due to its ability to account for the presence of saline water. Previous studies agree that developing indices according to the environment have a higher overall accuracy than commonly used water indices (Sharma *et al*., 2015; Jiang *et al*., 2020).

### 5.3. Spatiotemporal Dynamics of Surface Water in Sua Pan

The visual interpretation of SWI-derived maps (Figure 18) reveals significant fluctuations in surface water area across the study period. The wet season (January-March) consistently exhibited a larger water extent than the dry season (August-October). This aligns with expected seasonal precipitation patterns and river inflow where Sua Pan undergoes seasonal flooding and drying (Eckardt *et al*., 2008; Burrough, 2022; Ringrose *et al*., 2023).

The average surface water area for the wet season (1404.76 km²) was more than double that of the dry season (447.21 km²). Notably, 2017 displayed the most extensive water coverage for both seasons (2644.59 km² for wet and 1549.79 km² for dry). Conversely, 1996 and 2005 witnessed the least surface water presence, particularly during the wet season (190.69 km²).

The northeastern part of Sua Pan has unique geographical and subsurface characteristics that affect its water retention capabilities (Burrough and Thomas, 2008). Additionally, this area is sensitive to rainfall variability, with episodic rainfall events that don't consistently fill the pan, especially during drier years (McCarthy and Ellery, 1998). In 1992, 1995 and 2003, the rainfall during the wet season was less than 200 mm, contributing to reduced water accumulation.

The trend analysis suggests a statistically significant, weak positive trend for the wet season surface water area (*p-value* = 0.01). This indicates a gradual increase in water extent over the past three decades. On the contrary, the dry season trend showed a very weak positive trend but lacked statistical significance (*p-value* = 0.734). The CV highlights the variability in surface water area. The wet season exhibited a moderate CV (29.17%), suggesting somewhat consistent water availability compared to the dry season (CV of 91.24%), which displayed higher variability.

The homogeneity tests on the wet season data revealed a significant change point in the surface water area series. The SNHT and Buishand tests identified potential shifts in 1994 and 2003, respectively (Table 7). This suggests potential factors like extreme weather events or long-term climate shifts might have influenced the surface water dynamics during these periods. In contrast, the dry season data showed homogeneity for all three tests (Pettitt, SNHT, Buishand). This implies a statistically consistent dry season water extent pattern throughout the study period.

### 5.4. ENSO, Climate Variables, and Surface Water Dynamics in Sua Pan

The analysis revealed a surprisingly weak to moderate relationship between ENSO, rainfall, and surface water area across both seasons. Statistical tests (ANOVA and Tukey's HSD) showed no significant differences in rainfall or surface water area associated with specific ENSO phases. While previous studies suggest ENSO's influence on regional precipitation patterns in southern Africa (Lakhraj-Govender and Grab, 2019), the results indicate that factors beyond large-scale oceanic oscillations might drive Sua Pan's water balance. Hitchcock *et al*. (2000) suggest that the increase in groundwater pumping for irrigation has led to a decline in water level within the Makgadikgadi Pans complex. A Driver and Reason (2017) study suggests that ENSO events may modulate the Botswana High, which is expected to suppress rainfall during El Niño and enhance rainfall during La Niña.

Furthermore, the study highlights strong positive correlations between surface water area, evapotranspiration, and LST during wet and dry seasons. This suggests a dynamic interplay between these variables. Increased evapotranspiration during warmer periods leads to a decrease in surface water. Conversely, cooler periods witness reduced evapotranspiration, allowing surface water to accumulate. LST serves as a proxy for evaporative processes. A strong negative correlation between LST and surface water area reinforces the influence of evapotranspiration.

Interestingly, the correlation between rainfall and surface water area was stronger during the wet season (strong positive) compared to the dry season (moderate positive). This suggests that while rainfall significantly contributes to replenishing surface water during the wet season, other factors might play a more prominent role in the dry season when rainfall is scarce. Franchi *et al*. (2020) note that in the Makgadikgadi Basin, the decline in rainfall and increase in temperature has led to the shrinkage of salt pans.

### 5.5. Research Limitations

Understanding ecosystems requires continuous monitoring of surface water, LULC and meteorological change analysis. However, the limited availability of monthly satellite images, specifically Landsat TM and ETM+ data from 1992 to 2012, was insufficient for intra-annual analysis. This gap hindered our ability to fully capture the dynamic changes occurring within a year and how they vary interannually. This limitation is particularly critical for Sua Pan, which is located in a semi-arid region. Here, both temperature and water pumping for mining activities significantly impact surface water, causing it to dry within days.

An additional challenge in arid regions is spectral similarity. Here, the spectral signatures of bare soil and sparse vegetation can be very similar. This similarity can make it difficult for machine learning algorithms to achieve high classification accuracy for all classes.

Furthermore, the proposed water index (SWI) was only tested using Landsat 9 OLI imagery for 2022. Additionally, it was compared to just two other indices (MNDWI and NDSI) and applied solely to Sua Pan. Consequently, the efficiency of SWI in other regions, with different satellites, or against a broader range of indices remains uncertain.

### 5.6 Research Recommendations

Future research can explore techniques to address these limitations. Therefore, this study recommends the application of the Saline Water Index in other salt pans. The applicability of water indices can be highly dependent on the environmental context. Future research efforts should prioritise the development of advanced indices specifically tailored to address the unique challenges of water body differentiation in various environments. This could involve exploring indices optimised for specific water types (e.g., saline vs. freshwater) or complex land cover compositions. It is recommended that future studies integrate climate data and anthropogenic influence data with remotely sensed data to effectively assess its influence on environmental resources. Lastly, research on applying remote sensing techniques with the integration of machine learning needs to be conducted in sub-Saharan Africa for water resource management.

## Chapter 6: Conclusion

This study employed GEE to analyse remote sensing data, investigating the spatiotemporal dynamics of surface water extent and LULC changes within Sua Pan, Botswana, from 1992 to 2022. The primary objective was to map and monitor surface water variations across the pan.

It can be concluded that:

- GEE's cloud-computing capabilities facilitated the efficient processing of Landsat imagery across a vast timeframe. The Random Forest (RF) classifier achieved moderate to substantial accuracy (65.2% - 85.09%) in distinguishing water, bare area, vegetation, and salt hardpan. Notably, accuracy improved with later Landsat satellites, potentially due to additional spectral bands.
- Established water indices (MNDWI, NDSI) performed moderately well, but the newly developed SWI specifically designed for Sua Pan's saline environment achieved the highest overall accuracy (94%) in detecting surface water.
- Surface water exhibited significant interannual variability, with peak extents observed in 2004, 2008, 2010, 2011, 2014, 2017, and 2018. Conversely, vegetation and salt hardpan coverage decreased while bare area coverage increased. However, limitations exist in interpreting these trends due to the influence of unaccounted interannual climatic variability.
- This study revealed distinct seasonal patterns in water availability within the study area. Surface water extent, rainfall, and evapotranspiration all exhibited higher values during the wet seasons compared to the dry seasons. Additionally, temperatures were generally higher during the dry season. Increased evapotranspiration significantly impacted surface water presence.

This study demonstrates the significant potential of remote sensing to map and monitor surface water extent within salt pan environments. The findings also provide insight to inform policy decisions regarding environmental management and conservation. This study highlights the urgent need to shift towards cost and time-effective techniques to assess surface water changes, especially in under-resourced regions. This information can contribute to policy decisions and sustainability strategies that make Sua Pan a more sustainable environment, particularly anthropogenic activities and climate variability.

**References**


Abbas, A. and Khan, S. 2007. Using remote sensing techniques for appraisal of irrigated soil salinity. In *International Congress on Modelling and Simulation (MODSIM)* Modelling and Simulation Society of Australia and New Zealand. pp. 2632-2638.

Acharya, T.D., Lee, D.H., Yang, I.T. and Lee, J.K. 2016. Identification of water bodies in a Landsat 8 OLI image using a J48 decision tree. *Sensors*, *16*(7), pp.1075.

Adam, E., Mutanga, O., Odindi, J. and Abdel-Rahman, E.M. 2014. Land-use/cover classification in a heterogeneous coastal landscape using RapidEye imagery: evaluating the performance of random forest and support vector machines classifiers. *International Journal of Remote Sensing*, *35*(10), pp.3440-3458.

Ahmed, K., Shahid, S., Ismail, T., Nawaz, N. and Wang, X.J. 2018. Absolute homogeneity assessment of precipitation time series in an arid region of Pakistan. *Atmósfera*, *31*(3), pp.301-316.

Akinyemi, F.O., Ikanyeng, M. and Muro, J. 2019. Land cover change effects on land surface temperature trends in an African urbanizing dryland region. *City and Environment Interactions*, *4*, pp.100029.

Akoglu, H., 2018. User's guide to correlation coefficients. *Turkish Journal of Emergency Medicine*, *18*(3), pp.91-93.

Albarqouni, M.M., Yagmur, N., Bektas Balcik, F. and Sekertekin, A. 2022. Assessment of spatio-temporal changes in water surface extents and lake surface temperatures using Google Earth Engine for lakes region, Türkiye. *ISPRS International Journal of Geo-Information*, *11*(7), pp.407.

Alesheikh, A.A., Ghorbanali, A. and Nouri, N. 2007. Coastline change detection using remote sensing. *International Journal of Environmental Science & Technology*, *4*, pp.61-66.

Alexandersson, H. 1986. A homogeneity test applied to precipitation data. *Journal of Climatology*, *6*(6), pp.661-675.

Alsdorf, D.E., Rodríguez, E. and Lettenmaier, D.P. 2007. Measuring surface water from space. *Reviews of Geophysics*, *45*(2), pp.1-24.

Amoako-Attah, B., Henyo, I.K. and Amoako-Mensah, T. 2023. Application of GIS and Remote Sensing to Identify Changes in Surface Water Bodies and Wetland Depletion in the Kumasi Metropolis, Ghana. *Preprints* 2023, 2023040159. https://doi.org/10.20944/preprints202304.0159.v1

Ao, Y., Li, H., Zhu, L., Ali, S. and Yang, Z. 2019. The linear random forest algorithm and its advantages in machine learning assisted logging regression modeling. *Journal of Petroleum Science and Engineering*, *174*, pp.776-789.

Avcı, C., Budak, M., Yağmur, N. and Balcik, F. 2021. Comparison Between Random Forest and Support Vector Machine Algorithms for LULC Classification. *International Journal of Engineering and Geosciences*. 8. 10.26833/ijeg.987605.

Banerjee, C. and Kumar, D.N. 2019. Integration of GRACE Data for Improvement of Hydrological Models. *Hydrology in a Changing World: Challenges in Modeling*, pp.1-22.

Bangira, T., Alfieri, S.M., Menenti, M. and Van Niekerk, A. 2019. Comparing thresholding with machine learning classifiers for mapping complex water. *Remote Sensing*, *11*(11), pp.1351.

Bastin, J.F., Finegold, Y., Garcia, C., Mollicone, D., Rezende, M., Routh, D., Zohner, C.M. and Crowther, T.W. 2019. The global tree restoration potential. *Science*, *365*(6448), pp.76-79.

Batisani, N. and Yarnal, B. 2010. Rainfall variability and trends in semi-arid Botswana: implications for climate change adaptation policy. *Applied Geography*, *30*(4), pp.483-489.

Bhaga, T.D., Dube, T., Shekede, M.D. and Shoko, C. 2020. Impacts of climate variability and drought on surface water resources in Sub-Saharan Africa using remote sensing: A review. *Remote Sensing*, *12*(24), pp.4184.

Blamey, R.C., Kolusu, S.R., Mahlalela, P., Todd, M.C. and Reason, C.J.C. 2018. The role of regional circulation features in regulating El Niño climate impacts over southern Africa: A comparison of the 2015/2016 drought with previous events. *International Journal of Climatology*, *38*(11), pp.4276-4295.

Bowen, B.B., Kipnis, E.L. and Raming, L.W. 2017. Temporal dynamics of flooding, evaporation, and desiccation cycles and observations of salt crust area change at the Bonneville Salt Flats, Utah. *Geomorphology*, *299*, pp.1-11.

Bryant, R.G. 1996. Validated linear mixture modelling of Landsat TM data for mapping evaporite minerals on a playa surface: methods and applications. *International Journal of Remote Sensing*, *17*(2), pp.315-330.

Bryant, R.G., Bigg, G.R., Mahowald, N.M., Eckardt, F.D. and Ross, S.G. 2007. Dust emission response to climate in southern Africa. *Journal of Geophysical Research: Atmospheres*, *112*(D9), pp.1-17

Burrough, S.L. 2022. The Makgadikgadi basin. In *Landscapes and Landforms of Botswana* (pp. 77-90). Cham: Springer International Publishing.

Castañeda, C., Herrero, J. and Casterad, M.A. 2005. Facies identification within the playa-lakes of the Monegros desert, Spain, from field and satellite data. *Catena*, *63*(1), pp.39-63.

Chabalala, Y., Adam, E. and Ali, K.A., 2022. Machine learning classification of fused Sentinel-1 and Sentinel-2 image data towards mapping fruit plantations in highly heterogenous landscapes. *Remote Sensing*, *14*(11), p.2621.

Chapman, J.E., Rothery, D.A., Francis, P.W. and Pontual, A. 1989. Remote sensing of evaporite mineral zonation in salt flats (salars). *Remote Sensing*, *10*(1), pp.245-255.

Cohen, J. 1960. A coefficient of agreement for nominal scales. *Educational and Psychological Measurement, 20,* 37–46. https://doi.org/10.1177/001316446002000104

Cohen, J., Cohen, P., West, S.G. and Aiken, L.S. 2013. *Applied Multiple Regression/Correlation Analysis for the Behavioral Sciences*. Routledge.

Collen, B., Whitton, F., Dyer, E.E., Baillie, J.E., Cumberlidge, N., Darwall, W.R., Pollock, C., Richman, N.I., Soulsby, A.M. and Böhm, M. 2014. Global patterns of freshwater species diversity, threat and endemism. *Global Ecology and Biogeography*, *23*(1), pp.40-51.

de Almeida, C.R., Alírio, J., Gonçalves, A. and Teodoro, A.C. 2023, October. Analysis of the urban heat island in Bragança, Portugal, using MODIS data (2003-2022). In *Earth Resources and Environmental Remote Sensing/GIS Applications XIV* (Vol. 12734, pp. 125-137). SPIE.

De Klerk, A.R., De Klerk, L.P., Oberholster, P.J., Ashton, P.J., Dini, J.A. and Holness, S.D. 2016. A review of depressional wetlands (pans) in South Africa, including a water quality classification system. *Water Research Commission Report No 2230/1/16, Gezina*.

Dehni, A. and Lounis, M. 2012. Remote sensing techniques for salt affected soil mapping: application to the Oran region of Algeria. *Procedia Engineering*, *33*, pp.188-198.

Department of Environmental Affairs and Centre for Applied Research. 2010. The Makgadikgadi Framework Management Plan. Government of Botswana, Gaborone.

Driver, P., Abiodun, B. and Reason, C.J.C. 2019. Modelling the precipitation response over southern Africa to the 2009–2010 El Niño using a stretched grid global atmospheric model. *Climate dynamics*, *52*, pp.3929-3949.

Driver, P. and Reason, C.J.C. 2017. Variability in the Botswana High and its relationships with rainfall and temperature characteristics over southern Africa. *International Journal of Climatology*, *37*, pp.570-581.

Drusch, M., Del Bello, U., Carlier, S., Colin, O., Fernandez, V., Gascon, F., Hoersch, B., Isola, C., Laberinti, P., Martimort, P. and Meygret, A. 2012. Sentinel-2: ESA's optical high-resolution mission for GMES operational services. *Remote sensing of Environment*, *120*, pp.25-36.

Dube, T., Pandit, S., Shoko, C., Ramoelo, A., Mazvimavi, D. and Dalu, T. 2019. Numerical assessments of leaf area index in tropical savanna rangelands, South Africa using Landsat 8 OLI derived metrics and in-situ measurements. *Remote Sensing*, *11*(7), p.829.

Eckardt, F. D., Bryant, R.G., McCulloch, G., Spiro, B. and Warren W. Wood, W.W. 2008. The Hydrochemistry of a Semi-Arid Pan Basin Case Study: Sua Pan, Makgadikgadi, Botswana. *Applied Geochemistry 23* (6): 1563–1580. https://doi.org/10.1016/j.apgeochem.2007.12.033.

Fashae O.A., Olusola, A.O., Obateru, R.O. and Adagbasa, E.G. 2020. Land use/land cover change and land surface temperature of Ibadan and environs, Nigeria. *Environmental Monitoring Assessment,* 192: 109.

Feher, L.C., Osland, M.J., Griffith, K.T., Grace, J.B., Howard, R.J., Stagg, C.L., Enwright, N.M., Krauss, K.W., Gabler, C.A., Day, R.H. and Rogers, K. 2017. Linear and nonlinear effects of temperature and precipitation on ecosystem properties in tidal saline wetlands. *Ecosphere*, *8*(10), p.e01956.

Feyisa, G. L., Meilby, H., Fensholt, R. and Proud, S.R. 2014. Automated water extraction index

(AWEI): A new technique for surface water mapping using Landsat imagery. *Remote Sensing of Environment, 140*: 23-35.

Fisher, A., Flood, N. and Danaher, T. 2016. Comparing Landsat water index methods for automated water classification in eastern Australia. *Remote Sensing of Environment*, *175*, pp.167-182.

Flahaut, J., Martinot, M., Bishop, J.L., Davies, G.R. and Potts, N.J. 2017. Remote sensing and in situ mineralogic survey of the Chilean salars: An analog to Mars evaporate deposits?. *Icarus*, *282*, pp.152-173.

Foga, S., Scaramuzza, P.L., Guo, S., Zhu, Z., Dilley Jr, R.D., Beckmann, T., Schmidt, G.L., Dwyer, J.L., Hughes, M.J. and Laue, B. 2017. Cloud detection algorithm comparison and validation for operational Landsat data products. *Remote Sensing of Environment*, *194*, pp.379-390.

Franchi, F., MacKay, R., Selepeng, A.T. and Barbieri, R. 2020. Layered mound, inverted channels and polygonal fractures from the Makgadikgadi pan (Botswana): Possible analogues for Martian aqueous morphologies. *Planetary and Space Science*, *192*, p.105048.

Frazier, P. S and Page, K.J. 2000. Water Body Detection and Delineation with Landsat TM Data. *Photogrammetric engineering and remote sensing, 66*(12), pp.1461-1468.

Friederich, H. and Gould, J. 1986. Drinking water for Nata an alternative strategy. *Botswana Notes & Records*, *18*(1), pp.107-113.

Fuentes, I., F. van Ogtrop, and R. W. Vervoort. 2020. Long-Term Surface Water Trends and Relationship with Open Water Evaporation Losses in the Namoi Catchment, Australia. *Journal of Hydrology 584*: 124714–124777. doi:10.1016/j.jhydrol.2020.124714.

Geris, J., Comte, J.C., Franchi, F., Petros, A.K., Tirivarombo, S., Selepeng, A.T. and Villholth, K.G. 2022. Surface water-groundwater interactions and local land use control water quality impacts of extreme rainfall and flooding in a vulnerable semi-arid region of Sub-Saharan Africa. *Journal of Hydrology*, *609*, p.127834.

Gidey, E. and Mhangara, P. 2023. An Application of Machine-Learning Model for Analyzing the Impact of Land-Use Change on Surface Water Resources in Gauteng Province, South Africa. *Remote Sensing*, *15*(16), p.4092.

Gislason, P.O., Benediktsson, J.A. and Sveinsson, J.R. 2006. Random forests for land cover classification. *Pattern recognition letters*, *27*(4), pp.294-300.

Gocic, M. and Trajkovic, S. 2013. Analysis of changes in meteorological variables using Mann-Kendall and Sen's slope estimator statistical tests in Serbia. *Global and Planetary Change*, *100*, pp.172-182.

Guo, Q., Pu, R., Li, J. and Cheng, J. 2017. A weighted normalized difference water index for water extraction using Landsat imagery. *International Journal of Remote Sensing*, *38*(19), pp.5430-5445.

Gxokwe, S., Dube, T., Mazvimavi, D. and Grenfell, M. 2022. Using cloud computing

techniques to monitor long-term variations in ecohydrological dynamics of small seasonally-flooded wetlands in semi-arid South Africa. *Journal of Hydrology*, *612*, p.128080.

Haferburg, G., Gröning, J.A., Schmidt, N., Kummer, N.A., Erquicia, J.C. and Schlömann, M. 2017. Microbial diversity of the hypersaline and lithium-rich Salar de Uyuni, Bolivia. *Microbiological Research*, *199*, pp.19-28.

Hall, D.K., Kimball, J.S., Larson, R., DiGirolamo, N.E., Casey, K.A. and Hulley, G. 2023. Intensified warming and aridity accelerate terminal lake desiccation in the Great Basin of the western United States. *Earth and Space Science*, *10*(1), p.e2022EA002630.

Hitchcock, Robert K. and Nangati, F. 2000. People of the two-way river: Socio-economic change and natural resource management in the Nata River region. *Botswana Notes & Records*, *32*(1), pp.85-106. https://doi.org/10.1016/j.asej.2022.101739.

Huang, C., Chen, Y., Zhang, S. and Wu, J. 2018. Detecting, extracting, and monitoring surface water from space using optical sensors: A review. *Reviews of Geophysics*, *56*(2), pp.333-360.

Immitzer, M., F. Vuolo, and C. Atzberger. 2016. First Experience with Sentinel-2 Data for Crop and Tree Species Classifications in Central Europe. *Remote Sensing* 8 (3): 166. doi:10.3390/rs8030166. ISSN 2090-4479,

Jamaluddin, I., Chen, Y.N., Ridha, S.M., Mahyatar, P. and Ayudyanti, A.G. 2022. Two Decades Mangroves Loss Monitoring Using Random Forest and Landsat Data in East Luwu, Indonesia (2000–2020). *Geomatics*, *2*(3), pp.282-296.

Javan, K., Azizzadeh, M.R. and Yousefi, S. 2016. An Investigation and assessment of meteorological drought in Lake Urmia Basin using drought indices and probabilistic methods. *Natural Environment Change*, *2*(2), pp.153-164.

Javari, M. 2016. Trend and homogeneity analysis of precipitation in Iran. *Climate*, *4*(3), p.44.

Jiang, H., Feng, M., Zhu, Y., Lu, N., Huang, J. and Xiao, T. 2014. An automated method for extracting rivers and lakes from Landsat imagery. *Remote Sensing*, *6*(6), pp.5067-5089.

Jiang, W., Ni, Y., Pang, Z., He, G., Fu, J., Lu, J., Yang, K., Long, T. and Lei, T. 2020. A new index for identifying water body from Sentinel-2 satellite remote sensing imagery. *ISPRS Annals of the Photogrammetry, Remote Sensing and Spatial Information Sciences*, *3*, pp.33-38.

Kazemi Garajeh, M., Salmani, B., Zare Naghadehi, S., Valipoori Goodarzi, H. and Khasraei, A. 2023. An integrated approach of remote sensing and geospatial analysis for modeling and predicting the impacts of climate change on food security. *Scientific Reports*, *13*(1), p.1057.

Kendall, M.G. 1975. Rank correlation methods. London: Charles Griffin

Khan, N.M., Rastoskuev, V.V., Sato, Y. and Shiozawa, S. 2005. Assessment of hydrosaline land degradation by using a simple approach of remote sensing indicators. *Agricultural Water Management*, *77*(1-3), pp.96-109.

Klein, I., Gessner, U., Dietz, A.J. and Kuenzer, C. 2017. Global WaterPack–A 250 m resolution

dataset revealing the daily dynamics of global inland water bodies. *Remote Sensing of Environment*, *198*, pp.345-362.

Klemas, V. and Pieterse, A. 2015. Using remote sensing to map and monitor water resources in arid and semiarid regions. *Advances in Watershed Science and Assessment*, pp.33-60.

Kløve, B., Ala-Aho, P., Bertrand, G., Gurdak, J.J., Kupfersberger, H., Kværner, J., Muotka, T., Mykrä, H., Preda, E., Rossi, P. and Uvo, C.B. 2014. Climate change impacts on groundwater and dependent ecosystems. *Journal of Hydrology*, *518*, pp.250-266.

Kohen, J. 1960. A coefficient of agreement for nominal scale. *Educational and Psychological Measurement* 20:37–46. doi:10.1177/001316446002000104

Kousky, V.E. and Higgins, R.W. 2007. An alert classification system for monitoring and assessing the ENSO cycle. *Weather and Forecasting*, *22*(2), pp.353-371.

Lakhraj-Govender, R. and Grab, S.W. 2019. Assessing the impact of El Niño–Southern Oscillation on South African temperatures during austral summer. *International Journal of Climatology*, *39*(1), pp.143-156.

Li W, Du Z, Ling F, Zhou D, Wang H, Gui Y, Sun B & Zhang X. 2013. A comparison of land surface water mapping using the normalized difference water index from TM, ETM+ and ALI. *Remote Sensing* 5: 5530-5549.

Li, Jiaxin, Ronghua Ma, Zhigang Cao, Kun Xue, Junfeng Xiong, Minqi Hu, and Xuejiao Feng. 2022. Satellite Detection of Surface Water Extent: A Review of Methodology. *Water 14*, no. 7: 1148. https://doi.org/10.3390/w14071148

Lillesand, T., Kiefer, R.W. and Chipman, J. 2015. *Remote Sensing and Image Interpretation*. John Wiley & Sons.

Liu, C., Li, W., Zhu, G., Zhou, H., Yan, H. and Xue, P. 2020. Land use/land cover changes and their driving factors in the Northeastern Tibetan Plateau based on Geographical Detectors and Google Earth Engine: A case study in Gannan Prefecture. *Remote Sensing*, *12*(19), p.3139.

Ma, S., Zhou, Y., Gowda, P.H., Dong, J., Zhang, G., Kakani, V.G., Wagle, P., Chen, L., Flynn, K.C. and Jiang, W. 2019. Application of the water-related spectral reflectance indices: A review. *Ecological Indicators*, *98*, pp.68-79.

Mahdianpari, M., Salehi, B., Mohammadimanesh, F. and Motagh, M. 2017. Random forest wetland classification using ALOS-2 L-band, RADARSAT-2 C-band, and TerraSAR-X imagery. *ISPRS Journal of Photogrammetry and Remote Sensing*, *130*, pp.13-31.

Malahlela, O.E., Oliphant, T., Tsoeleng, L.T. and Mhangara, P. 2018. Mapping chlorophyll-a concentrations in a cyanobacteria-and algae-impacted Vaal Dam using Landsat 8 OLI data. *South African Journal of Science*, *114*(9-10), pp.1-9.

Mann, H.B. 1945. Nonparametric tests against trend. Econometric, 13(3), 245-259.

McCulloch, G.P., Hancock, P., Bridges, B. 2007. Makgadikgadi Pans Important Bird Area Monitoring Report, 2007. *Birdlife Botswana*, Gaborone, Botswana

McCulloch, G.P. and Borello, W. 2000. The Importance of the Makgadikgadi Salt Pans in Botswana for Flamingos in Africa. *Waterbirds: The International Journal of Waterbird Biology* 23: 64–68. https://doi.org/10.2307/1522148.

McCulloch, G.P. and Irvine, K. 2004. Breeding of Greater and Lesser Flamingos at Sua Pan, Botswana, 1998–2001. *Ostrich* 75 (4): 236–42. https://doi.org/10.2989/00306520409485450.

McFeeters, S.K. 1996. The use of the Normalized Difference Water Index (NDWI) in the delineation of open water features. *International Journal of Remote Sensing*, *17*(7), pp.1425-1432.

McLeod, G. 2019. *Makgadikgadi Pans*. Penguin Random House South Africa.

Micklin, P. 2010. The past, present, and future Aral Sea. *Lakes & Reservoirs: Research & Management*, *15*(3), pp.193-213.

Milewski, R., Chabrillat, S. and Behling, R. 2017. Analyses of recent sediment surface dynamic of a Namibian Kalahari salt pan based on multitemporal landsat and hyperspectral hyperion data. *Remote Sensing*, *9*(2), p.170.

Milewski, R., Chabrillat, S. and Bookhagen, B. 2020. Analyses of Namibian seasonal salt pan crust dynamics and climatic drivers using Landsat 8 time-series and ground data. *Remote Sensing*, *12*(3), p.474.

Mim, M.A. and Zamil, K.S. 2018. Gis-based analysis of changing surface water in rajshahi city corporation area using support vector machine (svm), decision tree & random forest technique. *Machine Learning Research*, *3*(2), pp.11-17.

Mirzakarimova, G.M. 2023. Remote sensing data: international experiences and applications. *ITALY" ACTUAL PROBLEMS OF SCIENCE AND EDUCATION IN THE FACE OF MODERN CHALLENGES"*., *14*(1), pp.1-6.

Mishra, V.N., Prasad, R., Rai, P.K., Vishwakarma, A.K. and Arora, A. 2019. Performance evaluation of textural features in improving land use/land cover classification accuracy of heterogeneous landscape using multi-sensor remote sensing data. *Earth Science Informatics*, *12*, pp.71-86.

Mohsen, A., Elshemy, M. and Zeidan, B.A. 2018. Change Detection for Lake Burullus, Egypt Using Remote Sensing and GIS Approaches. *Environmental Science and Pollution Research*. https://doi.org/10.1007/s11356-016-8167-y.

Moradi, M., Sahebi, M. and Shokri, M. 2017. Modified optimization water index (MOWI) for Landsat-8 OLI/TIRS. *The International Archives of the Photogrammetry, Remote Sensing and Spatial Information Sciences*, *42*, pp.185-190.

Nasiri, V., Deljouei, A., Moradi, F., Sadeghi, S.M.M. and Borz, S.A. 2022. Land use and land cover mapping using Sentinel-2, Landsat-8 Satellite Images, and Google Earth Engine: A comparison of two composition methods. *Remote Sensing*, *14*(9), p.1977.

Newete, S.W., Mayonde, S., Kekana, T. and Adam, E. 2023. A rapid and accurate method of mapping invasive Tamarix genotypes using Sentinel-2 images. *PeerJ*, *11*, p.e15027.

Nhamo, L., Magidi, J. and Dickens, C. 2017. Determining wetland spatial extent and seasonal variations of the inundated area using multispectral remote sensing. *Water Sa*, *43*(4), pp.543-552.

Nield, J.M., Wiggs, G.F., King, J., Bryant, R.G., Eckardt, F.D., Thomas, D.S. and Washington, R. 2016. Climate–surface–pore-water interactions on a salt crusted playa: implications for crust pattern and surface roughness development measured using terrestrial laser scanning. *Earth Surface Processes and Landforms*, *41*(6), pp.738-753.

Obilor, E.I. and Amadi, E.C. 2018. Test for significance of Pearson's correlation coefficient. *International Journal of Innovative Mathematics, Statistics & Energy Policies*, *6*(1), pp.11-23.

Ocampo-Marulanda, C., Fernández-Álvarez, C., Cerón, W.L., Canchala, T., Carvajal-Escobar, Y. and Alfonso-Morales, W. 2022. A spatiotemporal assessment of the high-resolution CHIRPS rainfall dataset in southwestern Colombia using combined principal component analysis. *Ain Shams Engineering Journal*, *13*(5), p.101739.

Olmanson, L.G., Brezonik, P.L., Finlay, J.C. and Bauer, M.E. 2016. Comparison of Landsat 8 and Landsat 7 for regional measurements of CDOM and water clarity in lakes. *Remote Sensing of Environment*, *185*, pp.119-128.

Ozesmi, S.L. and Bauer, M.E. 2002. Satellite remote sensing of wetlands. *Wetlands Ecology and Management*, *10*, pp.381-402.

Patel, A.K., Trujillo-Rivera, E., Chamberlain, J.M., Morizono, H. and Pollack, M.M. 2024. External evaluation of the Dynamic Criticality Index: A machine learning model to predict future need for ICU care in hospitalized pediatric patients. *Plos one*, *19*(1), p.e0288233.

Pekel, J.F., Cottam, A., Gorelick, N. and Belward, A.S. 2016. High-resolution mapping of global surface water and its long-term changes. *Nature*, *540*(7633), pp.418-422.Pettitt (1979)

Policelli, F., Hubbard, A., Jung, H.C., Zaitchik, B. and Ichoku, C. 2019. A predictive model for Lake Chad total surface water area using remotely sensed and modeled hydrological and meteorological parameters and multivariate regression analysis. *Journal of Hydrology*, *568*, pp.1071-1080.

Rahman, M.S. and Di, L. 2017. The state of the art of spaceborne remote sensing in flood management. *Natural Hazards*, *85*, pp.1223-1248.

Raw, J.L., Adams, J.B., Bornman, T.G., Riddin, T. and Vanderklift, M.A. 2021. Vulnerability to sea-level rise and the potential for restoration to enhance blue carbon storage in salt marshes of an urban estuary. *Estuarine, Coastal and Shelf Science*, *260*, p.107495.

Riedel, F., Erhardt, S., Chauke, C., Kossler, A., Shemang, E. and Tarasov, P. 2012. Evidence for a permanent lake in Sua Pan (Kalahari, Botswana) during the early centuries of the last millennium indicated by distribution of Baobab trees (Adansonia digitata) on "Kubu Island". *Quaternary International*, *253*, pp.67-73.

Ringrose, S., Cassidy, L., Diskin, S. and Coetzee, S.H. 2023. Factors leading to sub-surface

pan silcrete formation in north-central Botswana. *South African Journal of Geology 2023*, *126*(1), pp.93-112.

Rivera, J.A., Hinrichs, S. and Marianetti, G. 2019. Using CHIRPS dataset to assess wet and dry conditions along the semiarid central-western Argentina. *Advances in Meteorology*, *2019*, pp.1-18.

Rokni, K., Ahmad, A., Selamat, A. and Hazini, S. 2014. Water feature extraction and change detection using multitemporal Landsat imagery. *Remote Sensing*, *6*(5), pp.4173-4189.

Rwanga, S.S. and Ndambuki, J.M. 2017. Accuracy assessment of land use/land cover classification using remote sensing and GIS. *International Journal of Geosciences*, *8*(04), p.611.

Sadrian, M.R., Calvin, W.M., Engelbrecht, J.P. and Moosmüller, H. 2023. Spectral characterization of parent soils from globally important dust aerosol entrainment regions. *Journal of Geophysical Research: Atmospheres*, *128*(2), p.e2022JD037666.

Sanchez-Lopez, M.D. 2019. From a white desert to the largest world deposit of lithium: Symbolic meanings and materialities of the Uyuni Salt Flat in Bolivia. *Antipode*, *51*(4), pp.1318-1339.

Scheffers, A.M. and Kelletat, D.H. 2016. *Lakes of the world with google earth: understanding our environment*. Switzerland: Springer International Publishing.

Schmidt, G., Luzzi, E., Franchi, F., Selepeng, A.T., Hlabano, K. and Salvini, F. 2023. Structural influences on groundwater circulation in the Makgadikgadi salt pans of Botswana? Implications for martian playa environments. *Frontiers in Astronomy and Space Sciences*, *10*, p.1108386.

Seaman, M.T., Ashton, P.J. and Williams, W.D. 1991. Inland salt waters of southern Africa. *Hydrobiologia*, *210*, pp.75-91.

Segobaetso, T.K., Tafesse, N.T., Mapeo, R.B.M. and Laletsang, K. 2022. Groundwater recharge using the chloride mass balance method in the Kanye area, in southeast Botswana. *Journal of African Earth Sciences*, *193*, p.104534.

Setlhogile, T., Arntzen, J., Mabiza, C. and Mano, R. 2011. Economic valuation of selected direct and indirect use values of the Makgadikgadi wetland system, Botswana. *Physics and Chemistry of the Earth, Parts A/B/C*, *36*(14-15), pp.1071-1077.

Setlhogile, T., Arntzen, J. and Pule, O.B. 2017. Economic accounting of water: The Botswana experience. *Physics and Chemistry of the Earth, Parts A/B/C*, *100*, pp.287-295.

Sharma, R.C., Tateishi, R., Hara, K. and Nguyen, L.V. 2015. Developing superfine water index (SWI) for global water cover mapping using MODIS data. *Remote Sensing*, *7*(10), pp.13807-13841.

Shaw, P.A. and Bryant, R.G. 2011. Pans, playas and salt lakes. *Arid Zone Geomorphology: Process, Form and Change in Drylands*, pp.373-401.

Sheng, Y., Song, C., Wang, J., Lyons, E.A., Knox, B.R., Cox, J.S. and Gao, F. 2016.

Representative lake water extent mapping at continental scales using multi-temporal Landsat-8 imagery. *Remote Sensing of Environment*, *185*, pp.129-141.

Shih, S.Y., Sun, F.K. and Lee, H.Y. 2019. Temporal pattern attention for multivariate time series forecasting. *Machine Learning*, *108*, pp.1421-1441.

Singh, A. 1989. Review article digital change detection techniques using remotely-sensed data. *International Journal of Remote Sensing*, *10*(6), pp.989-1003.

Sisay, A. 2016. Remote sensing based water surface extraction and change detection in the central rift valley region of ethiopia. *American Journal of Geographic Information System*, *5*(2), pp.33-39.

Slagter, B., Tsendbazar, N.E., Vollrath, A. and Reiche, J. 2020. Mapping wetland characteristics using temporally dense Sentinel-1 and Sentinel-2 data: A case study in the St. Lucia wetlands, South Africa. *International Journal of Applied Earth Observation and Geoinformation*, *86*, p.102009.

Su, Y., Wu, S., Kang, S., Xu, H., Liu, G., Qiao, Z. and Liu, L. 2023. Monitoring Cropland Abandonment in Southern China from 1992 to 2020 Based on the Combination of Phenological and Time-Series Algorithm Using Landsat Imagery and Google Earth Engine. *Remote Sensing*, *15*(3), p.669.

Townshend, J.R. 1994. Global data sets for land applications from the Advanced Very High Resolution Radiometer: an introduction. *International Journal of Remote Sensing*, *15*(17), pp.3319-3332.

Tulbure, M.G. and Broich, M. 2019. Spatiotemporal patterns and effects of climate and land use on surface water extent dynamics in a dryland region with three decades of Landsat satellite data. *Science of the Total Environment*, *658*, pp.1574-1585.

Tulbure, M.G., Broich, M., Stehman, S.V. and Kommareddy, A. 2016. Surface water extent dynamics from three decades of seasonally continuous Landsat time series at subcontinental scale in a semi-arid region. *Remote Sensing of Environment*, *178*, pp.142-157.

Turner, W.C., Périquet, S., Goelst, C.E., Vera, K.B., Cameron, E.Z., Alexander, K.A., Belant, J.L., Cloete, C.C., Du Preez, P., Getz, W.M. and Hetem, R.S. 2022. Africa's drylands in a changing world: Challenges for wildlife conservation under climate and land-use changes in the Greater Etosha Landscape. *Global Ecology and Conservation*, *38*, p.e02221.

Ubilava, D. 2017. The ENSO effect and asymmetries in wheat price dynamics. *World Development*, *96*, pp.490-502.

Vermote, E., Roger, J.C., Franch, B. and Skakun, S. 2018. LaSRC (Land Surface Reflectance Code): Overview, application and validation using MODIS, VIIRS, LANDSAT and Sentinel 2 data's. In *IGARSS 2018-2018 IEEE International Geoscience and Remote Sensing Symposium* (pp. 8173-8176). IEEE.

Wang, G.X. and Cheng, G.D. 2000. The characteristics of water resources and the changes of the hydrological process and environment in the arid zone of northwest China. *Environmental Geology*, *39*(7), pp.783-790.

Wang, R., Xia, H., Qin, Y., Niu, W., Pan, L., Li, R., Zhao, X., Bian, X. and Fu, P. 2020. Dynamic monitoring of surface water area during 1989–2019 in the hetao plain using landsat data in Google Earth Engine. *Water*, *12*(11), p.3010.

Wang, R.Q., Mao, H., Wang, Y., Rae, C. and Shaw, W. 2018. Hyper-resolution monitoring of urban flooding with social media and crowdsourcing data. *Computers & Geosciences*, *111*, pp.139-147.

White, K. and Eckardt, F. 2006. Geochemical mapping of carbonate sediments in the Makgadikgadi basin, Botswana using moderate resolution remote sensing data. *Earth Surface Processes and Landforms*, *31*(6), pp.665-681.

Williams, W.D. 2002. Environmental threats to salt lakes and the likely status of inland saline ecosystems in 2025. *Environmental Conservation*, *29*(2), pp.154-167.

Wulder, M. A., Masek, J. G., Cohen, W. B., Loveland, T. R. and Woodcock, C. E. 2012. Opening the archive: How free data has enabled the science and monitoring promise of Landsat. *Remote Sensing of Environment, 122*, 2-10.

Wulder, M.A., Roy, D.P., Radeloff, V.C., Loveland, T.R., Anderson, M.C., Johnson, D.M., Healey, S., Zhu, Z., Scambos, T.A., Pahlevan, N. and Hansen, M. 2022. Fifty years of Landsat science and impacts. *Remote Sensing of Environment*, *280*, p.113195.

Wurtsbaugh, W.A. 2014. Management of the Great Salt Lake Ecosystem: Water, Economic Values and Competing Interests. *Water Sciences Faculty Publications*, p. 594

Xia, H., Zhao, J., Qin, Y., Yang, J., Cui, Y., Song, H., Ma, L., Jin, N. and Meng, Q. 2019. Changes in water surface area during 1989–2017 in the Huai River Basin using Landsat data and Google earth engine. *Remote Sensing*, *11*(15), p.1824.

Xu, H. 2006. Modification of normalised difference water index (NDWI) to enhance open water features in remotely sensed imagery. *International Journal of Remote Sensing*, *27*(14), pp.3025-3033.

Yates, F. 1934. Contingency Tables Involving Small Numbers and the Chi-Square Test. *Supplement to the Journal of the Royal Statistical Society, 1(2),* 217-235.

Yousefian, F., Sahebi, M., Shokri, M. and Moradi, M. 2019. a Novel Water Index (swi) for Salty Water from Landsat 8 Oli/tirs. *The International Archives of the Photogrammetry, Remote Sensing and Spatial Information Sciences*, *42*, pp.1097-1105.

Yu, D., Bian, X., Yang, L., Zhou, Y., An, D., Zhou, M., Chen, S. and Pan, S. 2023. Monitoring suspended sediment concentration in the Yellow River Estuary from 1984 to 2021 using landsat imagery and Google Earth Engine. *International Journal of Remote Sensing*, *44*(10), pp.3122-3145.

Zhai, K., Wu, X., Qin, Y. and Du, P. 2015. Comparison of surface water extraction performances of different classic water indices using OLI and TM imageries in various situations. *Geo-spatial Information Science*, *18*(1), pp.32-42.

Zhou, Y., Dong, J., Xiao, X., Xiao, T., Yang, Z., Zhao, G., Zou, Z. and Qin, Y. 2017. Open

surface water mapping algorithms: A comparison of water-related spectral indices and sensors. *Water*, *9*(4), p.256.

**Appendix A: Training and Validation points**

| Accuracy assessment: Training and validation points | | | | |
|---|---|---|---|---|
| Year | Water | Bare area | Vegetation | Salt hardpan |
| 1992 | 224/96 | 210/90 | 175/75 | 196/84 |
| 1993 | 280/120 | 140/60 | 189/81 | 196/84 |
| 1994 | 210/90 | 287/123 | 140/60 | 189/81 |
| 1995 | 196/84 | 203/87 | 189/81 | 140/60 |
| 1996 | 294/126 | 140/60 | 161/69 | 105/45 |
| 1997 | 252/108 | 140/60 | 142/68 | 126/54 |
| 1998 | 175/75 | 210/90 | 140/60 | 224/96 |
| 1999 | 196/84 | 126/54 | 84/36 | 98/42 |
| 2000 | 280/120 | 91/39 | 70/30 | 147/63 |
| 2001 | 231/99 | 140/60 | 126/54 | 161/69 |
| 2002 | 175/75 | 142/68 | 140/60 | 63/27 |
| 2003 | 196/84 | 147/63 | 245/105 | 175/75 |
| 2004 | 287/123 | 119/51 | 210/90 | 196/84 |
| 2005 | 210/90 | 105/45 | 161/69 | 315/135 |
| 2006 | 280/120 | 203/87 | 245/105 | 280/120 |
| 2007 | 175/75 | 161/69 | 175/75 | 77/33 |
| 2008 | 224/96 | 175/75 | 280/120 | 231/99 |
| 2009 | 161/69 | 217/93 | 203/87 | 231/117 |
| 2010 | 280/120 | 210/90 | 140/60 | 322/138 |
| 2011 | 210/90 | 140/60 | 119/51 | 140/60 |
| 2012 | 294/126 | 189/81 | 161/69 | 84/36 |
| 2013 | 140/60 | 133/57 | 105/45 | 161/69 |
| 2014 | 266/114 | 256/111 | 315/135 | 105/45 |
| 2015 | 238/102 | 231/99 | 133/57 | 161/69 |
| 2016 | 287/123 | 140/60 | 105/45 | 91/39 |
| 2017 | 322/138 | 203/87 | 70/30 | 224/96 |
| 2018 | 280/120 | 217/93 | 140/60 | 245/105 |
| 2019 | 224/96 | 105/45 | 119/51 | 266/114 |
| 2020 | 196/84 | 287/123 | 147/63 | 175/75 |
| 2021 | 210/90 | 140/60 | 203/87 | 189/81 |
| 2022 | 126/54 | 245/105 | 273/117 | 259/111 |

**Appendix B: LULC Accuracy Assessment**

| Random Forest | | | | | |
|---|---|---|---|---|---|
| | | **Water** | **Bare Area** | **Vegetation** | **Salt hardpan** |
| **TM 1992** | **PA** | 83,33 | 73,33 | 44 | 54,76 |
| | **UA** | 87,91 | 74,16 | 45,83 | 49,46 |
| | **F1 score** | 85,56 | 73,74 | 44,9 | 51,98 |
| **TM 1993** | **PA** | 80 | 56,67 | 64,2 | 75 |
| | **UA** | 91,43 | 80,95 | 59,09 | 57,27 |
| | **F1 score** | 85,33 | 66,67 | 61,54 | 64,95 |
| **TM 1994** | **PA** | 91,11 | 60,83 | 78,33 | 67,9 |
| | **UA** | 89,13 | 81,11 | 66,2 | 56,12 |
| | **F1 score** | 90,11 | 69,52 | 71,76 | 61,45 |
| **TM 1995** | **PA** | 82,14 | 67,82 | 58,02 | 50 |
| | **UA** | 84,15 | 79,73 | 50,54 | 47,62 |
| | **F1 score** | 83,13 | 73,29 | 54,02 | 48,78 |
| **TM 1996** | **PA** | 84,13 | 61,67 | 47,83 | 73,33 |
| | **UA** | 90,6 | 63,79 | 50,77 | 55 |
| | **F1 score** | 87,24 | 62,71 | 49,25 | 62,86 |
| **TM 1997** | **PA** | 93,52 | 53,33 | 52,94 | 64,81 |
| | **UA** | 93,52 | 62,75 | 62,07 | 47,95 |
| | **F1 score** | 93,52 | 57,66 | 57,14 | 55,12 |
| **TM 1998** | **PA** | 78,67 | 77,53 | 68,33 | 71,88 |
| | **UA** | 89,39 | 69,7 | 62,12 | 77,53 |
| | **F1 score** | 83,69 | 73,4 | 65,08 | 74,59 |
| **TM 1999** | **PA** | 89,29 | 77,36 | 41,67 | 66,67 |
| | **UA** | 85,23 | 62,12 | 55,56 | 70 |
| | **F1 score** | 87,21 | 68,91 | 47,62 | 68,29 |
| **TM 2000** | **PA** | 90,76 | 61,54 | 41,67 | 68,42 |
| | **UA** | 87,1 | 70,59 | 46,15 | 62,65 |
| | **F1 score** | 88,89 | 65,75 | 43,8 | 65,41 |
| **TM 2001** | **PA** | 86,87 | 89,29 | 78,05 | 58,02 |
| | **UA** | 97,73 | 75,76 | 66,67 | 69,12 |
| | **F1 score** | 91,98 | 81,97 | 71,91 | 63,09 |
| **ETM+ 2002** | **PA** | 92,96 | 67,12 | 76 | 77,22 |
| | **UA** | 88 | 80,33 | 75,25 | 70,93 |
| | **F1 score** | 90,41 | 73,13 | 75,62 | 73,94 |
| **ETM+ 2003** | **PA** | 94,34 | 81,58 | 61,8 | 68,35 |
| | **UA** | 98,04 | 72,09 | 66,27 | 70,13 |
| | **F1 score** | 96,15 | 76,54 | 63,95 | 69,23 |
| **ETM+ 2004** | **PA** | 97,5 | 46,43 | 65,33 | 80 |
| | **UA** | 88,64 | 72,22 | 74,24 | 64,37 |
| | **F1 score** | 92,86 | 56,52 | 69,5 | 71,34 |
| **ETM+ 2005** | **PA** | 87,91 | 53,19 | 61,54 | 68,63 |
| | **UA** | 86,96 | 61,73 | 74,42 | 48,61 |
| | **F1 score** | 87,43 | 57,14 | 67,37 | 56,91 |
| **ETM+ 2006** | **PA** | 100 | 27,08 | 64,62 | 75 |

| | | | | | |
|---|---|---|---|---|---|
| | **UA** | 94 | 56,52 | 66,67 | 51,72 |
| | **F1 score** | 96,91 | 36,62 | 65,63 | 61,22 |
| **ETM+ 2007** | **PA** | 98,25 | 30 | 82,93 | 86,67 |
| | **UA** | 97,39 | 70,59 | 81,93 | 64,2 |
| | **F1 score** | 97,82 | 42,11 | 82,42 | 73,76 |
| **ETM+ 2008** | **PA** | 97,99 | 12,12 | 73,03 | 65 |
| | **UA** | 95,12 | 26,67 | 80,25 | 48,75 |
| | **F1 score** | 96,53 | 16,67 | 76,47 | 55,71 |
| **ETM+ 2009** | **PA** | 92,27 | 31,71 | 81,91 | 64 |
| | **UA** | 97,81 | 34,21 | 82,8 | 49,23 |
| | **F1 score** | 94,96 | 32,91 | 82,35 | 55,65 |
| **ETM+ 2010** | **PA** | 95,12 | 54,55 | 83,47 | 50 |
| | **UA** | 95,12 | 52,17 | 82,11 | 56,41 |
| | **F1 score** | 95,12 | 53,33 | 82,79 | 53,01 |
| **ETM+ 2011** | **PA** | 90,63 | 68,67 | 85,71 | 27,78 |
| | **UA** | 94,42 | 49,14 | 84,44 | 53,57 |
| | **F1 score** | 92,48 | 57,29 | 85,07 | 36,59 |
| **ETM+ 2012** | **PA** | 95,19 | 71,2 | 80,99 | 31,82 |
| | **UA** | 93,68 | 53,94 | 81,56 | 60,87 |
| | **F1 score** | 94,43 | 61,38 | 81,27 | 41,79 |
| **OLI 2013** | **PA** | 96,91 | 79,87 | 92,86 | 45,12 |
| | **UA** | 97,52 | 71,93 | 83,49 | 67,27 |
| | **F1 score** | 97,21 | 75,69 | 87,92 | 54,01 |
| **OLI 2014** | **PA** | 96,25 | 93,33 | 62,9 | 51,76 |
| | **UA** | 95,06 | 62,69 | 88,64 | 77,19 |
| | **F1 score** | 95,65 | 75 | 73,58 | 61,97 |
| **OLI 2015** | **PA** | 96,69 | 64,63 | 84,38 | 86,46 |
| | **UA** | 95,12 | 82,81 | 81,82 | 75,45 |
| | **F1 score** | 95,9 | 72,6 | 83,08 | 80,58 |
| **OLI 2016** | **PA** | 99,16 | 75,32 | 59,15 | 83,33 |
| | **UA** | 99,16 | 64,44 | 67,74 | 86,73 |
| | **F1 score** | 99,16 | 69,46 | 63,16 | 85 |
| **OLI 2017** | **PA** | 98,48 | 66,04 | 66,67 | 58,75 |
| | **UA** | 98,48 | 70 | 50,67 | 72,31 |
| | **F1 score** | 98,48 | 67,96 | 57,57 | 64,83 |
| **OLI 2018** | **PA** | 98,31 | 77,36 | 66,07 | 69,23 |
| | **UA** | 99,43 | 82 | 57,81 | 72 |
| | **F1 score** | 98,86 | 79,61 | 61,67 | 70,59 |
| **OLI 2019** | **PA** | 92,59 | 78,33 | 64,91 | 76,92 |
| | **UA** | 98,04 | 73,44 | 59,68 | 80 |
| | **F1 score** | 95,24 | 75,81 | 62,18 | 78,43 |
| **OLI 2020** | **PA** | 98,31 | 90 | 66,67 | 62,82 |
| | **UA** | 100 | 79,12 | 61,29 | 77,78 |
| | **F1 score** | 99,15 | 84,21 | 63,87 | 69,5 |
| **OLI 2021** | **PA** | 86,67 | 91,57 | 83,33 | 78,65 |
| | **UA** | 97,5 | 82,61 | 71,43 | 87,5 |
| | **F1 score** | 91,76 | 86,86 | 76,92 | 82,84 |
| **OLI 2022** | **PA** | 97,87 | 71,79 | 52,56 | 61,46 |

| | | | | | |
|---|---|---|---|---|---|
| | **UA** | 93,24 | 86,6 | 41,41 | 67,05 |
| | **F1 score** | 95,5 | 78,5 | 46,3 | 64,13 |

**Rating criteria of Kappa statistics according to Cohen (1960).**

| **Kappa** | **Strength of agreement** |
|---|---|
| <0.00 | Poor |
| 0.00–0.20 | Slight |
| 0.21–0.40 | Fair |
| 0.41–0.60 | Moderate |
| 0.61–0.80 | Substantial |
| 0.81–1.00 | Almost perfect |

## Appendix C: R-Studio Codes

### McNemar Test

MNDWI

```
Performance <-
  matrix(c(94, 6, 66, 34),
         nrow = 2,
         dimnames = list("Non water" = c("Approve", "Disapprove"),
                         "water" = c("Approve", "Disapprove")))
Performance
mcnemar.test(Performance)
```

NDSI

```
Performance <-
  matrix(c(97, 3, 79, 21),
         nrow = 2,
         dimnames = list("Non water" = c("Approve", "Disapprove"),
                         "water" = c("Approve", "Disapprove")))
Performance
mcnemar.test(Performance)
```

SWI

```
Performance <-
  matrix(c(91, 9, 4, 96),
         nrow = 2,
         dimnames = list("Non water" = c("Approve", "Disapprove"),
                         "water" = c("Approve", "Disapprove")))
Performance
mcnemar.test(Performance)
```

### Pearsons Correlation

```
library(readxl)
> Book3 <- read_excel("Book3.xlsx")
> View(Book3)
> correlation <- cor(Book3$rainfall, Book3$enso, method = 'pearson')
> cor.test(Book3$rainfall, Book3$enso)

        Pearson's product-moment correlation

data:  Book3$rainfall and Book3$enso
t = -2.2878, df = 29, p-value = 0.02963
alternative hypothesis: true correlation is not equal to 0
95 percent confidence interval:
 -0.65465305 -0.04257603
sample estimates:
       cor
-0.3910171


> correlation <- cor(Book3$rainfall, Book3$LST, method = 'pearson')
> cor.test(Book3$rainfall, Book3$LST)

        Pearson's product-moment correlation

data:  Book3$rainfall and Book3$LST
t = -7.9594, df = 21, p-value = 8.934e-08
alternative hypothesis: true correlation is not equal to 0
```

```
95 percent confidence interval:
 -0.9422384 -0.7069767
sample estimates:
       cor
-0.8666283
> correlation <- cor(Book3$rainfall, Book3$evapo, method = 'pearson')
> cor.test(Book3$rainfall, Book3$evapo)

        Pearson's product-moment correlation

data:  Book3$rainfall and Book3$evapo
t = 7.4083, df = 20, p-value = 3.741e-07
alternative hypothesis: true correlation is not equal to 0
95 percent confidence interval:
 0.6799019 0.9388458
sample estimates:
      cor
0.8561056
> correlation <- cor(Book3$rainfall, Book3$wet, method = 'pearson')
> cor.test(Book3$rainfall, Book3$wet)

        Pearson's product-moment correlation

data:  Book3$rainfall and Book3$wet
t = 3.9645, df = 29, p-value = 0.0004406
alternative hypothesis: true correlation is not equal to 0
95 percent confidence interval:
 0.3019430 0.7827582
sample estimates:
      cor
0.5928535
```

## ANOVA

```
# NAME VARIABLES
data <- ENSORSWA
ENSO <- data$ENSO
Rainfall <- data$Rainfall
# SHOW LEVELS OF CATEGORICAL VARIABLE
levels(ENSO)
library(dplyr)
group_by(data, ENSO) %>% summarise(count = n(), mean = mean(Rainfall, na.rm
= TRUE), sd = sd(SWA, na.rm = TRUE))
res.aov <- aov(Rainfall ~ ENSO, data = data)
summary(res.aov)
TukeyHSD(res.aov)
```

```
# NAME VARIABLES
data <- ENSORSWA
ENSO <- data$ENSO
SWA <- data$SWA
# SHOW LEVELS OF CATEGORICAL VARIABLE
levels(ENSO)
library(dplyr)
group_by(data, ENSO) %>% summarise(count = n(), mean = mean(Rainfall, na.rm
= TRUE), sd = sd(SWA, na.rm = TRUE))
```

```
res.aov <- aov(SWA ~ ENSO, data = data)
summary(res.aov)
TukeyHSD(res.aov)
```

## Appendix D: Google Earth Engine Codes

**SWI surface water extraction code**

```
function maskL8(col) {
   var cloudshadowbitmask = (1 << 3);
   var cloudsbitmask = (1 << 5);
   var qa = col.select('QA_PIXEL');
   var mask = qa.bitwiseAnd(cloudshadowbitmask).eq(0)
                 .and(qa.bitwiseAnd(cloudsbitmask).eq(0));
  return col.updateMask(mask);
}
//Landsat 8 SR
var l8 = ee.ImageCollection('LANDSAT/LC08/C02/T1_L2')
var l8Filt = l8.filterBounds(aoi)
               .map(maskL8)
                 //.filterDate('2020-01-01', '2020-03-31')// wet season
                 //.filterDate('2014-08-01', '2014-10-31')// dry season
            ;
// Applies scaling factors.
function applyScaleFactors(image) {
  var opticalBands = image.select('SR_B.').multiply(0.0000275).add(-0.2);
  var thermalBand =
image.select('ST_B.*').multiply(0.00341802).add(149.0);
  return image.addBands(opticalBands, null, true)
              .addBands(thermalBand, null, true);
}

var dataset8 = l8Filt.map(applyScaleFactors);
var visualization = {
  bands: ['SR_B5', 'SR_B6', 'SR_B4'],
  min: 0.0,
  max: 0.3,
};

//Map.addLayer(dataset, visualization, 'True Color (321)');

var l8compositeMasked = dataset8.median().clip(aoi);

print('L8 composite masked', l8compositeMasked);

Map.addLayer(l8compositeMasked,
             {bands:['SR_B5','SR_B6','SR_B4']},
             'L8 composite masked');

//>> Salinity Water Index
var SWI = l8compositeMasked.expression(
    "(2 * NIR - 5 * (GREEN - SWIR1) * sqrt (GREEN * RED))",
    {
      NIR: l8compositeMasked.select("SR_B5"),    // NIR
      SWIR1 : l8compositeMasked.select("SR_B6"),   // SWIR1
      GREEN: l8compositeMasked.select("SR_B3"),   // GREEN
     RED: l8compositeMasked.select("SR_B4"),    //  RED
    }).rename('SWI');

Map.addLayer(SWI, {min: 0, max: 1, palette: ['blue', 'pink','white']},
"SWI");

var SWIThreshold = SWI.lte(0.4);
var SWIMask = SWIThreshold.updateMask(SWIThreshold);
//Map.addLayer(SWIThreshold, {palette:['black','white']}, 'SWI Binary
Mask');
Map.addLayer(SWIMask, {palette:['blue']}, 'SWI Mask');
```

```
Export.image.toDrive({
  image: SWIMask,
  description: 'SWA',
  folder:'last',
  fileFormat: 'GeoTIFF',
  maxPixels:1e13,
  region:aoi,
});

//Spectral Charts
//Choose bands to include and define feature collection to use
var subset = l89composite.select('SR_B[2-7]')
var samples = ee.FeatureCollection([water, nonwater]);
// Define customization options.
var plotOptions = {
  title: 'MNDWI  Surface reflectance spectra',
  hAxis: {title: 'Wavelength (nanometers)'},
  vAxis: {title: 'Reflectance'},
  lineWidth: 1,
  pointSize: 4,
  series: {
    0: {color: 'blue'}, // water
    1: {color: 'red'}, // bareAreas
}};

// Define a list of Landsat-8 wavelengths for X-axis labels.
var wavelengths = [452, 533, 636, 851, 1566, 2107];

// Create the chart and set options.
var Chart2 = ui.Chart.image.regions(

    subset, samples, ee.Reducer.mean(), 10, 'label', wavelengths)
        .setChartType('LineChart')
        .setOptions(plotOptions);
// Display the chart.
print(Chart2);
// We can now calculate the masked areas pixel area
var SWIPixelArea =
ee.Image.pixelArea().addBands(SWIMask.select('SWI')).divide(1e6).reduceReg
ion({
    reducer: ee.Reducer.sum().group(1),
    geometry: aoi,
    scale: 10,
    bestEffort: true
});

var list = ee.List(ee.Dictionary(SWIPixelArea).get('groups'));
var group0 = ee.Dictionary(list.get(0));
var SWIWaterArea = ee.Number(group0.get('sum')).float();
print("Water area (km2):", SWIWaterArea);
```